



MAX PLANCK INSTITUTE
FOR POLYMER RESEARCH

The Current-Driven Organic Electrochemical Transistor for Sensing Barrier Tissue Modulation

Zur Erlangung des Grades
„Doktor der Naturwissenschaften“

im Fachbereich Chemie, Pharmazie, Geographie und
Geowissenschaften

Der Johannes Gutenberg-Universität Mainz und in Kooperation
mit dem Max-Planck-Institut für Polymerforschung Mainz

Vorgelegt von
Katharina Lieberth
Geboren in Bamberg, Deutschland
Mainz, 15.03.2022

The thesis was carried out from October 2018 until March 2022 in the group of Prof. Dr. Paul W. M. Blom at the Max Planck Institute for Polymer Research in Mainz.

Die vorliegende Arbeit wurde in der Zeit von Oktober 2018 bis März 2022 im Max-Planck-Institut für Polymerforschung in Mainz unter der Betreuung von Prof. Dr. Paul W. M. Blom durchgeführt.

Dekan Univ. – Prof. Dr. Tanja Schirmeister

Prodekan: Univ.-Prof. Dr. Tobias Reich & Univ.-Prof. Dr. Till Opatz

1. Berichterstatter: Prof. Dr. Paul W. M. Blom
2. Berichterstatter: Prof. Dr. Pol Besenius

Tag der mündlichen Prüfung: 5.05.2022

Was man zu verstehen gelernt hat, fürchtet man nicht mehr!

(Marie Curie)

*Out beyond ideas of wrongdoing and rightdoing,
there is a field. I'll meet you there.*

*When the soul lies down in that grass,
the world is too full to talk about.*

*Ideas, language, even the phrase "each other"
doesn't make any sense.*

The breeze at dawn has secrets to tell you.

Don't go back to sleep.

You must ask for what you really want.

Don't go back to sleep.

*People are going back and forth across the doorsill
where the two worlds touch.*

The door is round and open.

Don't go back to sleep.

(Jelaluddin Rumi)

Abstract

The scientific progress of biosensors exponentially raised over the past 30 years. The organic electrochemical transistor (OECT) as one of the major new developments gives hope for a huge step forward when introducing new form factors for medical technologies. Bioelectronic applications aim to replace, reduce and refine the animal model and specialize the research on drug delivery. However, the translation of OECTs as an impedance sensor, for sensing *in vitro* cultured barrier tissue into commercial applications is still facing challenges. One main challenge is to avoid the electrical stress and degradation of biological systems by electronic sensors. Biological tissue could be stressed or even disrupted, when electrical potential is applied too high or over long timescales. Another challenge is to improve the sensitivity of the sensor in order to study the events of interest with high precision.

As a first topic the thesis addresses the ability to monitor with OECTs small changes in the barrier functionality of biological tissue *in-situ* over a long-time scale. Changes in barrier tissue are indicated by small changes of ion flow across the barrier under the presence of a variation of ions. The opening of tight junction (TJ) protein complexes, built between the cells, is a rather fast process in the range of minutes, whereas the recovery of TJs is rather slow lasting several hours. Therefore, a new measurement method has been developed, the so-called current-driven configuration, where only a very small current bias is applied to the OECT. In the first part of this work, we demonstrate that the OECT in current-driven configuration can sense the effect of TJ modulators on barrier tissue, while measuring over 24 hours *in-situ*. As a result, not only reversible TJ modulation could be monitored, but also the effects of various TJ modulator concentrations on barrier tissue. These results show that the OECT with integrated barrier tissue can be used as a detector to evaluate the effectiveness of TJ modulators in a concentration range well below the toxicity level.

As next step we put the focus on another main issue in OECTs as impedance sensors, which is to realize a measurement method with high sensitivity that enables to transfer measured voltage outputs into the resistance of barrier tissue equivalently. For that we have developed the measurement technique of the dynamic current-driven configuration, where the transfer characteristics are measured forward and backward. The observed hysteretic window can be used as a sensitive detector for changes in the permeability of the barrier tissue. The transfer characteristics of the current-driven OECT with integrated barrier tissue have been simulated with an equivalent circuit model, in order to obtain the resistance of barrier tissue as a result.

1-II Abstract

Our results open promising perspectives towards bioelectronic devices with high sensitivity, where due to the low applied voltage and current as well as the reduced measurement time the measured barrier tissue can be monitored in-situ over time.

Abstrakt

Der wissenschaftliche Fortschritt von Biosensoren hat sich in den letzten 30 Jahren exponentiell erhöht. Der organische elektrochemische Transistor (OECT) als eine der wichtigsten Neuentwicklungen gibt Hoffnung auf einen großen Schritt nach vorn bei der Einführung neuer Formfaktoren für medizinische Technologien. Bioelektronische Anwendungen zielen darauf ab, das Tiermodell zu ersetzen, zu reduzieren und zu verfeinern und die Forschung zur Medikamentenverabreichung zu spezialisieren. Die Umsetzung von OECTs als Impedanzsensor zur Messung von *in vitro* gezüchtetem Barrieregewebe in kommerzielle Anwendungen steht jedoch noch vor Herausforderungen. Eine der größten Herausforderungen ist die Vermeidung von elektrischem Stress und Degradation biologischer Systeme durch elektronische Sensoren. Biologisches Gewebe könnte gestresst oder sogar gestört werden, wenn ein zu hohes elektrisches Potenzial oder über zu lange Zeiträume angelegt wird. Eine weitere Herausforderung besteht darin, die Empfindlichkeit des Sensors zu verbessern, um die relevanten Ereignisse mit hoher Präzision untersuchen zu können.

Als erstes Thema befasst sich die Arbeit mit der Fähigkeit, mit OECTs kleine Veränderungen in der Barrierefunktionalität von biologischem Gewebe *in-situ* über eine lange Zeitskala zu überwachen. Veränderungen im Barrieregewebe werden durch kleine Veränderungen des Ionenflusses durch die Barriere in Gegenwart verschiedener Ionen angezeigt. Die Öffnung der Proteinkomplexe der Tight Junctions (TJ), die zwischen den Zellen gebildet werden, ist ein relativ schneller Prozess im Minutenbereich, während die Wiederherstellung der TJs eher langsam erfolgt und mehrere Stunden dauert. Daher wurde eine neue Messmethode entwickelt, die so genannte stromgesteuerte Konfiguration, bei der nur eine sehr geringe Stromvorspannung an den OECT angelegt wird. Im ersten Teil dieser Arbeit zeigen wir, dass der OECT in der stromgesteuerten Konfiguration die Wirkung von TJ-Modulatoren auf Barrieregewebe erfassen kann, während wir über 24 Stunden *in-situ* messen. So konnte nicht nur die reversible TJ-Modulation überwacht werden, sondern auch die Auswirkungen verschiedener TJ-Modulator-Konzentrationen auf das Barrieregewebe. Diese Ergebnisse zeigen, dass die OECT mit integriertem Barrieregewebe als Detektor verwendet werden kann, um die Wirksamkeit von TJ-Modulatoren in einem Konzentrationsbereich weit unterhalb des Toxizitätsniveaus zu bewerten.

In einem nächsten Schritt haben wir den Fokus auf ein weiteres Hauptproblem bei OECTs als Impedanzsensoren gelegt, nämlich eine Messmethode mit hoher Empfindlichkeit zu realisieren, die es ermöglicht, gemessene Spannungsausgänge äquivalent in den Widerstand

1-IV Abstrakt

des Barrieregewebes zu übertragen. Zu diesem Zweck haben wir die Messtechnik der dynamischen stromgesteuerten Konfiguration entwickelt, bei der die Übertragungseigenschaften vorwärts und rückwärts gemessen werden. Das beobachtete hysteretische Fenster kann als empfindlicher Detektor für Änderungen in der Permeabilität des Barrieregewebes verwendet werden. Die Übertragungseigenschaften der stromgesteuerten OECT mit integriertem Barrieregewebe wurden mit einem Ersatzschaltbildmodell simuliert, um den Widerstand des Barrieregewebes als Ergebnis zu erhalten.

Unsere Ergebnisse eröffnen vielversprechende Perspektiven für bioelektronische Geräte mit hoher Empfindlichkeit, bei denen aufgrund der geringen angelegten Spannung und Stromstärke sowie der reduzierten Messzeit das gemessene Barrieregewebe in-situ über die Zeit überwacht werden kann.

Table of Contents

Abstract	1-I
Abstrakt	1-III
List of Figures	1-VIII
Glossary	1-X
Abbreviations	1-XII
1 Organic Bioelectronics	1-1
1.1 Organic Bioelectronics: A Field with an Impressive Perspective	1-2
1.1.1 Mixed Ion-Electron Conductors: The Workhorse in Organic Bioelectronics	1-3
1.1.2 The Base of Bioelectronics: PEDOT:PSS Coated Electrodes	1-5
1.1.3 Ion-Gated Organic Transistors.....	1-6
1.2 The Raising Potential of the Organic Electrochemical Transistor	1-7
1.2.1 Device Structure: Materials and Fabrication Process	1-7
1.2.2 Application of the OECT in Biology	1-9
1.3 The OECT as an Impedance Sensor	1-10
1.3.1 The role of Tight Junctions in Barrier Tissues	1-10
1.3.2 Benefits of OECTs.....	1-12
1.3.3 Monitoring Barrier Tissue Integrity with the OECT in Standard Configuration	1-13
1.4 References	1-16
2 Enhanced Ion Sensitive Current-Driven OECT Configuration	2-21
2.1 Highly-Sensitive ion Detection at low Voltages with Current-Driven OECTs.....	2-22
2.2 Complementary OECT Amplifier Based on the Current-Driven OECT Architecture	2-24
2.3 Sensing Barrier Tissue Integrity and Irreversible Barrier Tissue Disruption with the Current- Driven OECT	2-26
2.4 Motivation and Outline.....	2-28
2.5 References	2-30
3 Experiment and Methods	3-31

3.1	PEDOT:PSS Formulations	3-32
3.2	Fabrication of OECTs.....	3-32
3.3	Cell Preparation	3-33
3.3.1.	Culturing of Caco-2 Cells	3-33
3.3.2.	Transwell-filter Preparation	3-34
3.4	Characterization Methods.....	3-34
3.4.1	Electrical characterisation using the OECT	3-35
	Standard Transient Response Measurements	3-36
	Standard Current-Driven Configuration.....	3-36
	Dynamic Current-Driven Configuration	3-36
	Electrochemical impedance spectroscopy	3-36
3.4.2	Transepithelial electrical resistance measurement as an alternative electrical characterisation method	3-37
3.4.3	Optical Characterisation	3-38
	Cell Viability Assay	3-38
	Immunofluorescence Staining	3-38
3.5	References	3-40
4	Monitoring reversible Tight Junction Modulation with the OECT.....	4-41
4.1	Summary.....	4-41
4.2	Introduction	4-42
4.3	Results and discussion	4-44
4.3.1	Current-driven OECT with cell barrier integrity.	4-44
4.3.2	Sensing reversible tight junction modulation over time with a current- driven OECT	4-45
4.3.3	The concentration effect of TJ modulator PLL measured by current-driven OECT as a dynamic sensor for reversible tight junction modulation	4-47
4.4	Conclusion	4-53
4.5	References	4-54
5	High-sensitivity real-time monitoring of cellular barrier functionality with dynamic-mode current-driven organic electrochemical transistor	5-56
5.1	Summary.....	5-56

5.2	Introduction	5-57
5.3	Results	5-60
5.3.1	Dynamic mode current-driven OECT.....	5-60
5.3.2	Operation Mechanism.....	5-65
5.3.3	High-sensitivity real-time monitoring of cellular barrier functionality .	5-70
5.4	Conclusion	5-72
5.5	References	5-74
6	Conclusion.....	6-76
	Appendix	6-79
	Declaration	6-79
	List of Publications.....	6-80
	List of Conferences	6-82
	Curriculum Vitae.....	6-83
	Acknowledgements	6-84

List of Figures

Figure 1.1: The Raise of Bioelectronics. Amount of Publications per year on “bioelectronics”, “OECT“, and “OECT + Sensor“ over the last thirty years.	1-2
Figure 1.2: Bioelectronics as an <i>in vitro</i> platform for drug delivery development in order to replace, reduce, and refine <i>in vivo</i> studies on the animal model and in human.	1-3
Figure 1.3: The OECT with PEDOT:PSS as OMIEC.....	1-4
Figure 1.4: Comparison in the device structure of a) organic field-effect transistor (OFET), b) the electrolyte gated organic field effect transistor (EGOFET), and c) the organic electrochemical transistor (OECT).....	1-7
Figure 1.5: Comparison of the OECT and the OFET regarding the transconductance g_m over frequency.....	1-7
Figure 1.6: Conceptional representation of the OECT as an impedance biosensor.....	1-9
Figure 1.7: The OECT and its application as an impedance sensor.	1-11
Figure 1.8: Barrier modulation of biological tissue..	1-12
Figure 1.9: Sensing barrier integrity and barrier disruption with the standard OECT configuration.	1-14
Figure 1.10: Monitoring barrier tissue disruption with the OECT <i>in-situ</i> due to the addition of toxins.	1-15
Figure 2.1: Current-driven OECT used as ion sensor.	2-24
Figure 2.2: The OECT complementary amplifier.	2-26
Figure 2.3: Sensing cell barrier integrity for H ₂ O ₂ with an OECT in current-driven configuration.	2-27
Figure 3.1: Device with and without PMMA-well.	3-33
Figure 3.2: Filter Preparation.	3-34
Figure 3.3: Device operation of an OECT with an integrated barrier tissue.....	3-35
Figure 3.4: Device setup of a TER Volt-Ohm-Meter	3-37
Figure 4.1: Current-driven OECT with cell barrier integrity.....	4-45
Figure 4.2: Sensing reversible tight junction modulation over time with a current-driven OECT.	4-46
Figure 4.3 The concentration effect of TJ modulator PLL measured by current-driven OECT as an <i>in-situ</i> sensor for reversible tight junction modulation.	4-48
Figure 4.4: Stability measurement of a current-driven OECT with an integrated barrier tissue.	4-49

Figure 4.5: Sensing the effect of deionized water on Caco-2 barrier tissue over time with a current-driven OECT.....	4-50
Figure 4.6: PLL toxicity on Caco2 cells is time and concentration dependent.....	4-51
Figure 4.7: The concentration effect of TJ modulator PLL measured by immunofluorescence staining of occludin (green) in human CaCo-2 cells cultivated on day 14 on coverslips (1.12 cm ²) and treated with different concentration of PLL.	4-52
Figure 4.8: Redistribution of occludin staining after high PLL treatment and 20 h recovery under Transwell culture conditions.	4-52
Figure 4.9: Caco2 cells show a cell recovery only after low PLL exposure.	4-53
Figure 5.1: Dynamic-mode current-driven organic electrochemical transistor (OECT).	5-61
Figure 5.2: Electrochemical impedance spectroscopies.....	5-62
Figure 5.3: Electrical characteristics of OECTs without and with cellular barrier tissue.	5-63
Figure 5.4: Operation mechanism.	5-65
Figure 5.5: Impact of the scan rate on the OECT characteristics.....	5-66
Figure 5.6: Impact of the scan rate on the V_O - V_I characteristics.	5-67
Figure 5.7: Wide range high sensitivity operation.	5-69
Figure 5.8: Impact of the scan rate and ionic resistance.	5-70

Glossary

AR	Average sensitivity
BBL	Poly-benzimidazobenzophenanthrolin
cLSM	Confocal laser scanning microscopy
CD	Current-driven configuration
CP	Conducting polymer
DBSA	4-dodecylbenzenesulfonic acid
DCD	Dynamic-mode current-driven configuration
DMSO	Dimethyl sulfoxide
EDL	Electronic double layer
EDTA	Ethylenediamine-N,N,N',N'-tetraacetic acid
EG	Ethylene glycol
EIS	Electrochemical impedance spectroscopy
EGOFET	Electrolyte-gated field-effect transistor
EGTA	Ethylene glycol-bis(beta-aminoethyl ether) -N,N,N',N'-tetraacetic acid
EMEM	Eagle's Minimum Essential Medium
EtOH	Ethanol
FBS	Fetal bovine serum
GOPS	3-glycidoxypropyltrimethoxysilane
HS	High sensitivity
ISM	Ion-selective membrane
OC	Output characteristics
OEET	Organic electrochemical transistor
OEM	Organic electronic material
OFET	Organic field-effect transistor
OMIEC	Organic mixed ionic-electronic conductor
PBS	Dulbecco's Phosphate Buffered Saline
PDMS	Polydimethylsiloxane
PEDOT	Poly(3,4-ethylenedioxythiophene)
Pen/Strep	Penicilin/ Streptomycin
PMMA	Poly(methyl methacrylate)
PSS	Poly(styrene sulfonic acid)

PLL	Poly-L-lysine
RIE	Reactive ion etching
SR	Scan rate
TC	Transfer characteristics
TER	Transepithelial electrical resistance
TR	Transient Response
TJ	Tight junctions
WR	Wide range

Abbreviations

C	Concentration
C_M	Capacitance of the barrier tissue membrane
C_{OECT}	Capacitance of the OECT
C_V	Volumetric capacitance
d	Thickness
f	Frequency
G	Conductance
g_m	Transconductance
I_B	Current bias
I_D	Drain current
λ	Channel length modulation
L	Length
μ	Charge carrier mobility
N_{fix}	Amount of fixed charges
N_P	Number of periods
Q	Elementary charge
R_A	Resistance of apical electrolyte
R_B	Resistance of basal electrolyte
R_F	Resistance of Transwell filter
R_G	Resistance of the gate electrode
R_M	Resistance of the barrier tissue membrane
R_{OECT}	Resistance of the OECT
t	Time
t_P	Thickness of the channel
T	Temperature
V_{CH}	Actual potential gating of the OECT
V_D	Drain voltage
V_{DD}	Supply voltage (current-driven OECT)
V_G	Gate voltage
V_{IN}/V_I	Input voltage (current-driven OECT)
V_M	Potential drop across the barrier tissue

V_{OUT}/ V_O	Output voltage (current-driven OECT)
V_{PS}	Voltage phase shift (dynamic-mode current-driven OECT)
V_T	Threshold voltage
V_S	Source voltage
V_{SW}	Switching voltage
ΔV_{SW}	Hysteresis of the switching voltage
W	Width
Z_{MEM}	Impedance of cell layer

1 Organic Bioelectronics

In this chapter the scientific path of organic bioelectronics is drawn, starting from the history and concept till recent achievements using the Organic Electrochemical Transistor (OECT) as a biosensor for impedance sensing of cell layers.

1.1 Organic Bioelectronics: A Field with an Impressive Perspective

Utilizing electronic circuits to detect or stimulate biological systems is understood as the field of bioelectronics. The famous experiment of Luigi Galvani in the 1780s was the first step into bioelectronic research, investigating the movement of a sciatic nerve of detached frogs' legs upon applied potential of an inorganic electrode. As the field of organic bioelectronics grew exponentially over the last 30 years (**Fig. 1.1**), more and more applications for biology were developed and complement the inorganic counterpart.

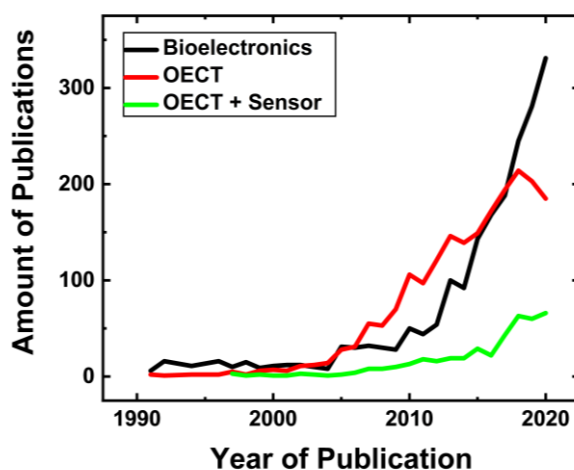


Figure 1.1: The Raise of Bioelectronics. Amount of Publications per year on “bioelectronics”, “OECT“, and “OECT + Sensor“ over the last thirty years, using data from the online database Scopus of Elsevier.

The translation of biochemical signals is crucial, as it portrays numerous regulating and defence mechanisms in humans and animals represented by small cations^[1] (nutrients) and neurotransmitters (hormones)^[2], but also macromolecules (DNA^[3] and proteins^[4]). State-of-the-art optical techniques, like immunofluorescence staining and permeability assays, have drawbacks, like the spatio-temporal resolution together with biocompatibility, invasiveness and time-consuming processability.^[5,6] To answer today's questions non-invasive devices are of great need, allowing *in vitro* and *in vivo studies* in the medical domains of therapy, diagnostics, cell biology and health care monitoring, e.g., pacemaker, deep brain stimulator or cochlear implants. As schematically portrait in **Fig. 1.2**, bioelectronics are used as an *in vitro* platform for drug delivery development in order to replace, reduce, and refine *in vivo* studies on the animal model and in human. Organic bioelectronic devices are promising candidates to overcome these challenges, as they have the ability to bridge the signalling gap between biology and technology due to their high biocompatibility and the possibility to tailor physical properties of the organic electronic conducting material (OEM) due to organic synthesis. Besides humans, organic bioelectronics also found relevant applications considering fungi,

plants,^[7] bacteria,^[8] protista and archaea systems.^[9] Organic bioelectronic devices contain an organic electronic conducting material in various device architectures, such as permeable/semipermeable membranes on electrodes, semiconductors and conductors in transistors and as insulators.^[9] Being biocompatible and having the ability to tailor physical properties like ion-sensitivity, stretchability, or stability in aqueous electrolyte according to the sensing application by organic synthesis, makes them the workhorse of organic bioelectronics.

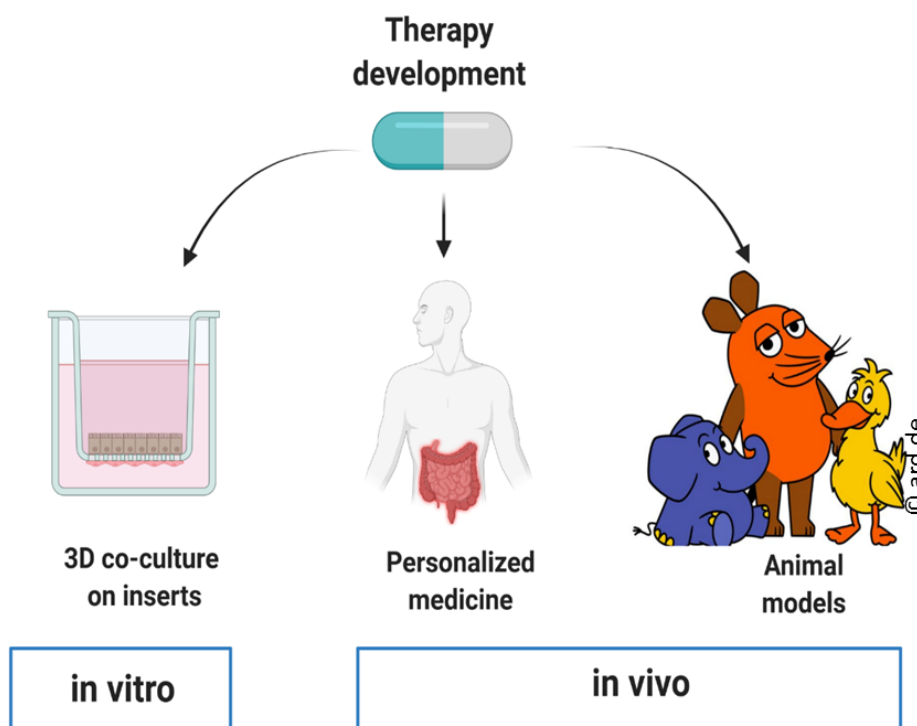


Figure 1.2: Bioelectronics as an *in vitro* platform for drug delivery development in order to replace, reduce, and refine *in vivo* studies on the animal model and in human. Created with biorender.com.

1.1.1 Mixed Ion-Electron Conductors: The Workhorse in Organic Bioelectronics

Small molecules and more important conducting polymers (CPs) are utilized in organic bioelectronics, transporting either electrons (n-type) or holes (p-type). The first explored biocompatible CPs were the hole conducting polymers polypyrrole (PPy)^[10] and poly(3,4-ethylenedioxythiophene) (PEDOT)^[11,12]. Both CPs can be obtained from monomer solutions together with their counterions by electropolymerisation or by polymeric chain reaction.^[11,12,13,14] Positively doped CPs, by removing one electron, have a high electric conductivity across the volume, due to large charge delocalisation over the CP's π -orbitals. The semiconducting polymer PEDOT gained increasing attention over PPy due to its enhanced water stability, although it is only water soluble together with its counterion.^[15] The dopant counterion stabilizes the doping state of PEDOT in aqueous electrolyte, being hydrophilic, but also promotes ion permeability throughout the whole volume of PEDOT:PSS films due to the

1-4 Organic Bioelectronics: A Field with an Impressive Perspective

porous morphology.^[15–17] As counterion for PEDOT the anionic polyelectrolyte poly(styrene sulfoxide) (PSS) (Fig. 1.3 a) was established, providing high stability and ion permittivity.^[18] PSS forms an amorphous backbone, in which PEDOT-rich domains are embedded. By applying positive gate bias, cations from the electrolyte are driven into the whole volume of the CP and thus dedope PEDOT. PEDOT:PSS therefore transduces ion flux into electronic current, as PEDOT is electrochemically reduced by the penetration of cations into the PEDOT:PSS film, and oxidized again when cations are removed from the film. Since PEDOT:PSS can transport both ionic and electronic charges, it is called an organic mixed ion-electron conductor (OMIEC).^[19,20] The ionic conductance of the polymer is determined by the density and morphology of the PSS phase while the electronic conductance is determined by the structural and physical properties of the PEDOT phase.^[15,16,21] As ions penetrate the whole volume of the CP film, the electronic conductivity is a volumetric property. P-type doped CP-films operate in depletion mode (Fig. 1.3 b). Vice versa n-type CPs, such as pristine poly-benzimidazobenzophenanthrolin (BBL), operate in accumulation mode.

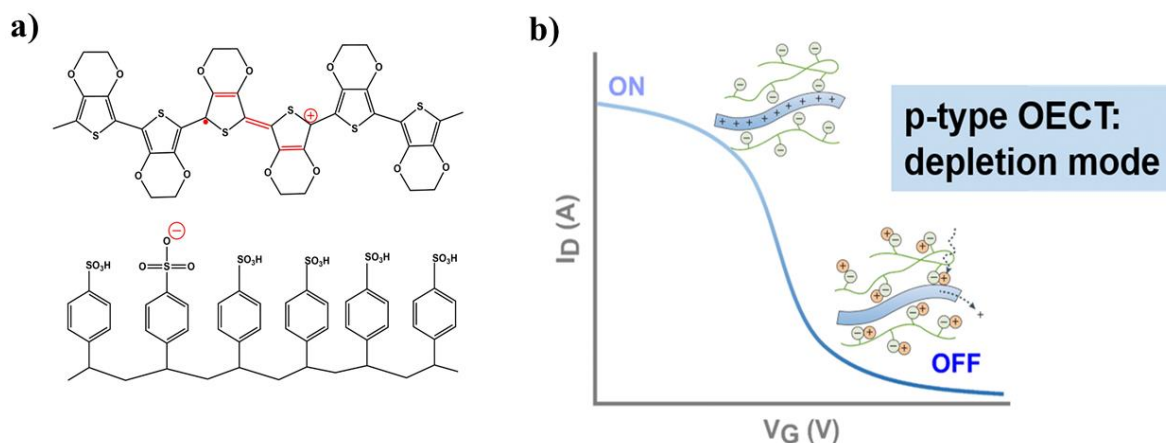


Figure 1.3: The OEECT with PEDOT:PSS as OMIEC. **a)** Molecular structure of positively doped conducting polymer PEDOT (up) and the negatively charged polyelectrolyte PSS (down). **b)** Working principle of a p-type OEECT with PEDOT: PSS as CP, operating in depletion mode. Reproduced with permission.^[31] Copyright 2018, Springer Nature.

Relevant features for bioelectronic operation are the operation at voltages well-below 1 V and stability in liquid environment. PEDOT:PSS provides these properties, accompanied by a flexible morphology, optical transparency, processability and scalable green synthesis. In direct interface to tissues or cell layers, the soft and stretchable morphology of CPs enables achieving the ideal interface conditions, as it is the case for PEDOT:PSS and PPy. Therefore, PEDOT:PSS finds wide application in electrophysiology and biosensing,^[22,23] organic electrochemical transistors (OEECTs) and electrodes for neuronal systems^[14,23,24] as well as for organic electronic ion pumps.^[25,26]

When PEDOT:PSS films interface aqueous electrolyte, water molecules form hydroxide bridges between the PSS backbones, which leads to film swelling. To prevent the decay in electric conductivity, polar organic solvents, such as dimethyl sulfoxide (DMSO) or ethylene glycol (EG), are added to concentrate the conducting PEDOT islands for conductivity improvement.^[27] In case of DMSO the conductivity is two orders of magnitude larger as compared to PEDOT:PSS films in absence of DMSO.^[28] Furthermore, silane-based crosslinkers, such as (3-glycidyloxypropyl) trimethoxysilane (GOPS), are added to enhance stretchability and prevent dissolution and delamination of PEDOT:PSS films in aqueous solutions. Crosslinkers connect PSS backbones with each other and the glass surface.^[29,30] Surfactants, such as Zonyl, improve the adhesion on substrates.

Over the last forty years various semiconducting polymers of p- and n-type have been published.^[31,32] However, the well-established PEDOT:PSS is in great focus with more than 15 000 publications per year^[33], being one of the most studied materials on earth. In the presented works of this thesis PEDOT:PSS is the material of choice as an OEM. Due to the blue colour in doped state and transparent colour in undoped state, PEDOT has also been used as a pixel electrode in electrochromic displays.^[34] Moreover, thanks to its high volumetric capacitance in the order of 40 F cm^{-3} , PEDOT:PSS finds application in ion-based energy storage systems like supercapacitors,^[35] conducting channel of electrochemical transistors^[36] and sensors^[37]. Today, PEDOT:PSS is also widely utilized as hole injecting electrode in organic light emitting diodes,^[38] organic field effect transistors (OFET),^[39] and hole extraction electrode in photovoltaics^[40].

1.1.2 The Base of Bioelectronics: PEDOT:PSS Coated Electrodes

Electrodes are the simplest device architecture and have extensively been studied for bioelectronic applications. Faradaic electrodes, like Ag/AgCl, reacting electrochemically with the electrolyte, are less applicable for biological applications, as the composition of the electrolyte changes and possibly released toxic compounds might harm biological tissue.^[41] On the contrary, the usage of non-faradaic electrodes, like Au, forming an electric double layer (EDL) is preferred for bioelectronic applications. To effectively transduce ionic signals into electronic current, a low impedance at the electrode surface with a high ionic conduction is required. A porous CP film coated on the non-faradaic electrode surface is an attractive solution, having high electronic conductivity and ionic conductance. Moreover, the porous structure lowers the impedance of the electrode. The possibility of electropolymerisation directly on the electrode eliminates photolithographic steps from the process and makes the film thickness finely controllable.^[42] CP coated electrodes, especially PEDOT:PSS, found bioelectronic

applications in neural activity sensing.^[11,12] CP coatings enhance the electrical performance as well as biocompatibility of the electrode-tissue interface.^[24] First *in vivo* experiments to heal diseases affecting the brain have been performed.^[43]

1.1.3 Ion-Gated Organic Transistors

Coming from two-terminal to three-terminal device configurations, ion-gated organic transistors are essential devices in bioelectronics. Compared to conventional organic field-effect transistors (OFETs^[44]), in ion-gated organic transistors the insulator is replaced with an electrolyte and the conductivity of the organic semi-conducting channel is modulated by ions, as shown in **Fig. 1.4**. Depending on the applied gate voltage (V_G), cations ($V_G < 0$ V) or anions ($V_G > 0$ V) are accumulated at the gate-electrolyte interface and a corresponding number of anions or cations are accumulated at the electrolyte-semiconductor interface. More in detail, the ionic charges accumulated at the gate-electrolyte interface screen the charges in the metal gate, while the ionic charges accumulated at the electrolyte-semiconductor interface are electrostatically compensated by the electronic charge carriers (holes or electrons) induced into the semiconductor. In steady-state equilibrium conditions (*viz.* no migration of ionic charges) the interface ionic-electronic charge compensation results in two electrical double layers (EDLs) at the corresponding interfaces (*viz.* gate-electrolyte and electrolyte-semiconductor), which are electrically equivalent to nanometre-thick capacitors. Typical values of the EDL capacitance per unit area are in the range $1 \cdot 10^{-6}$ F cm⁻², *i.e.* more than one order of magnitude larger than that obtained with conventional dielectrics. The large specific capacitance is due to the large permittivity of fluids and small radius of solvated ions (typically < 1 nm). Depending on the electrolyte and organic semiconductor materials, the organic material can be impermeable or permeable to ions. As shown in **Fig. 1.4 b**, in the case ions cannot penetrate the organic material a single electrolyte-semiconductor interface is formed giving rise to the class of electrolyte-gated organic field-effect transistors (EGOFETs).^[45] EGOFETs are used to sense humidity^[46], pH^[47], DNA^[48], penicillin,^[49] dopamine,^[50] ions,^[51] and the reaction of transmembrane proteins of a phospholipid layer.^[52] In the case ions can penetrate the organic semiconductor, the EDL is distributed within the volume of the organic material giving rise to the class of OEECTs, depicted in **Fig. 1.4 c**.

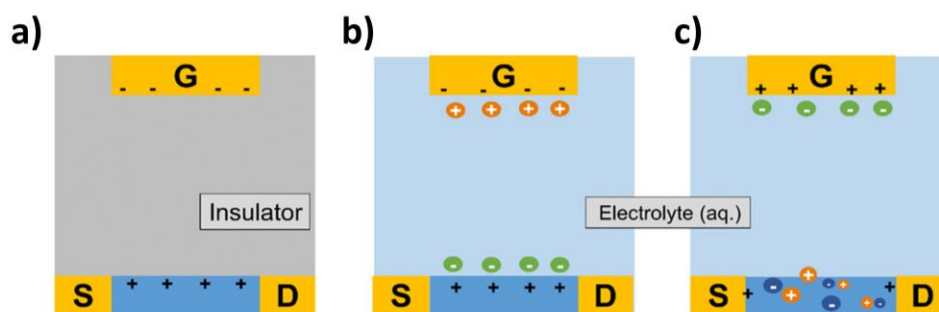


Figure 1.4: Comparison in the device structure of **a)** organic field-effect transistor (OFET), **b)** the electrolyte gated organic field effect transistor (EGOFET), and **c)** the organic electrochemical transistor (OECT).

1.2 The Raising Potential of the Organic Electrochemical Transistor

The first OECTs were developed by the Wrighton group in the 1980s, using polyaniline and poly(3-methylthiophene) as CPs.^[53] In 2002 PEDOT:PSS was introduced by the Berggren group for OECTs and it is till now widely used as channel material for OECTs, especially in bioelectronics.^[19,31,54,55] The OECT with PEDOT:PSS as CP operates in depletion mode. An important advantage of OECT is the volumetric capacitance due to the distributed EDL in the CPs, which results in a large transconductance (g_m), typically in the range of milli siemens, and, in turn, in an enhanced transduction and amplification of ionic signals into electronic currents. We note that the g_m of OECTs is about three orders of magnitude larger than that of OFETs (**Fig. 1.5**).^[22,23] However, the large overall capacitance results in a bandwidth limited to a few kHz, which fortunately is not a major concern in bioelectronic applications. In the following section the already existing and promising future of OECTs in bioelectronics is drawn.

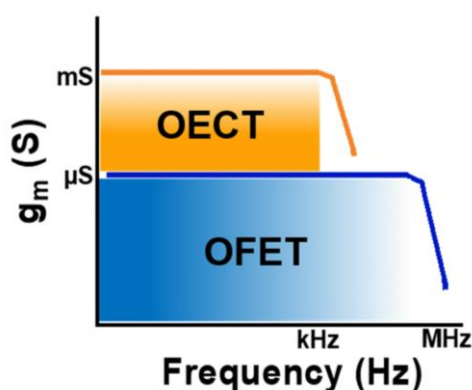


Figure 1.5: Comparison of the OECT and the OFET regarding the transconductance g_m over frequency.

1.2.1 Device Structure: Materials and Fabrication Process

The OECT is a three terminal device consisting of a source and drain electrode, connected by the channel CP (**Fig. 1.6**). The source-drain current I_D is modulated by ions penetrating from the electrolyte into the channel, driven by the gate potential. Typically, source

and drain gold electrodes with a thin chromium adhesion layer below are deposited on a rigid substrate, like glass, using physical vapor deposition. Besides rigid on-chip technology, OEECTs can be fabricated onto flexible substrates, such as PET, due to the mechanical properties of organic electronic materials as channel.^[56] The work of Yao et al. shows that OEECTs on flexible substrates have the advantage to monitor 3D microenvironments and obtain a similar signal-to-noise ratio to the one of OEECTs on rigid substrate.^[56] The merits of flexible OEECTs for *in vivo* sensing are crucial, as first studies on sensing brain activity proved in 2012.^[22] Flexible OEECTs could monitor tissues^[57] and reduce fabrication costs for *in vitro* chips by printing technologies.^[58] Besides aqueous electrolyte, typically defined by a PMMA-well, the possibility to use solid electrolytes, using ionic liquids, offer a great potential for applications, e.g. for wearable electronics, due to its wide variety of processing methods.^[59] The channel geometries are determining the channel's volumetric capacitance. Recently the group of Hsing et al. tuned the sensitivity of the OEECT as an impedance sensor by optimizing the impedance relation of the channel and the integrated cell layer. It was found that an increased channel geometry enhances the sensitivity in the low frequency regime and therefore the suitability to monitor tightly packed cell layers. However, sensing leaky cell layers requires sensitivity in the high frequency regime, which is achieved with a small channel geometry.^[60] The gate electrode is either deposited in plane on the substrate or as a top-electrode, e.g. Ag/AgCl pellet, immersed into the electrolyte.^[61] The voltage drop at the gate/ electrolyte interface should be low, to have an efficient voltage transfer and thus, an efficient ion-to-electron transduction. A voltage loss means a reduction of the sensitivity of the OEECT.^[62] Ag/AgCl as a non-polarizable gate electrode achieves this due to electrochemical reaction of AgCl salt with plain silver or the electrolyte ions.^[63] As a result, Ag/AgCl electrodes are widely used for biosensing short-time measurements.^[56,64] Being easy to handle, but having the drawback of cytotoxic effects of Ag/AgCl on cells in the case of long-term measurements, the applications for top-gated OEECTs for cell integrity are limited due to the formation of toxic Ag nanoparticles.^[65,66] This drawback can be overcome by using a salt bridge, like saturated KCl solution, shielding the diffusion of AgCl into the electrolyte.^[55,67,57] However, top-gated OEECTs are not feasible to be used for *in vivo* applications. On-chip technology can be realized for OEECTs using lateral electrodes, which enables not only *in vitro* but also *in vivo* cell integrity. As explained before polarizable materials, such as gold, are not suitable by themselves, but when coated with the electron-ion conducting polymer PEDOT:PSS,^[68,67] a biocompatible operation and further advantages, such as a facile fabrication process, tunability of the device performance regarding gate and channel

geometries, transparency to simultaneously record optical images, and flexibility to monitor 3D samples, are provided.^[63,69,70,71,72]

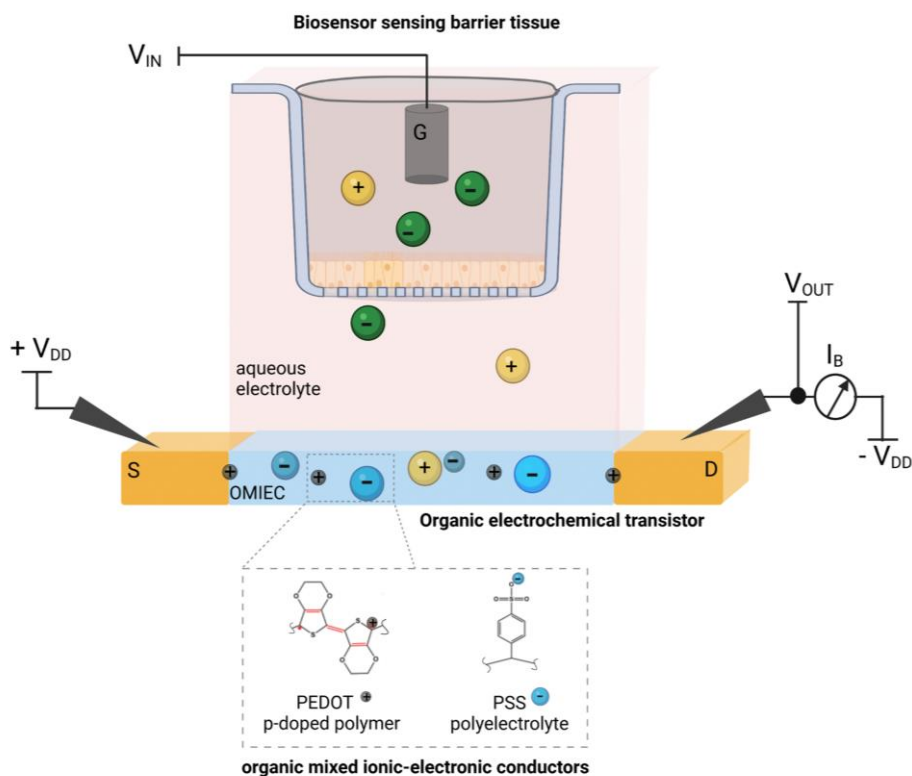


Figure 1.6: Conceptual representation of the OECT as an impedance biosensor. The barrier tissue, seeded in a Transwell-filter and cell medium as electrolyte is integrated between gate and channel. The channel, an organic electronic material (OEM), here PEDOT:PSS, is electrochemically active, thus measured electronic phenomena depend on the ion permeability across the tissue in the electrolyte. Created with biorender.com

1.2.2 Application of the OECT in Biology

Being biocompatible and stable in liquid environment, OECTs are in focus with the rise of bioelectronics.^[9] Three main bioelectronic applications of OECTs are (i) electrophysiology and neural signal recordings,^[73] (ii) analyte detection with a functionalized gate electrode^[31] and (iii) impedance sensing^[74]. Indeed, OECTs can be placed in contact with human skin^[75] for recording electrocardiograms or can be implanted in contact with organs in order to locally-amplify electrophysiological signals from the brain, heart, and muscles,^[76] Works of the OECT in combination with different receptors or selective membranes showed the ability to detect, e.g., ascorbic acid,^[77] marine diatoms in the seawater medium,^[78] dopamine,^[79] acetylcholine, glutamate,^[29] and proteins^[80]. In the last decade, monitoring the integrity of barrier tissue got great attention.^[5] Recently, OECTs found important application for monitoring the barrier tissues, sensing the resistance and capacitance of a cell layer being inserted between the gate and the channel.^[55,64] In this thesis, OECTs are used for monitoring cell layer integrity with enhanced sensitivity.

1.3 The OECT as an Impedance Sensor

1.3.1 The role of Tight Junctions in Barrier Tissues

Detecting disruption or malfunction of tissues is important for toxicological studies.^[61,81] The studying of the reversible loss of barrier function offers great insights for the research on drug delivery and physiology in general. Confluent cell layers and tissues serving as physical barriers are so-called barrier tissues (**Fig. 1.7**). Epithelial barrier tissues cover the internal and external surfaces of organs, e.g. the epidermal covering of skin, kidney, and gastrointestinal tract.^[82] Protein complexes connect the cells of barrier tissue tightly, so that a semipermeable, physical barrier is formed separating the inner to the outer of the organ.^[83] Hence, epithelial barrier tissues regulate the passage of nutrients from organs into blood, but restrict harmful substances.^[84,85] The passage takes place either through cells (transcellular) or between adjacent cells (paracellular).^[84] Epithelial cell layers are categorized in the apical, exposed to the external domain, the lateral, and the basal domain, connected to the matrix of the tissue. In the lateral part, cell-cell junctions are formed by various protein complexes, link the cytoskeleton of adjacent cells and determine the strength of barrier function of cell layers. The apical part facilitates absorption of nutrients. A closer look on the cell-cell junctions reveals four junctional complex types. Whereas for adherent junctions desmosomes are responsible for the cell layer stability, gap junctions enable the interchange of molecules between cells. However, tight junction (TJ) complexes regulate the exchange of ions and molecules paracellular through the barrier tissue by sealing the cell layer. Therefore, TJs define the paracellular barrier function.^[83] In addition, TJs maintain cell polarity, by preventing apical and basal proteins to migrate to the other side.^[83,86] They are dynamically modulated by the intracellular signalling transduction system of cells and a number of extracellular stimuli.^[87,88] Tightness in epithelia alters according to the respective purpose of each tissue. The tightest barrier tissues are the blood-brain-barrier and the skin epithelium. A well-established model for the gastrointestinal tract, important for oral drug delivery is the epithelial colon carcinoma (Caco-2) cell line, found in the small intestine.^[89] Transmembrane TJ complexes, like various claudin, occludin, tricellulin and JAM proteins, mediate cell-cell adhesion, whereas cytoplasmic proteins, such as zonulin proteins, anchor transmembrane junctions to the actin cytoskeleton and are involved in recruiting regulatory proteins.^[90–92]

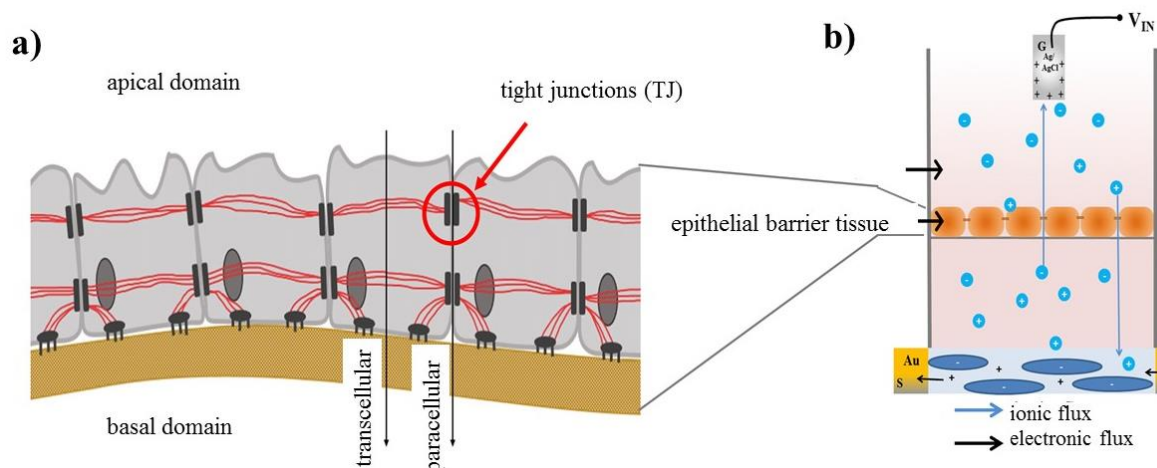


Figure 1.7: The OECT and its application as an impedance sensor. Impedance sensing of barrier tissue (left) on a permeable filter, implemented in the OECT in a self-standing architecture (right). Adapted from Fig. 1 b in Adv. Mater. Technol., 2021 (6).^[108] **a)** Scheme of epithelial cell layer that functions as a physical barrier facilitated by intercellular TJs. The paracellular barrier consists of TJs, adherent junctions, and desmosomes. **b)** Scheme of the OECT device structure with an integrated Transwell filter in presence of cell layers as barrier tissue with TJs in between the cells. PEDOT:PSS as the active area between the gold electrodes, source (S) and drain (D), defines the OECT's geometries: $W = 2$ mm, $L = 1$ mm, $t = 100$ nm. An Ag/AgCl gate electrode (G) and the cell culture medium EMEM is utilized as an electrolyte. Mobile ionic charge carriers are labelled in bright blue, non-mobile PSS-anions in dark blue and holes in black.

The transepithelial resistance (TER) quantifies the barrier functionality of cell layers and tissues as figure-of-merit.^[61,90,93] As an example the TER-value of barrier tissue from Caco-2 cell line is in the order of $\sim 500 \Omega \text{ cm}^2$. Performing transepithelial electrical resistance (TER) measurements with a volt-ohm meter is one possibility to assess TER-values of cell layers. The paracellular conductance is measured using a two-electrode set-up. The basal and apical compartments connecting electrode and electrolyte are separated by a permeable Transwell-filter, on which cells are cultured.^[72,94] Although this method is easy to handle, it suffers from low reproducibility and low temporal resolution.^[61] The more advanced two-terminal frequency-dependent electrochemical impedance spectroscopy (EIS) determines the TER with higher reproducibility and higher sensitivity.^[95] Less time-consuming automated EIS set-ups, such as the CellZScope, were evolved, measuring several samples in parallel.^[96] Optical techniques like immunofluorescence spectroscopy or permeability assays are state-of-the-art techniques to visualize TJ proteins, utilizing antibody staining.^[85,87,93,97] However, due to their invasiveness along with a low temporal resolution, *in vivo* applications are prohibited. Bioelectronics and specifically the OECT offer *in vitro* and *in vivo* impedance sensing with high sensitivity and temporal resolution (**Fig. 1.7**).

To improve drug targeting, the detection and *in-situ* monitoring of TJ modulation becomes crucial (**Fig. 1.8**). Many clinically approved drugs are too big to paracellularly pass across barrier tissue and are repelled from TJs due to their hydrophobic nature, thus prohibiting

1-12 The OECT as an Impedance Sensor

the patient friendly oral intake of drugs.^[90,91] Together with the development of hydrophilic drug delivery systems, agents to regulate the tightness of barrier tissue by manipulating TJ complexes like ethylenediaminetetraacetic acid (EDTA), chitosan, or poly-L-lysine (PLL), so called TJ modulators, are evolved.^[90]

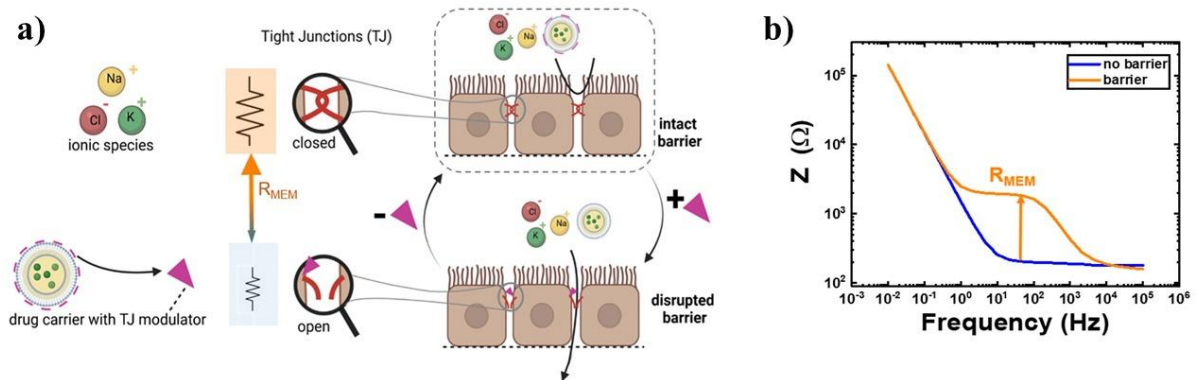


Figure 1.8: Barrier modulation of biological tissue. **a)** Simplified schematic of a biological barrier tissue. The barrier function is defined by tight junctions (TJs), protein complexes between cells ensuring tightness and controlling the paracellular permeability of ions or drug carriers across the barrier. Due to the addition of a TJ modulator, inserted on a drug carrier, TJs open and the tissue loses its resistance of the membrane (R_{MEM}). Created with biorender.com. **b)** Barrier tissue sensed *in vitro* with the organic electrochemical transistor (OECT).measured with electrochemical impedance spectroscopy (EIS).

1.3.2 Benefits of OECTs

The envisioned added value for organic bioelectronics is to replace, where possible, animal models for medical studies. The animal model does not necessarily correctly predict the effect on human tissue, especially regarding neurological diseases such as Alzheimer, epilepsy, or Parkinson. Organic electronics open the possibility to perform experiments using *in vitro* or even *in vivo* human tissue culture, such as brain, liver, lung, kidney, and intestine enabling concise investigations on the effects of therapeutics on our body. Organic bioelectronics together with the growing research knowledge on *in vitro* cell culture of human organ tissue brings hope to overcome the lack of knowledge regarding tumours or infectious diseases due to viruses, like Zika or Covid-19.

The electrical assessing of barrier tissue integrity with the OECT as an impedance sensor was first reported in 2012 by the group of Owens and since then received increasing attention.^[61] The sensitivity of OECTs as an impedance sensor can be enhanced through tuning of channel area according for a broad range of tissue resistance. As mentioned before, the sensitivity of OECTs can be tuned according to the required range of monitored cell barrier resistance.^[72,60] After first time monitoring cell layer integrity with the OECT in the group of Owens in 2012, the OECT established as a validated complementary or alternative method for *in vitro* and future *in vivo* biomedical applications, e.g. monitoring minute changes of tissue

under the effect of toxins.^[64] Utilizing the OECT supported by imaging methods is state-of-the-art and provides valuable insights to understand monitored results on biosensing.^[69,71,98] The group of Owens evolved a fully automated electrical wound-healing assay utilizing OECTs.^[69] Taking advantage of the transparent nature of PEDOT:PSS, the healing process has been simultaneously monitored electrically and optically in this project. In comparison to sheer optical techniques, the OECT offers two advantages, monitoring with higher sensitivity and *in-situ*.^[69] It monitors conformational changes of integrated cells with higher sensitivity and is even able to detect metabolites. The capability to provide real-time measurements of cell structure broadens the range of possibilities to apply the OECT in *in vitro* and *in vivo* research extensively, compared to end-point measurements in case of e.g. immunofluorescence.^[69] The ability to customize the transistor configuration and mechanical properties according to the studied tissue structure is outstanding.^[57,72,99] Research results, such as the integration of a microfluidic platform,^[69] or 3D cardiac tissues^[57] show the potential of OECTs for *in vitro* biosensing. Furthermore, the OECT-based barrier tissue integrity evolved for sensing^[26,60,72,100], controlling and/or monitoring cell growth and tissue formation (**Fig. 1.9 a**).^[61,64,71,101] TJ opening or irreversible disruption using agents, such as hydrogen peroxide, ethanol, EGTA, Salmonella, and silver nanoparticles, has been monitored by transient response measurements.^[55,61,66,67,71,102] Highlighting here the work of Decataldo et al., where the ability of OECTs to assess coating-dependent toxicity of nanoparticles on barrier tissue and non-barrier tissue has been reported.^[66] The recent published work of Yeung et al. showed that the OECT is able to *in-situ* monitor cancer invasion and metastasis of NPC43 cells on Caco-2 cells, using a multichannel recording OECT array.^[103] Utilizing the OECT as an impedance sensor is crucial in the fields of toxicology, drug delivery, infectious disease diagnostics and basic research on molecular biology and electrophysiology of barrier tissue.

1.3.3 Monitoring Barrier Tissue Integrity with the OECT in Standard Configuration

The work of Jimison *et al.* in 2012 represents a milestone in the field of impedance sensing with OECTs.^[61] Sensing the barrier function of tissues *in vitro*, with an integrated tissue between apical and basal electrolyte is of great importance for toxicological and drug delivery studies. Utilizing a permeable Transwell filter, where cells are seeded on a porous membrane, not only enables an easy transfer, but also mimics *in vivo* conditions.^[61] Besides the TER-value accounting for the ion flux through the tissue (R_{MEM}), the ion accumulation at the barrier tissue interface is expressed by the capacitance C_{MEM} (**Fig. 1.9 b**). Furthermore, the ion flux alters with the apical and basal electrolyte resistance R_{AB} , the resistance and the capacitance of the

filter, and the capacitance of the channel C_{CP} . In the well-established standard OECT configuration, the transient response of I_D is measured at a certain V_D by applying a V_G pulse. Minute variations in the paracellular ion flux into the channel are detected in real time by a change in I_D . Jimison *et al.* showed, as displayed in **Fig. 1.9 c**, that the OECT reveals a smaller decay in the transient response of I_D in presence of barrier tissue (solid line) as compared to the transient response in absence of barrier tissue (dashed line), where a larger change in I_D was measured (**Fig. 1.9 c ①**).^[80] OECTs in standard configuration are able to monitor the barrier disruption due to the exposure to toxins, such as H_2O_2 (100 mM), displayed as an overlap with the electrical characteristics of the filter in absence of cells (**Fig. 1.9 c ②**).

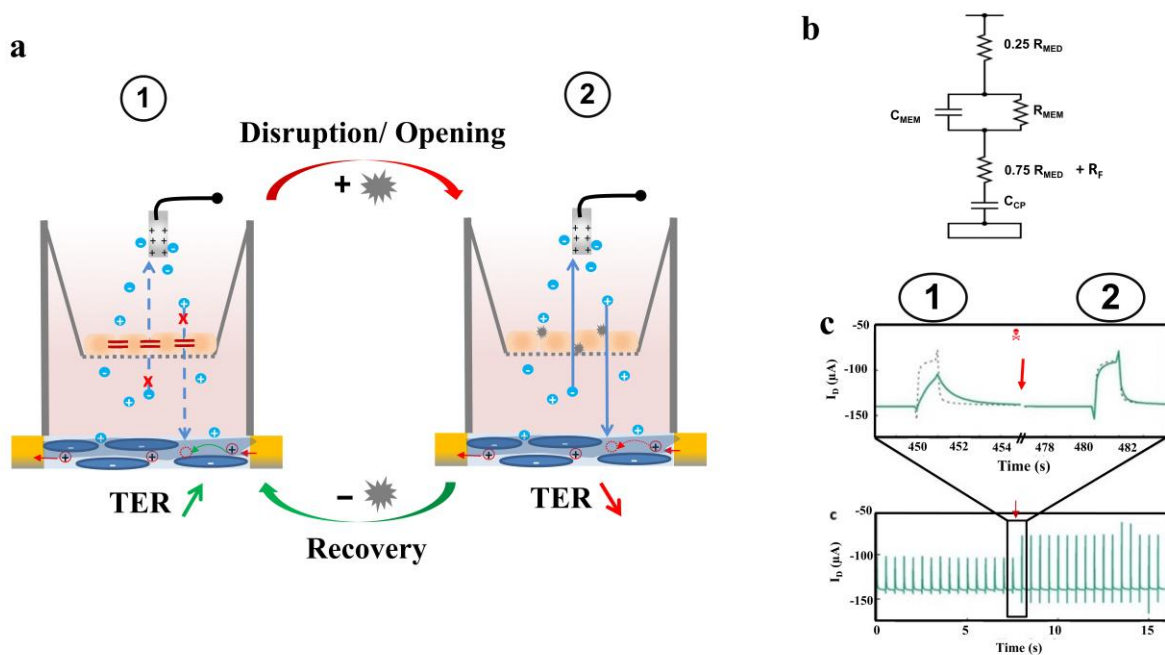


Figure 1.9: Sensing barrier integrity and barrier disruption with the standard OECT configuration. **a)** Schematic of the OECT with integrated tissue as an intact barrier functionality due to the presence of tight junctions (TER high, left) and without barrier function due to the loss of tight junctions (TER low, right). The tight junction modulation is controlled by adding and removing a chemical agent. All images reproduced with permission.^[108] Copyright 2021, Wiley-VCH. **b)** Electronic circuit describing ionic transport between gate electrode and transistor channel. R_M and C_M refers to the trans-epithelial resistance and the capacitance of the cell layer, respectively. R_F relates to the resistance of the permeable Transwell filter. R_{AB} refers to the resistance of the permeable filter and cell culture media. C_{CP} refers to the capacitance of PEDOT:PSS as conducting polymer in the channel. Reproduced with permission.^[61] Copyright 2012, Wiley-VCH. **c)** Transfer characteristics of the transient response of I_D to a V_G pulse, where $V_G = 0.3$ V was applied for 1 s and off for 29 s, and at a constant $V_D = -0.1$ V. ① Monitoring barrier tissue integrity by measuring the response of I_D (solid line) in contrast to the reference, response of I_D in absence of cells (dashed lines). The red arrow indicates the time H_2O_2 was added. ② Monitoring the disruption of barrier tissue by measuring the response of I_D with an integrated barrier tissue after the addition of 100 mM H_2O_2 (solid lines) in contrast to the reference (dashed lines). Over all, the OECT response was measured *in-situ* for periodic square V_{GS} pulses over 15 min. Reproduced with permission.^[61] Copyright 2012, Wiley-VCH.

In general, with an increase in permeability the TER-value decreases.^[104] The standard OECT configuration displays a sufficiently high sensitivity to distinguish the concentration dependent barrier disruption as a change in I_D due to the exposure to a series of H_2O_2

concentrations (100, 50, 5, 1) mM in real time (**Fig. 1.10 a**). Furthermore, the standard OECT is applicable as a sensitive sensor for milder barrier disruption due to the less toxic compound ethanol (EtOH) for several concentrations (30, 20, and 10) % (**Fig. 1.10 b**). The work benchmarked the transient response measurement of I_D using the OECT in standard configuration to assess barrier tissue integrity and barrier disruption in real time and to distinguish concentration-dependent toxicity. Thus, the OECT impedance sensor found its application in evaluating toxicology of chemicals.

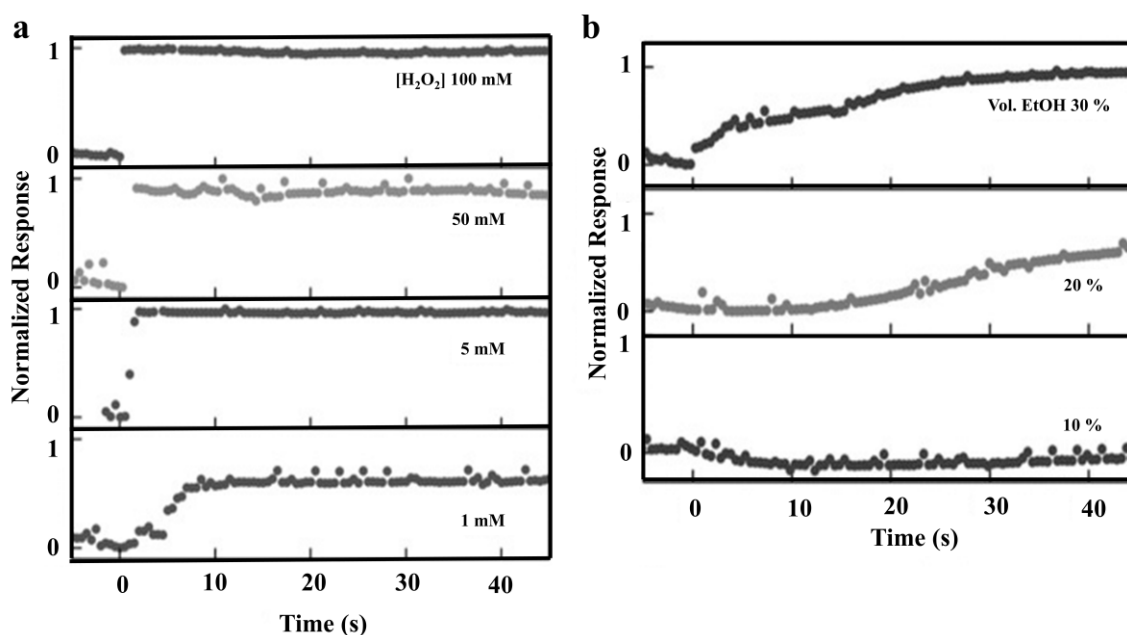


Figure 1.10: Monitoring barrier tissue disruption with the OECT *in-situ* due to the addition of toxins. The normalized response (NR) is obtained by calculating $\Delta I_D / I_0$ (where ΔI_D refers to drain current modulation in response to the application of V_G , and I_0 refers to the drain current when V_G is off) and subsequently normalizing the dataset to [0, 1]. **a)** Change in the normalized response (NR) after the addition of H₂O₂ at $t = 0$ s for several concentrations (100, 50, 5, and 1) mM. Here, NR = 0 corresponds to full barrier properties of a confluent monolayer and a NR = 1 corresponds to a cell layer with no barrier properties. Reproduced with permission.^[61] Copyright 2012, Wiley-VCH. **b)** Change in the NR after the addition of EtOH at $t = 0$ s for volume concentrations of 30, 20, and 10 %. Reproduced with permission.^[61] Copyright 2012, Wiley-VCH.

1.4 References

- [1] M. Prentki, T. J. Biden, D. Janjic, R. F. Irvine, M. J. Berridge, C. B. Wollheim, *Nature* **1984**, *309*, 562.
- [2] A. Carlsson, *Adv. Neurol.* **1993**, *60*, 1.
- [3] J. D. Watson, F. H. C. Crick, *Nature* **1953**, *171*, 737.
- [4] L. Pauling, C. Niemann, *J. Am. Chem. Soc.* **1939**, *61*, 1860.
- [5] M. Ramuz, A. Hama, M. Huerta, J. Rivnay, P. Leleux, R. M. Owens, *Adv. Mater.* **2014**, *26*, 7083.
- [6] S. Tria, L. H. Jimison, A. Hama, M. Bongo, R. M. Owens, *Biosensors* **2013**, *44*.
- [7] a) J. P. Giraldo, M. P. Landry, S. M. Faltermeier, T. P. McNicholas, N. M. Iverson, A. A. Boghossian, N. F. Reuel, A. J. Hilmer, F. Sen, J. A. Brew et al., *Nat. Mater.* **2014**, *13*, 400; b) E. Stavriniidou, R. Gabrielsson, E. Gomez, X. Crispin, O. Nilsson, D. T. Simon, M. Berggren, *Sci. Adv.* **2015**, *1*, e1501136.
- [8] a) D. R. Lovley, *Annu. Rev. Microbiol.* **2012**, *66*, 391; b) A. Operamolla, R. Ragni, F. Milano, R. R. Tangorra, A. Antonucci, A. Agostiano, M. Trotta, G. Farinola, *J. Mater. Chem. C* **2015**, *3*, 6471.
- [9] D. T. Simon, E. O. Gabrielsson, K. Tybrandt, M. Berggren, *Chem. Rev.* **2016**, *116*, 13009.
- [10] a) J. Y. Wong, R. Langer, D. E. Ingber, *Proc. Natl. Acad. Sci. USA* **1994**, *91*, 3201; b) C. E. Schmidt, V. R. Shastri, J. P. Vacanti, R. Langer, *Proc. Natl. Acad. Sci. USA* **1997**, *94*, 8948.
- [11] X. Y. Cui, J. F. Hetke, J. A. Wiler, D. J. Anderson, D. C. Martin, *Sens. Actuators, A* **2001**, *93*, 8.
- [12] X. Y. Cui, V. A. Lee, Y. Raphael, J. A. Wiler, J. F. Hetke, D. J. Anderson, D. C. Martin, *J. Biomed. Mater. Res.* **2001**, *56*, 261.
- [13] a) D. H. Kim, M. Abidian, D. C. Martin, *J. Biomed. Mater. Res.* **2004**, *71A*, 577; b) T. Nyberg, O. Inganas, H. Jerregard, *Biomed. Microdevices* **2002**, *4*, 43.
- [14] X. Cui, D. C. Martin, *Sensors and Actuators B: Chemical* **2003**, *89*, 92.
- [15] M. Asplund, H. von Holst, O. Inganas, *Biointerphases* **2008**, *3*, 83.
- [16] C. Weidlich, K. M. Mangold, K. Juttner, *Electrochim. Acta* **2005**, *50*, 1547.
- [17] J. Xia, N. Masaki, K. J. Jiang, S. Yanagida, *J. Mater. Chem.* **2007**, *17*, 2845.
- [18] a) G. Heywang, F. Jonas, *Adv. Mater.* **1992**, *4*, 116; b) L. Groenendaal, F. Jonas, D. Freitag, H. Pielartzik, J. R. Reynolds, *Adv. Mater.* **2000**, *12*, 481.
- [19] J. Rivnay, P. Leleux, M. Sessolo, D. Khodagholy, T. Hervé, M. Focchi, G. G. Malliaras, *Adv. Mater.* **2013**, *25*, 7010.
- [20] A. Malti, J. Edberg, H. Granberg, Z. U. Khan, J. W. Andreasen, X. J. Liu, D. Zhao, H. Zhang, Y. L. Yao, W. Brill et al., *Adv. Sci.* **2016**, *3*.
- [21] a) G. C. Li, P. G. Pickup, *Phys. Chem. Chem. Phys.* **2000**, *2*, 1255; b) J. Bobacka, A. Lewenstam, A. Ivaska, *J. Electroanal. Chem.* **2000**, *489*, 17.
- [22] D. Khodagholy, T. Doublet, P. Quilichini, M. Gurfinkel, P. Leleux, A. Ghestem, E. Ismailova, T. Hervé, S. Sanaur, C. Bernard et al., *Nat. Commun.* **2013**, *4*, 1575.
- [23] J. Rivnay, P. Leleux, M. F. Ferro, M. Sessolo, A. Williamson, D. Koutsouras, D. Khodagholy, M. Ramuz, X. Stakosias, R. M. Owens et al., *Sci. Adv.* **2015**, *1*, e1400251.
- [24] N. K. Guimard, N. Gomez, C. E. Schmidt, *Progress in Polymer Science* **2007**, *32*, 876.
- [25] a) J. Isaksson, P. Kjäll, D. Nilsson, N. D. Robinson, M. Berggren, A. Richter-Dahlfors, *Nat. Mater.* **2007**, *6*, 673; b) A. Williamson, J. Rivnay, L. Kergoat, A. Jonsson, S. Inal, I. Uguz, M. F. Ferro, A. Ivanov, T. A. Sjöström, D. T. Simon et al., *Adv. Mater.* **2015**, *27*, 3138; c) D. T. Simon, S. Kurup, K. C. Larsson, R. Hori, K. Tybrandt, M. Gojny, E. W. H. Jager, M. Berggren, B. Canlon, A. Richter-Dahlfors, *Nat. Mater.* **2009**, *8*, 742.

- [26] A. Jonsson, Z. Song, D. Nilsson, B. A. Meyerson, D. T. Simon, B. Linderöth, M. Berggren, *Sci. Adv.* **2015**, *1*, 1500039.
- [27] J. Y. Kim, J. H. Jung, D. E. Lee, J. Joo, *Synth. Met.* **2002**, *126*, 311.
- [28] H. Shi, C. Liu, Q. Jiang, J. Xu, *Adv. Electron. Mater.* **2015**, *1*, 1500017.
- [29] L. Kergoat, B. Piro, D. T. Simon, M. C. Pham, V. Noël, M. Berggren, *Adv. Mater.* **2014**, *26*, 5658.
- [30] a) E. Stavrinidou, P. Leleux, H. Rajaona, D. Khodagholy, J. Rivnay, M. Lindau, S. Sanaur, G. G. Malliaras, *Adv. Mater.* **2013**, *25*, 4488; b) O. Berezhetska, B. Liberelle, G. De Crescenzo, F. Cicoira, J., *Mater. Chem. B* **2015**, *3*, 5087.
- [31] J. Rivnay, S. Inal, A. Salleo, R. M. Owens, M. Berggren, G. G. Malliaras, *Nat Rev Mater* **2018**, *3*, 99.
- [32] a) O. I. E. Zeglio, *Adv. Mater.* **2018**, *0*, e1800941; b) E. Zeglio, M. Vagin, C. Musumeci, F. N. Ajjan, R. Gabrielsson, X. T. Trinh, N. T. Son, A. Maziz, N. Solin, O. Inganäs, *Chem. Mater.* **2015**, *27*, 6385; c) S. Inal, J. Rivnay, P. Leleux, M. Ferro, M. Ramuz, J. C. Brendel, M. M. Schmidt, M. Thelakkat, G. G. Malliaras, *Adv. Mater.* **2014**, *26*, 7450; d) A. Giovannitti, C. B. Nielsen, D.-T. Sbircea, S. Inal, M. Donahue, M. R. Niazi, D. A. Hanifi, A. Amassian, G. G. Malliaras, J. Rivnay, I. McCulloch, *Nat. Commun.* **2016**, *7*, 13066; e) H. Sun, M. Vagin, S. Wang, X. Crispin, R. Forchheimer, M. Berggren, S. Fabiano, *Adv. Mater.* **2018**, *30*, 1704916.
- [33] Y. Wen, J. Xu, J., *Polym. Sci., Part A: Polym. Chem.* **2017**, *55*, 1121.
- [34] a) H. Shi, C. Liu, Q. Jiang, J. Xu, *Adv. Funct. Mater.* **2015**, *1*, 1500017; b) P. Tehrani, L.-O. Hennerdal, A. L. Dyer, J. R. Reynolds, M. Berggren, *J. Mater. Chem.* **2009**, *19*, 1799; c) Q. Pei, G. Zuccarello, M. Ahlskog, O. Inganäs, *Polymers* **1994**, *35*, 1347; d) ACREO, zu finden unter <https://www.acreo.se/expertise/printed-electronic-technologies>.
- [35] a) J. F. Franco-Gonzalez, N. Rolland, I. V. Zozoulenko, *ACS Appl. Mater. Interfaces* **2018**, *10*, 29115; b) N. Rolland, J. F. Franco-Gonzalez, R. Volpi, M. Linares, I. V. Zozoulenko, *Phys. Rev. Mater.* **2018**, *2*, 45605.
- [36] M. Modarresi, J. F. Franco-Gonzalez, I. Zozoulenko, *Phys. Chem. Chem. Phys.* **2018**, *20*, 17188.
- [37] K. Tybrandt, I. V. Zozoulenko, M. Berggren, *Sci. Adv.* **2017**, *3*, eaao3659.
- [38] M. Cai, Z. Ye, T. Xiao, R. Liu, Y. Chen, R. W. Mayer, R. Biswas, *Adv. Mater.* **2012**, *24*, 4337.
- [39] N. Stutzmann, R. H. Friend, H. Sirringhaus, *Sci. Adv.* **2003**, *299*, 1881.
- [40] K. Sun, S. Zhang, P. Li, Y. Xia, X. Zhang, D. Du, F. H. Isikgor, J. Ouyang, *J. Mater. Sci.: Mater. Electron.* **2015**, *26*, 4438.
- [41] D. R. Merrill, M. Bikson, J. G. R. Jefferys, *J. Neurosci. Methods* **2005**, *141*, 171.
- [42] M. Asplund, T. Nyberg, O. Inganäs, *Polym. Chem.* **2010**, *1*, 1374.
- [43] C. J. Bettinger, M. Ecker, T. D. Yoshida Kozai, G. G. Malliaras, W. Voit, *MRS Bulletin* **2020**, *45*, 655.
- [44] A. Tsumura, H. Koezuka, T. Ando, *Appl. Phys. Lett.* **1986**, *49*, 1210.
- [45] A. Laiho, L. Herlogsson, R. Forchheimer, X. Crispin, M. Berggren, *Proc. Natl. Acad. Sci.* **2011**, *108*, 15069.
- [46] a) Z. T. Zhu, J. T. Mason, R. Dieckmann, G. G. Malliaras, *Appl. Phys. Lett.* **2002**, *81*, 4643; b) L. Torsi, A. Dodabalapur, N. Cioffi, L. Sabbatini, Zamboni, *Sens. Actuators, B* **2001**, *77*, 7; c) D. Li, E. J. Borkent, R. Nortrup, H. Moon, H. Katz, Z. Bao, *Appl. Phys. Lett.* **2005**, *86*, 42105.
- [47] C. Batic, B. Palan, A. Campitelli, G. Borghs, *Sens. Actuators, B* **2002**, *83*, 115.
- [48] L. Kergoat, B. Piro, M. Berggren, M. Pham, A. Yassar, G. Horowitz, *Org. Electron.* **2012**, *13*, 1.
- [49] F. Buth, A. Donner, M. Stutzmann, J. A. Garrido, *Proc. SPIE* **2012**, *8479*, 84790M.

- [50] S. Casalini, F. Leonardi, T. Cramer, F. Biscarini, *Org. Electron.* **2013**, *14*, 156.
- [51] A. Loi, I. Manunza, A. Bonfiglio, *Appl. Phys. Lett.* **2005**, *86*, 103512.
- [52] a) S. Cotrone, M. Ambrico, H. Toss, M. D. Angione, M. Magliulo, A. Mallardi, M. Berggren, G. Palazzo, G. Horowitz, T. Ligonzo et al., *Org. Electron.* **2012**, *13*, 638; b) K. S. Narayan, B. N. Madhushankar, V. Gautam, S. P. Senanayak, R. Shivanna, *IEEE Electron Device Lett.* **2013**, *34*, 310; c) T. Someya, H. E. Katz, A. Gelperin, A. J. Lovinger, A. Dodabalapur, *Appl. Phys. Lett.* **2002**, *81*, 3079.
- [53] a) E. W. Paul, A. J. Ricco, M. S. Wrighton, *J. Phys. Chem.* **1985**, *89*, 1441; b) X. Strakosas, M. Bongo, R. M. Owens, *J. Appl. Polym. Sci.* **2015**, *132*, 41735.
- [54] Nilsson, D., Kugler, T., Svensson, P. O. & Berggren, M., *Sens. Actuators B* **2002**, *86*, 193.
- [55] S. A. Tria, M. Ramuz, M. Huerta, P. Leleux, J. Rivnay, L. H. Jimison, A. Hama, G. G. Malliaras, R. M. Owens, *Adv. Healthcare Mater.* **2014**, *3*, 1053.
- [56] C. Yao, Q. Li, J. Guo, F. Yan, I. M. Hsing, *Adv. Healthcare Mater.* **2015**, *4*, 528.
- [57] X. Gu, S. Y. Yeung, A. Chadda, E. N. Y. Poon, K. R. Boheler, I. M. Hsing, *Adv. Biosys.* **2019**, *3*, 1800248.
- [58] J. Rivnay, R. M. Owens, G. G. Malliaras, *Chem. Mater.* **2014**, *26*, 679.
- [59] M. Sophocleous, L. Contat-Rodrigo, E. Garcia-Breijo, J. Georgiou, *IEEE Sensors* **2021**, *21*, 3977.
- [60] Yeung, S., Y., X. Gua, C. M. Tsangb, S. W. Tsaoc, I. M. Hsing, *Sens. Act. A* **2019**, *287*, 185.
- [61] L. H. Jimison, S. A. Tria, D. Khodagholy, Gurfinkel M., E. Lanzarini, A. Hama, G. G. Malliaras, R. M. Owens, *Adv. Mater.* **2012**, *24*, 5919.
- [62] F. Cicoira, M. Sessolo, O. Yaghmazadeh, DeFranco, J. A., Yang, S. Y., *Adv. Mater.* **2010**, *22*, 1012.
- [63] M. Ramuz, K. Margita, A. Hama, P. Leleux, J. Rivnay, I. Bazin, R. M. Owens, *ChemPhysChem* **2015**, *16*, 1210.
- [64] S. T. Tria, L. H. Jimison, A. Hama, M. Bongo, R. M. Owens, *Biochem. Biophys. Acta* **2013**, *1830*, 4381.
- [65] a) C. Greulich, S. Kittler, M. Epple, G. Muhr, M. Köller, *Langenbecks Arch. Chir.* **2009**, *394*, 495; b) S. Kittler, C. Greulich, J. Diendorf, M. Koller, M. Epple, *Chem. Mater.* **2010**, *22*, 4548.
- [66] F. Decataldo, M. Barbalinardo, D. Gentili, M. Tessarolo, M. Calienni, M. Cavallini, B. Fraboni, *Adv. Biosys.* **2020**, *4*, 19000204.
- [67] C. Yao, C. Xie, P. Lin, F. Yan, P. Huang, I. M. Hsing, *Adv. Mater.* **2013**, *25*, 6575.
- [68] P. Lin, F. Yan, J. Yu, H. L. W. Chan, M. Yang, *Adv. Mater. Technol.* **2010**, *22*, 3655.
- [69] V. F. Curto, B. Marchiori, A. Hama, A.-M. Pappa, M. P. Ferro, M. Braendlein, J. Rivnay, M. Fiochi, G. G. Malliaras, M. Ramuz et al., *Microsys. Nanoengin.* **2017**, *3*, 17028.
- [70] a) F. Decataldo, V. Druet, A.-P. Pappa, E. Tan, A. Savva, C. Pitsalidis, S. Inal, J.-S. Kim, B. Fraboni, R. M. Owens et al., *Flex. Print. Electron.* **2019**, *4*, 44006; b) C. M. Proctor, J. Rivnay, G. G. Malliaras, *J. Polymer Sci. B: Polymer Phy.* **2016**, *54*, 1433; c) Y. Liang, M. Ernst, F. Brings, D. Kireev, V. Maybeck, A. Offenhäusser, D. Mayer, *Adv. Healthcare Mater.* **2018**, *7*, 1800304.
- [71] M. Ramuz, A. Hama, J. Rivnay, P. Leleux, R. M. Owens, *J. Mater. Chem. B* **2015**, *3*, 5971.
- [72] F. Decataldo, M. Barbalinardo, M. Tessarolo, V. Vurro, M. Calienni, D. Gentili, F. Valle, M. Cavallini, B. Fraboni, *Adv. Mater. Technol.* **2019**, *4*, 1900207.
- [73] a) D. Koutsouras, A. Hama, J. Pas, P. Gkoupidenis, B. Hivert, C. Faivre-Sarrahil, Pasquale E., R. M. Owens, G. G. Malliaras, *MRS Communications* **2017**, *7*, 259; b) J. Pas, C. Pitsalidis, D. A. Koutsouras, P. P. Quilichini, F. Santoro, B. Cui, L. Gallais, R.

- P. O'Connor, G. G. Malliaras, R. M. Owens, *Advanced Biosystems* **2018**, 2, 170014; c) P. Gkoupidenis, N. Schaefer, X. Strakosas, J. Fairfield, G. G. Malliaras, *Appl. Phys. Lett.* **2015**, 107, 263302; d) P. Gkoupidenis, D. A. Koutsouras, G. G. Malliaras, *Nat. Commun.* **2017**, 8, 15448.
- [74] N. Y. Shim, D. A. Bernardis, D. J. Macaya, J. A. DeFranco, M. Nikolou, R. M. Owens, G. G. Malliaras, *Sensors* **2009**, 9, 9896.
- [75] A. Campana, T. Cramer, D. T. Simon, M. Berggren, F. Biscarini, *Adv. Mater.* **2014**, 26, 3874.
- [76] W. Lee, D. Kim, J. Rivnay, N. Matsuhisa, T. Lonjaret, T. Yokota, H. Yawo, M. Sekino, G. G. Malliaras, T. Someya, *Adv. Mater.* **2016**, 28, 9722.
- [77] I. Gualandi, M. Marzocchi, E. Scavetta, M. Calienni, A. Bonfiglio, B. Fraboni, *J. Mater. Chem. B* **2015**, 3, 6753.
- [78] J. Liao, S. Lin, K. Liu, Y. Yang, R. Zhang, W. Du, X. Li, *Sens. Actuators B* **2014**, 203, 677.
- [79] H. Tang, P. Lin, H. L. W. Chan, F. Yan, *Biosens. Bioelectron.* **2011**, 26, 4559.
- [80] E. Macchia, P. Romele, K. Manoli, M. Ghittorelli, M. Magliulo, Z. M. Kovács-Vajna, F. Torricelli, L. Torsi, *Flexible Printed Electron.* **2018**, 3, 34002.
- [81] L. V. Lingstedt, M. Ghittorelli, M. Brückner, J. Reinholz, N. I. Crăciun, F. Torricelli, V. Mailänder, P. Gkoupidenis, P. W. M. Blom, *Adv. Healthcare Mater.* **2019**, 8, e1900128.
- [82] J. M. Anderson, M. S. Balda, Fanning A. S., *Current Opinion in Cell Biology* **1993**, 5, 772.
- [83] M. G. Farquhar, G. E. Palade, *J. Cell Biol.* **1963**, 17, 375.
- [84] J. M. Anderson, C. M. van Itallie, *Current Biology* **1999**, 9, R922-R924.
- [85] J. M. Anderson, *News Physiol. Sci.* **2001**, 16, 126.
- [86] a) L. González-Mariscal, P. Nava, S. Hernandez, *The J. of Membrane Bio.* **2005**, 207, 55; b) T. Suzuki, *Cell. Mol. Life Sci.* **2013**, 70, 631.
- [87] J. M. Anderson, B. R. Stevenson, D. A. Goodenough, M. S. Mooseker, *J. Cell Biol.* **1986**, 103, A71.
- [88] a) J. M. Anderson, *News Physiol. Sci.* **2001**, 16, 126; b) A. S. Fanning, Mitic L., J. M. Anderson, *J. Am Soc. Nephrol.* **1999**, 10, 1337.
- [89] F. Ingels, S. Deferme, N. Delbar, M. Oth, P. Augustijns, *J. Pharm. Belg.* **2002**, 57, 153.
- [90] M. A. Deli, *Biochemica et Biophysica Acta* **2009**, 1788, 892.
- [91] L. Gonzalez-Mariscal, *Tight junctions*, Landes Bioscience and Springer Science Business Media, LLC, **2006**.
- [92] A. Fasano, *Physiol. Rev.* **2011**, 91, 151.
- [93] K. Sonaje, E.-Y. Chuang, K.-J. Lin, T.-C. Yen, F.-Y. Su, M. T. Tseng, H.-W. Sung, *Molecular pharmaceuticals* **2012**, 9, 1271.
- [94] B. Srinivasan, A. R. Kolli, M. B. Esch, H. E. Abaci, M. L. Shuler, J. J. Hickman, *Journal of Laboratory Automation* **2015**, 20, 107.
- [95] D. A. Koutsouras, L. V. Lingstedt, K. Lieberth, J. Reinholz, V. Mailänder, P. W. M. Blom, P. Gkoupidenis, *Adv. Healthcare Mater.* **2019**, 8, 1901215.
- [96] a) J. Wegener, D. Abrams, W. Willenbrink, H. J. Galla, A. Janshoff, *BioTechniques* **2004**, 37, 590; b) J. Wegener, C. R. Keese, I. Giaever, *Experimental cell research* **2000**, 259, 158.
- [97] a) K. Matter, M. S. Balda, *Int. Rev. Cytol.* **1999**, 1861, 117; b) A. S. Fanning, van Itallie C.M., J. M. Anderson, *Molecular Biology of the Cell* **2012**, 23, 577.
- [98] A. M. Pappa, H. Y. Liu, W. Traberg-Christensen, Q. Thiburce, A. Savva, A. Pavia, A. Salleo, S. Daniel, R. M. Owens, *ACS nano* **2020**, 14, 12538.
- [99] a) A. M. D. Wan, S. Inal, T. Williams, K. Wang, P. Leleux, L. Estevez, E. P. Giannelis, C. Fischbach, G. G. Malliaras, D. Gourdon, *J. Mater. Chem. B* **2015**, 3, 5040; b) S. Inal,

- A. Hama, M. Ferro, C. Pitsalidis, J. Oziat, D. Iandolo, A.-M. Pappa, M. Hadida, M. Huerta, D. Marchat et al., *Adv. Biosys.* **2017**, *1*, 1700052.
- [100] D. Gentili, P. D'Angelo, F. Militano, R. Mazzei, T. Poerio, M. Brucale, G. Tarabella, S. Bonetti, S. L. Marasso, M. Cocuzza et al., *J. Mater. Chem. B* **2018**, *6*, 5400.
- [101] a) M. H. Bolin, K. Svennersten, D. Nilsson, A. Sawatdee, E. W. Jager, A. Richter-Dahlfors, M. Berggren, *Adv. Mater.* **2009**, *21*, 4379; b) G. Tarabella, A. G. Balducci, N. Coppedè, S. L. Marasso, P. D'Angelo, S. Barbieri, M. Cocuzza, P. Colombo, F. Sonvico, R. Mosca et al., *Biochim. Biophys. Acta* **2013**, *1830*, 4374.
- [102] S. A. Tria, M. Ramuz, L. H. Jimison, A. Hama, R. M. Owens, *Journal of Visualized Experiments* **2014**, *84*, 2.
- [103] S. Y. Yeunga, X. Gua, C. M. Tsang, S. W. G. Tsaoc, I. M. Hsing, *Sensors & Actuators: B. Chemical* **2019**, *297*, 126761.
- [104] a) M. S. Balda, J. A. Whitney*, C. Flores*, S. Gonzilez, M. Cereijido*, K. Matter, *The Journal of Cell Biology* **1996**, *134*, 1031; b) W. C. Prozialeck, J. R. Edwards, P. C. Lamar, C. S. Smith, *Toxicology in vitro* **2006**, *20*, 942.

2 Enhanced Ion Sensitive Current-Driven OECT Configuration

The transient OECT current can be used to detect changes in the impedance of cell layers, as shown by Jimison et al.^[1] To circumvent the application of a high gate bias and preventing electrolysis of the electrolyte, regarding small impedance variations, an alternative measuring technique based on an OECT in a current-driven configuration has been recently developed and presented in this chapter.^[2] The ion-sensitivity of the current-driven OECT is larger than $1200 \text{ mV V}^{-1} \text{ dec}^{-1}$ at low operating voltage. It can be even further enhanced using an OECT based complementary amplifier, which consists of a p-type and an n-type OECT connected in series, as known from digital electronics.^[3] The monitoring of barrier tissue integrity and irreversible disruption of barrier function with the current-driven OECT is demonstrated for an epithelial Caco-2 cell layer, showing the enhanced ion-sensitivity as compared to the standard OECT configuration.^[4] Furthermore, the motivation and outline of this dissertation is presented.

2.1 Highly-Sensitive ion Detection at low Voltages with Current-Driven OEECTs

The OEECT in standard configuration is a sensitive method to detect the presence of a barrier tissue. However, state-of-the-art transistor-based approaches have an intrinsic trade-off between sensitivity, ion concentration range and operating voltage.^[5] The current-driven configuration provides a simple yet effective approach overcoming this fundamental limit. **Fig. 2.1 a** and **b** show the schematic three-dimensional structure and the corresponding circuit of an OEECT connected in a current-driven configuration. The current-driven configuration resembles an inverter-topology, where the pull-down transistor is replaced with a current generator (I_B). In this configuration, the source is connected to the supply voltage V_{DD} , the drain is the output voltage V_{OUT} , while the input voltage V_{IN} is applied to the gate ($V_G = V_{IN}$).^[2] The V_{IN} - V_{OUT} electrical characteristics of the current-driven OEECT configuration can be related to the OEECT parameters and current bias I_B as follows:

$$V_{OUT} = V_{DD} - I_B r_{channel} \quad (1)$$

The channel resistance depends on the operating region of the OEECT. When the current-driven OEECT is biased between negative V_{IN} and $V_{IN} = 0$, anions are injected into the CP, the hole concentration in the polymer is increased, and the OEECT operates in the linear region. According to the Bernard-Malliaras model^[6] the drain current then reads:

$$I_D = k_n \left[(V_T - V_{GS})V_{SD} + \frac{V_{SD}^2}{2} \right] \quad (2)$$

where $k_n = W \cdot t \cdot C_v \cdot \mu \cdot L^{-1}$, W , L and t is the channel width, length and thickness, respectively, C_v is the volumetric capacitance and μ the mobility. In the current driven configuration $V_{GS} = V_{IN} - V_{DD}$, $V_{SD} = V_{DD} - V_{OUT}$ and the OEECT channel resistance results:

$$r_{channel(lin)} \cong \frac{1}{k_n(V_{DD} + V_T - V_{IN})} \quad (3)$$

Combining Eqs. (1) and (3) results:

$$V_{OUT} = V_{DD} - \frac{I_B}{k_n(V_{DD} + V_T - V_{IN})} \quad (4)$$

Eq. (4) shows that when V_{OUT} depends on the supply voltage V_{DD} , on the bias current I_B , on the input voltage V_{IN} , and the OEECT parameters k_n and V_T . In the current driven configuration I_B is a design variable that enables the low-voltage operation independently of the ion concentration of the electrolyte, as displayed in **Fig. 2.1 c**, and/or the specific biological properties of the cell layer.^[3,4,7] When V_{IN} is small, the OEECT channel resistance is small and $V_{OUT} \cong V_{DD}$. Eq. (4) also shows that V_{OUT} decreases by increasing V_{IN} . When $V_{OUT} < V_{IN} - V_T$ the OEECT operates in saturation region and the drain current reads ^[6]:

$$I_D = k_n(V_T - V_{GS})(1 + \lambda V_{SD}) \quad (5)$$

where λ is the channel length modulation. When the OEECT operates in saturation, its output resistance is large, since it behaves like a current generator and hence V_{SD} is large. Combining Eq. (1) with (5) and considering the current-driven topology, the output voltage reads:

$$V_{OUT} \cong V_{DD} - \frac{I_B}{\lambda k_n (V_{DD} - V_{IN} + V_T)^2} \quad (6)$$

We note that in the case of OEECTs λ is typically smaller than 10^{-3} V^{-1} and this explain the large variation of V_{OUT} when V_{IN} is closed to the switching voltage V_{SW} . Indeed, when the OEECT is operating in salutation region, the current-driven OEECT operates as a common-source amplifier and its voltage gain $\delta V_{OUT}/\delta V_{IN} = g_m r_{channel(sat)}$ which corresponds to the intrinsic gain of the transistor.^[8]

The figure of merit of a current-driven OEECT is the switching voltage V_{SW} . Previous work with focused on ion detection with a current-driven OEECT demonstrated a sensitivity of up to $\Delta V_{SW}/\Delta c = 516 \text{ mV dec}^{-1}$, extracted from measured transfer characteristics at various NaCl concentrations, as shown in **Fig. 2.1 d**. This was more than one order of magnitude larger than the Nernst limit, also exceeding the sensitivity of several state-of-the-art ion-sensitive transistors, including Si ISFETs, ZnO FETs, a-IGZO double gate FETs, Si nanowire FETs, graphene FETs, EGOFETs, and OEECTs in standard configuration. To fairly compare the various technologies, the sensitivity is normalized to the supply voltage V_{DD} . The comparison shows that the current-driven configuration provides the best performance because it has the advantage of combining low-voltage operation with high ion sensitivity. Moreover, when combined with an ion-selective membrane (ISM), the OEECT current-driven configuration achieved a sensitivity of 414 mV dec^{-1} , which is close to the value obtained in absence of the ISM. The ISM is implemented between the analyte and the inner electrolyte on the channel.^[9] Thus, the current-driven OEECT configuration can also operate with high sensitivity as an ion selective sensor. The reproducibility of the platform depends on the stability of the deposited PEDOT:PSS polymer and on the amount of fixed charges into the polyelectrolyte (PSS) phase.^[10] The stability of the polymer on glass is maximized by using GOPS in the PEDOT:PSS formulation.^[10] The amount of fixed charges into the polyelectrolyte (N_{fix}) depends on the polymer formulation and in the case of PEDOT:PSS results in $N_{fix} = 10^{21} \text{ cm}^{-3}$, viz. 1.66 M. As a result, when the ion concentration is smaller than about 1 M, the OEECT threshold voltage increases (viz. becomes more negative), the shift amounts to 112 mV per decade of ion concentration decrease (dec). We verified that this result is very reproducible, which has a variability of only about 1 mV/dec. The results in **Fig. 2.1 d** do not include error bars. However,

during the last years we mainly focused on the current-driven architecture for monitoring cell layers.^[7] Furthermore, we further developed high-sensitivity ion-detection and monitoring with the complementary OECT amplifier architecture.^[3] Overall, the various experiments provided an excellent reproducibility and stability of these architectures for both ion sensing and cell monitoring.

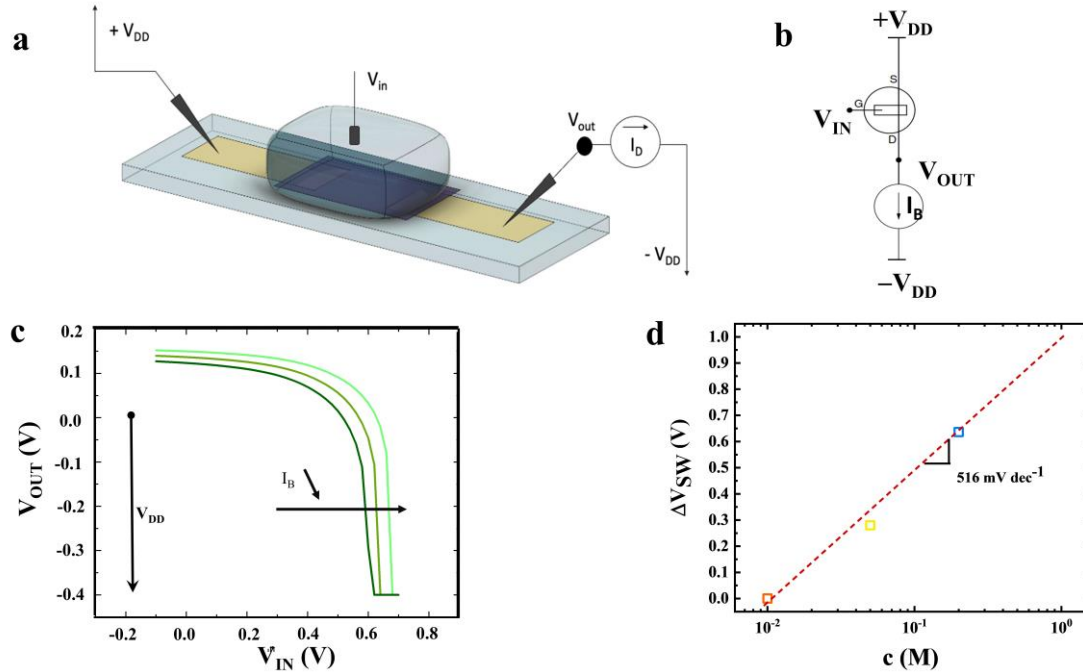


Figure 2.1: Current-driven OECT used as ion sensor. **a)** Device architecture of a current-driven OECT configuration. **b)** Schematic circuit of the OECT in current-driven configuration. **c)** Measured transfer characteristics of a current-driven OECT for various $I_B = [1.25; 1.00; 0.75]$ and $|V_{DD}| = 0.4$ V. The gate is an Ag/AgCl pellet and the OECTs geometries are: $W = 1000 \mu\text{m}$, $L = 2000 \mu\text{m}$, $t = 300$ nm. As electrolyte NaCl (aq) was used in a concentration of 0.1 M. **d)** Cumulative switching voltage variation $\Delta V_{SWi+1} = \Delta V_{SWi} + (V_{SWi+1} - V_{SWi})$ as a function of ion concentration. The average sensitivity calculated by last-square linear approximation is of 516 mV dec^{-1} . The gate electrode is a tungsten foil and the OECTs geometries are: $W = 1000 \mu\text{m}$, $L = 300 \mu\text{m}$, $t = 25$ nm. All images reproduced with permission.^[2] Copyright 2018, Springer Nature.

2.2 Complementary OECT Amplifier Based on the Current-Driven OECT Architecture

Recently, Romele *et. al.* has extended the current-driven architecture by substituting the current generator with a n-type OECT.^[3] This new architecture, named complementary OECT amplifier, is the very same topology of a complementary inverter but it is operated in analogue fashion, exploiting the circuit amplification. The schematic circuit diagram is displayed in **Fig. 2.2 a**. The input voltage V_{IN} is applied at the gates of the transistors and V_{OUT} is collected at their drains. In this configuration V_{DD} is applied at the source of the p-type OECT whereas the source of the n-type OECT is grounded. There are two modes of operation of the OECT amplifier. The Wide-Range (WR) mode is analogous to the current-driven operation. V_{IN} is

swept from GND (0V) to V_{DD} and V_{OUT} is recorded. The transition voltage, defined as the V_{IN} such that $V_{OUT} = V_{DD}/2$ is analogous to the V_{SW} in the current-driven configuration and depends on the ion concentration in the electrolyte. When operated in WR mode, the OECT amplifier takes advantage of a relatively low ion sensitivity to span the physiological range of ion concentration with a supply voltage as low as 0.5 V. Therefore, the WR mode enables to quantify the initial analyte concentration spanning several orders of magnitudes. Then, in order to detect small variations from the background concentration, a high sensitivity (HS) is required.

The HS mode of operation is schematically illustrated in **Fig. 2.2 b**. After using the OECT ion-sensitive amplifier in WR mode, the extracted $V_{OUT'}$ yields the initial background ion concentration. To operate in the HS mode, the input voltage is then set to V_{IN} such that $V_{OUT} = V_{OUT'}$. In this working region the output voltage is extremely sensitive to a shift in the transfer characteristic (viz. dV_{OUT}/dV_{IN} is large), and a small variation of ion concentration results in a large variation of V_{OUT} from $V_{OUT'}$ to $V_{OUT''}$ (from light blue to dark-blue, **Fig. 2.2 b**). The sensitivity of the OECT complementary amplifier is tuneable by the design parameters, transconductance and channel length modulation of the p- and n-type transistors during fabrication,^[11] but also by V_{DD} , which enables fine-tuning. With an increase in V_{DD} from 0.4 V to 0.5 V, the sensitivity almost doubled from 480 mV dec⁻¹ to 910 mV dec⁻¹.

By integrating an ISM, such as a K⁺-selective membrane, the OECT complementary amplifier operates as an ion selective sensor without losing sensitivity, as shown for K⁺ concentrations in a range of 10⁻⁴ M - 1 M (**Fig. 2.2 c**). The circuit-oriented device-aware sensor design approach enables the OECT complementary amplifier to operate with a top performing wide range and unprecedented sensitivity larger than 2300 mV V⁻¹ dec⁻¹, combined with real-time operation, tuneable performances and low operating supply voltage. It provides both ion detection over an ion concentration range of five orders of magnitude and real-time monitoring of variations two orders of magnitude lower than the detected concentration. The high sensitivity, multiscale and reconfigurable operation provided by the OECT complementary amplifier can be extremely relevant also in the emerging research field of bioelectronic sensors to improve the signal-to-noise ratio, resolution, and robustness.^[12]

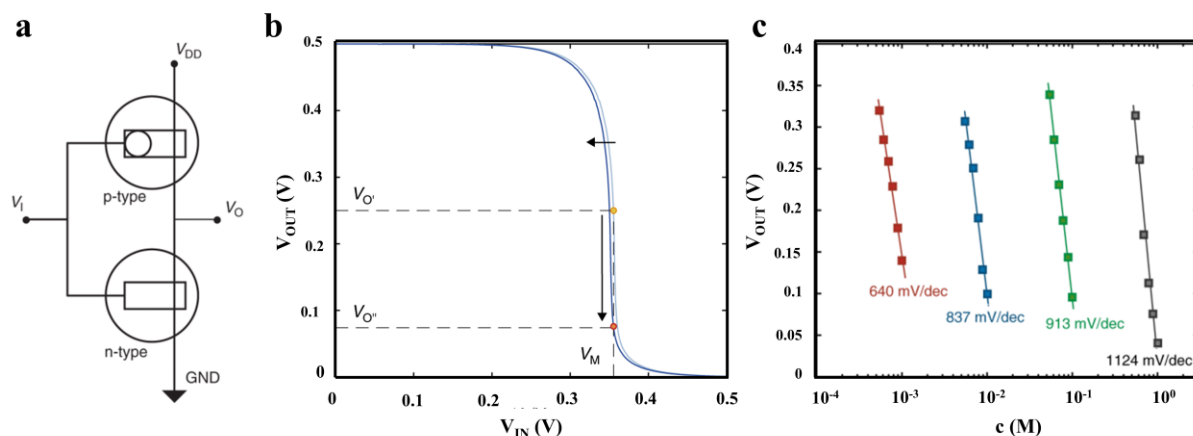


Figure 2.2: The OECT complementary amplifier. **a)** Schematic circuit of the OECT complementary amplifier. The V_{IN} is connected to the gates of the transistors, and V_{OUT} is collected at their drains. V_{DD} is connected to the source of the p-type OECT, and the source of the n-type is grounded (GND, $V_{GND} = 0$ V). **b)** Transfer characteristic of an OECT complementary amplifier. The red dot identifies V_M (viz. the required V_{IN} to have $V_{OUT} = V_{DD}/2$). To operate the OECT complementary amplifier with high sensitivity, the input voltage is biased at $V_{IN} = V_M$, while the output voltage is continuously measured. Light-blue characteristic: at $V_{IN} = V_M$ the output $V_{OUT} = V_{OUT}'$ and the ion concentration is c_0 . A small variation of the ion concentration results in a shift of the electrical characteristic (from light blue to dark blue) and this, in turn, in a large variation of the output voltage from V_{OUT} to V_{OUT}' . **c)** Real time high-sensitivity ion detection: Measured V_{OUT} as a function of c in various sub-range of concentrations, covering the whole physiological range. The ion concentration where $V_{OUT} = V_{DD}/2$ is $c_0 = [7.8 \times 10^{-4}, 7.8 \times 10^{-3}, 7.8 \times 10^{-2}, 7.8 \times 10^{-1}]$ M. Full lines are the linear least square fit to the measurements, yielding SA. The electrolyte concentration is increased every 30 s. The measurements are performed at $V_M = 0.415$ V. All images reproduced with permission.^[3] Copyright 2020, Springer Nature.

2.3 Sensing Barrier Tissue Integrity and Irreversible Barrier Tissue Disruption with the Current- Driven OECT

When monitoring small changes in the TER of barrier tissue, after adding a toxin in low concentration, a highly ion-sensitive impedance sensor is required. Due to the high ion sensitivity and low operating voltage, the OECT in current-driven configuration is a promising approach to sense barrier tissue integrity. A proven advantage of the current-driven OECT configuration is the possibility of tuning the operating range and voltages by means of the bias current I_B . This is very important when applied in bioelectronics, because the operation in an appropriate voltage window can limit possible side redox reactions that can be harmful for biology. Here, the ion-sensitivity of OECTs, using similar channel geometries, in current-driven configuration is compared to the standard configuration used by Jimison et al. in 2012, studying the effect of toxins, such as H_2O_2 , on the barrier function of Caco-2 cells.^[1] Barrier tissue disruption 60 min after adding 5 mM H_2O_2 has been monitored using the OECT in current-driven configuration (**Fig. 2.3 a**) and in standard configuration (**Fig. 2.3 b**).^[4] However, when comparing the response over time the enhanced ion-sensitivity of current-driven OECTs is evident. Extracting the response of the OECT is more evident in the current-driven

configuration, where it is directly revealed in the graph as the shift of V_{IN} , whereas in standard configuration an exponential fit of I_D must be performed. Hence, operating the OEECT in current-driven configuration monitors barrier disruption over time with higher sensitivity. The experiment has been repeated for a smaller concentration of 1 mM H_2O_2 . The minor disruption of barrier function could only be monitored with the current-driven configuration (**Fig. 2.3 c**), but not with the reference method (**Fig. 2.3 d**). The enhanced sensitivity of the OEECT, when operating in current-driven configuration, confirms the validity of using the OEECT as biosensor in current-driven configuration.

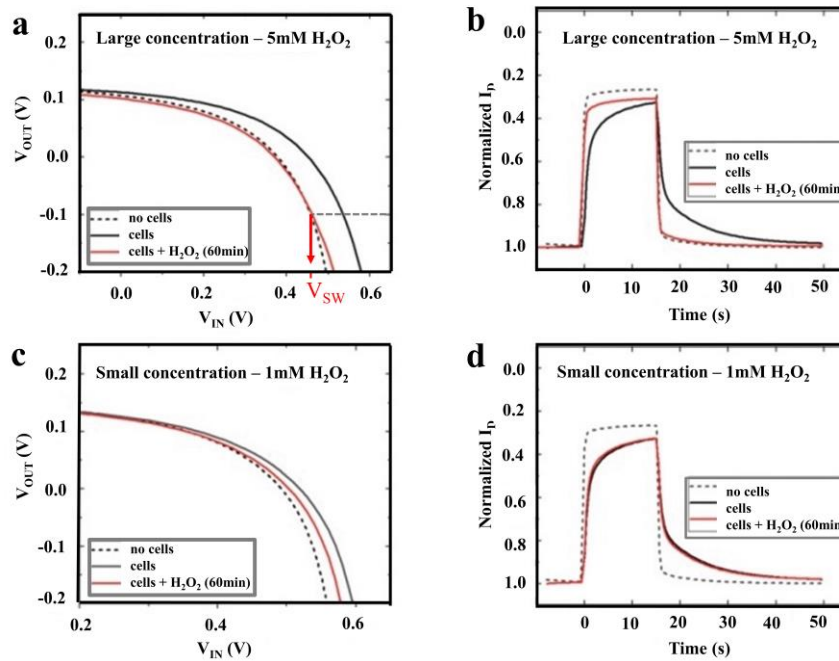


Figure 2.3: Sensing cell barrier integrity for H_2O_2 with an OEECT in current-driven configuration. The OEECT response in the absence and presence of barrier tissue adding 5 mM H_2O_2 **a)** and **b)** and 1 mM H_2O_2 **c)** and **d)** in the current-driven, **a)** and **c)**, and in the standard configuration, **b)** and **d)**. The transfer characteristics were taken at $V_{DD} = 0.2$ V and $I_B = -1.1$ mA **a)** and -0.6 mA **c)** in the current-driven configuration. In the standard configuration $V_D = -0.1$ V was used. Device dimension were $W = 2$ mm, $L = 1$ mm, $t = 100$ nm. An Ag/AgCl gate electrode and EMEM cell culture medium as an electrolyte was used. All images reproduced with permission.^[4] Copyright 2019, Wiley-VCH.

2.4 Motivation and Outline

In the previous chapters an introduction to this dissertation is given. **Chapter 1** describes the concept of organic bioelectronics with a focus on the OECT. The promising potential of OECTs as impedance sensors for *in vitro* monitoring of barrier tissues is discussed, which is crucial for toxicological characterisation of chemical compounds and drug delivery applications. Furthermore, the recent achievements in measuring tight junction modulation, impeding the transcellular pathway in barrier tissue of nutrients and drugs, are described. When the drain voltage is driven by an applied current while the gate voltage is swept, the OECT is operated as an inverter in a so called current-driven configuration. In **Chapter 2** the principle, advantages and recently achieved results of using the current-driven OECT are described in detail. The major objective of this dissertation is to study the applicability of OECTs in monitoring barrier tissue modulation regarding its ion-sensitivity. The work presented in this thesis demonstrates highly ion-sensitive technique to *in-situ* monitor TJ modulation of barrier tissue with the OECT. The work in this thesis aims to address some of the major concerns of the OECT as impedance sensor: monitoring *in-situ* over long intervals and enhancing the ion-sensitivity.

Chapter 3 outlines the experimental work accomplished in this thesis. Different PEDOT:PSS formulations and OECT device fabrication processes are reported. Cell culturing and the preparation of barrier tissue for incorporating into devices are further described in detail. In order to characterize the barrier functionality of tissues, electrical measurement configurations using the OECT with barrier tissue integrity as well as alternative electrical and optical measurement configurations are outlined.

The current-driven OECT offers a record ion-sensitivity at low operating voltage, exceeding the Nernst limit by one order of magnitude. In **chapter 4** the use of the current-driven OECT with integrated barrier tissue to *in-situ* sense the reversible loss of barrier function has been reported. As a model for reversible TJ modulation the effect of adding PLL as TJ modulator on a confluent barrier tissue of epithelial Caco-2 cell layer has been investigated. Investigating the effect of TJ modulators, causing temporal TJ opening, is of great importance for targeting drug development. A controlled TJ modulation is crucial to avoid cell damage, when drugs pass from organs into our blood.^[13] Sensing TJ modulation with bioelectronics such as the OECT as an alternative to established invasive methods gives a better understanding for studying drug delivery. In this chapter the current-driven OECT is presented as a suitable biosensor for the impedance modulation of barrier tissue, using Caco-2 barrier tissues under the effect of PLL as a case study.^[7] Due to its high sensitivity, the current-driven OECT enabled

the *in-situ* monitoring of reversible TJ modulations as a variation of output voltage. Due to the low operating voltage, the current-driven OECT successfully operates in real time over an extended time scale of 24 h which is necessary to monitor the process. By monitoring the effect for three different PLL concentrations, the current-driven OECT monitors TJ modulation with high sensitivity: monitoring no effect for 81 μM PLL (small concentration), reversible TJ modulation for 162 μM PLL (medium concentration), and irreversible TJ modulation for 324 μM PLL (high concentration). In addition, immunofluorescence images are presented, focusing on the displacement of occludin, as a relevant TJ protein. Our results show the progress of OECT technology towards *in vitro* testing of TJs for clinical applications, such as drug targeting and screening.

In **chapter 5** we address the challenge to monitor cellular barrier functionality with an enhanced sensitivity and translate it in real-time into the resistance of the barrier tissue using the dynamic-mode current-driven OECT. For this method the input voltage is swept dynamically forward and backward in a low voltage range, while measuring the output voltage. Obtaining the hysteretic behaviour of the output voltage, enhances the sensitivity compared to the standard current-driven OECT configuration. In this chapter we also show how the output sensitivity can be enhanced by an increase in the scan rate of the input signal. Selecting the scan rate during real-time measurements accordingly ensures the maximum performance in a wide range of resistances. Using the dynamic-mode current-driven OECT with barrier tissue integrity a sensitivity equal to 203 mV dec^{-1} was achieved within an operating range of $\text{TER}=13\text{-}640 \Omega \text{ cm}^2$. Measuring in the highly sensitive dynamic-mode current-driven OECT this highly sensitive method that allows us to successfully monitor reversible TJs modulation even for a very low TJ-modulator concentration of PLL ($c = 122 \mu\text{M}$) *in-situ*. Our results show that in dynamic-mode current-driven configuration the OECT is a suitable technology to monitor at the ultra-low detection limit of TJ modulator concentration. This offers opportunities for precision *in-vitro* medical diagnostic. In addition, numerical circuit simulations of all experimental results provide a clear rationale of the proposed approach and highlight the key design parameters.

2.5 References

- [1] L. H. Jimison, S. A. Tria, D. Khodagholy, Gurfinkel M., E. Lanzarini, A. Hama, G. G. Malliaras, R. M. Owens, *Adv. Mater.* **2012**, *24*, 5919.
- [2] M. Ghittorelli, L. Lingstedt, P. Romele, N. I. Crăciun, Z.M. Kovács-Vajna, P.W.M. Blom, F. Torricelli, *Nature Communications* **2018**, 1441.
- [3] P. Romele, P. Gkoupidenis, D. A. Koutsouras, K. Lieberth, Z. M. Kovács-Vajna, P. W. Blom, F. Torricelli, *Nat. Commun.* **2020**, *11*, 1.
- [4] L. V. Lingstedt, M. Ghittorelli, M. Brückner, J. Reinholz, N. I. Crăciun, F. Torricelli, V. Mailänder, P. Gkoupidenis, P. W. M. Blom, *Adv. Healthcare Mater.* **2019**, *8*, e1900128.
- [5] M. Braendlein, T. Lonjaret, P. Leleux, J.-M. Badier, G. G. Malliaras, *Adv. Sci.* **2017**, *4*, 1600247.
- [6] D. A. Bernardis, G. G. Malliaras, *Adv. Funct. Mater.* **2007**, *17*, 3538.
- [7] K. Lieberth, M. Brückner, F. Torricelli, V. Mailänder, P. Gkoupidenis, P. W. M. Blom, *Adv. Mater. Technol.* **2021**, *6*, 2000940.
- [8] F. Torricelli, L. Colalongo, D. Raiteri, Z. M. Kovács-Vajna, E. Cantatore, *Nat. Commun.* **2016**, *7*, 1.
- [9] a) M. Sessolo, J. Rivnay, E. Bandiello, G. G. Malliaras, H. J. Bolink, *Adv. Mater. Interfaces* **2014**, 4803; b) K. Schmoltner, J. Kofler, A. Klug, E. J. W. List-Kratochvil, *Adv. Mater.* **2013**, 6895.
- [10] P. Romele, M. Ghittorelli, Z. M. Kovács-Vajna, F. Torricelli, *Nat. Commun.* **2019**, *10*, 3044.
- [11] D. A. Bernardis, G. G. Malliaras, *Adv. Funct. Mater.* **2007**, *17*, 3538.
- [12] a) E. Macchia, R. A. Picca, K. Kyriaki Manoli, C. Cinzia Di Franco, D. Davide Blasi, L. Lucia Sarcina, N. Nicoletta Ditaranto, N. Cioffi, R. Österbacka, G. Scamarcio et al., *Materials Horizons* **2020**, *7*, 999; b) R. A. Picca, K. Manoli, E. Macchia, L. Sarcina, C. Di Franco, N. Cioffi, D. Blasi, R. Österbacka, F. Torricelli, G. Scamarcio et al., *Adv. Funct. Mater.* **2020**, *30*, 1904513.
- [13] J. M. Anderson, B. R. Stevenson, D. A. Goodenough, M. S. Mooseker, *J. Cell Biol.* **1986**, *103*, A71.

3 Experiment and Methods

In this chapter the fabrication of OECTs, biological preparation as well as characterisation methods used in this work are presented. The fabrication process of OECT devices with a focus on two different PEDOT:PSS formulations is described. The preparation of biological samples contains culturing of cancerous Caco-2 cells from the intestine as a model for barrier tissue and preparation for biological experiments. Relevant electrical and microscopical characterisation techniques investigating barrier tissue by itself or integrated in an OECT are described and complete the experimental section.

3.1 PEDOT:PSS Formulations

In this work two PEDOT:PSS formulations were used, differing by the addition of a cross-linker. In the following chapters the used formulation will be specified. The PEDOT:PSS formulation without cross-linker consisted of an aqueous dispersion of the conducting p-type polymer PEDOT:PSS (Clevios PH1000, 90 vol.%), one droplet of the surfactant Zonyl (Du Pont FSO-100) and the conductivity enhancer dimethyl sulfoxide (DMSO, 10 vol.%). The dispersion of PEDOT:PSS was spin coated at 1500 rpm on the device defining the layer thickness of ≈ 100 nm. The thickness of the spin-coated films was measured with a surface profilometer (Bruker, DektakXT Stylus Profiler) at dry conditions.^[1]

For the formulation with cross-linker PEDOT:PSS is mixed with 5 vol.% ethylene glycol (EG), 0.1 vol% dodecyl benzene sulfonic acid (DBSA) and 1 vol% of the cross-linker (3-glycidyloxypropyl)trimethoxysilane (GOPS). The film was spin coated in two steps at 1500 rpm and 650 rpm for 1 min, respectively and annealed at 120 °C for 1 min in between.^[2]

3.2 Fabrication of OECTs

In this section the fabrication of OECTs with PEDOT:PSS as the OMIEC polymer in the channel is described. OECTs are processed by thermal evaporation of metal contacts using shadow masks for patterned structures. All cleaning and fabrication processes were conducted in a clean room and in a glovebox under inert conditions.

Glass substrates (Corning® EAGLEXGTM AMLCD) of 30 x 30 mm were used. The substrates were cleaned first by sonication in water with soap (Micro-90®) for 15 min and then in a 1:1 (vol/vol) solvent mixture of acetone and isopropanol for 15 min. The substrates were subsequently dried and further cleaned with a UV-ozone treatment (UVOCS ®) for 20 min to remove any organic residues on the surface. An array of source and drain gold contacts was thermally evaporated with a thickness of 100 nm using a shadow mask. An adhesion layer of chromium (5 nm) was previously deposited. The active area is defined between source and drain electrodes with a geometry of $W \times L = 2 \times 1$ mm (**Fig. 3.1**). For a better adhesion, the glass surface was reactivated by a UV-ozone treatment for 20 min before film deposition. The PEDOT:PSS channel was patterned with a wet cotton stick before annealing for 1 h at 140 °C. After annealing the devices were rinsed with DI water for swelling of the active area. A polymethyl methacrylate (PMMA)-well was placed on top defining the volume of the electrolyte using double-sided tape to prevent leakage.^[1,3]

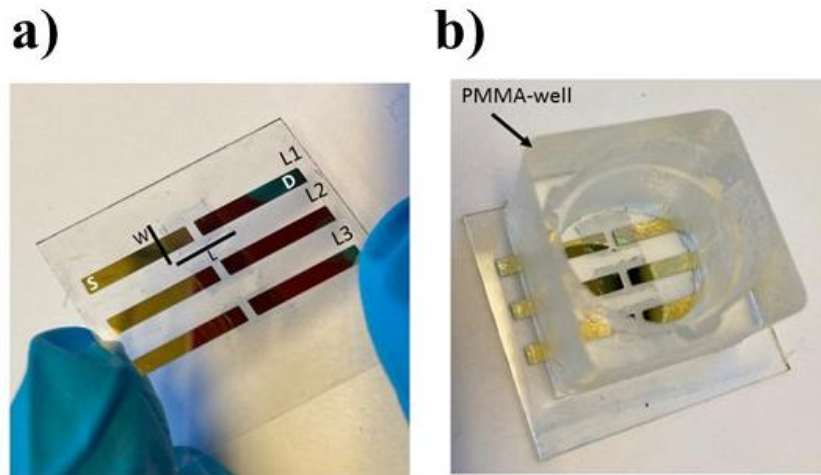


Figure 3.1: Device with and without PMMA-well. **a)** Glass slide with three source (S) and drain (D) electrodes connected by PEDOT:PSS channels with the geometries width (W) x length (L). **b)** Self-standing device setup with a PMMA-well glued on the glass slide in order to implement a Transwell filter.

3.3 Cell Preparation

This section contains the culturing of Caco-2 cells, the Transwell-filter preparation, the preparation of TJ modulators, and immunofluorescence staining. The Caco-2-cell line was used as a model to investigate barrier tissue integrity and barrier tissue modulation.

3.3.1. Culturing of Caco-2 Cells

Cells were cultured in EMEM (Eagle's Minimum Essential Medium, Invitrogen) with 10 % FBS (fetal bovine serum, Invitrogen), 2×10^{-3} M glutamine (GlutaMax-1, 100X, Invitrogen) and Pen-strep ($10\,000 \mu\text{g mL}^{-1}$ penicillin, $10\,000 \mu\text{g mL}^{-1}$ streptomycin, Invitrogen) with a medium change every 2 or 3 days.^[4] Cells were maintained at 37°C in a humidified atmosphere with 5 % CO_2 (CO_2 incubator C200 Labotect) during cell culturing and the experiment. When a confluency of around 80 % is reached, cells were passaged by discarding consumed cell medium and washing in 10 mL Dulbecco's Phosphate Buffered Saline (PBS, Sigma-Aldrich). For detachment the cells were immersed in 10 mL trypsin/ EDTA (Thermo Fisher, Gibco) for 15 min at 37°C . By the addition of 10 mL EMEM the reaction is stopped. The cell suspension was centrifuged at 800 rpm for 3 min. After removing the supernatant medium, the formed cell pellet was resuspended in 10 mL cell medium. For cell viability, the cell solution was mixed with a Trypan Blue solution (0.4 %, Sigma-Aldrich) in a volume ratio of 1:1 (20 μL). The live count was determined by an automated Cell Counter (TC10, Bio-Rad).

To measure barrier tissue integrity and barrier tissue modulation, Caco-2 cells (DSMZ, ACC 169) were seeded at 1.5×10^5 cells per Transwell filter with reduced area (0.16 cm^2 , pore

size = 0.4 μm). The medium was changed every 2-3 days. Experiments were performed on day 14 after seeding, corresponding to a TER $\approx 400 \Omega \text{ cm}^2$.^[3,5] The TER-value was measured with a handheld Volt-Ohm meter EVOM2 from World Precision Instruments.

Caco-2 cells were purchased from the Leibniz-Institute DSMZ – Deutsche Sammlung von Mikroorganismen und Zellkulturen GmbH.

3.3.2. Transwell-filter Preparation

For an increased barrier tissue resistance, the area of the permeable filter was reduced from 1.12 cm^2 to 0.16 cm^2 by coating polydimethylsiloxane (PDMS) on the back side of the filter and cured at room temperature for 2 days, as displayed in **Fig 3.2**. The silicon elastomer from Dow Corning was processed by adding 10 vol% Sylgard 184. The mixture was centrifuged at 2000 rpm for 2 min and further stored at -20 °C. The PDMS-modified Transwell filters were coated with collagen as stated in the literature for enhanced cell attachment.^[4] The PDMS-modified Transwell filters were sterilized under UV-light for 60 min and washed twice with PBS before incubating the filters with 0.5 ml collagen (type 1 solution from rat tail, Sigma Aldrich) over night at 37 °C. The remaining solution was removed and the filters were dried under UV light. The filters were washed with PBS before cell seeding.^[3]

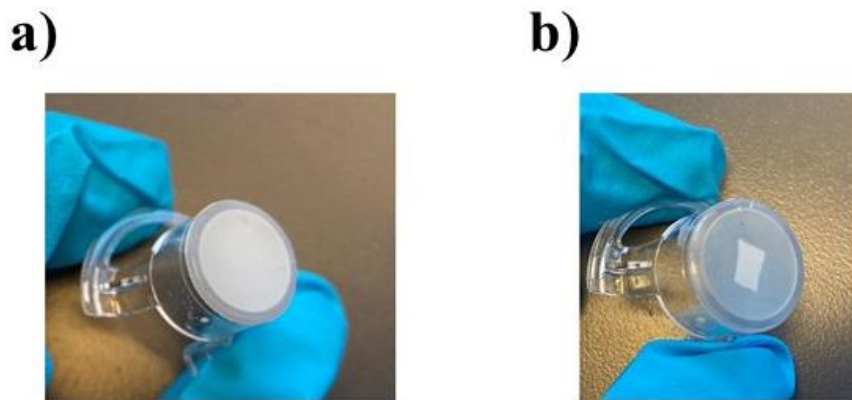


Figure 3.2: Filter Preparation. **a)** Original Transwell filter ($A = 1.12 \text{ cm}^2$). **b)** Transwell filter with PDMS coated on the bottom side of the filter ($A \approx 0.16 \text{ cm}^2$).

3.4 Characterization Methods

In this section, electrical and optical characterisation methods will be outlined. Electrical measurements of OECTs with barrier tissue integrity were performed at 37 °C in a humidified atmosphere with 5 % CO_2 in an incubator. In addition, electrochemical impedance spectroscopy was conducted on OECTs in the presence and absence of barrier tissue under ambient atmosphere using a probe station. As an alternative electrical method the TER

measurement technique is presented. To support outcomes from electrical measurements, additional optical methods were performed using microscopy.

3.4.1 Electrical characterisation using the OECT

All electrical measurements were performed at 37 °C in a humidified atmosphere with 5 % CO₂ by using a Keithley 4200-Semiconductor Characterization System and were analysed by using OriginLab software. Cell culture medium (EMEM) was utilized as an electrolyte apical and basal. An Ag/AgCl electrode (pellet, 2 mm, Warner Instruments) operated as a gate, immersed in the Transwell filter (**Fig. 3.3**). The operating gate voltage was kept well below 1.0 V to avoid water electrolysis and any cell damage.^[6]

When sensing the barrier function of tissues incorporated in the OECT over 24 h, the experiment was performed in a continuous measurement to minimize initialization parameter variations. Before integrating a Transwell filter with cells seeded on top, a prototype Transwell filter in absence of cells was employed to measure device stability over one hour. Ensuring cell layer stability, the prototype Transwell filter was exchanged with a Transwell filter with barrier tissue and the OECT with integrated barrier tissue was then measured for further 3 h (**Fig. 3.3**). Before adding PLL solution in DI water (0,56 mM, $M_w = 30-70$ kDa, Sigma Aldrich) apical to the barrier tissue, the same volume of electrolyte was removed in order to keep the ionic concentration similar. Cell layers were exposed to the following three concentrations of PLL: 72 μ L (81 μ M) 120 μ L (162 μ M), 240 μ L (324 μ M). After 90 min of treatment, the electrolyte was exchanged apical and basal and the measurement was continued for further 20 h.^[6]

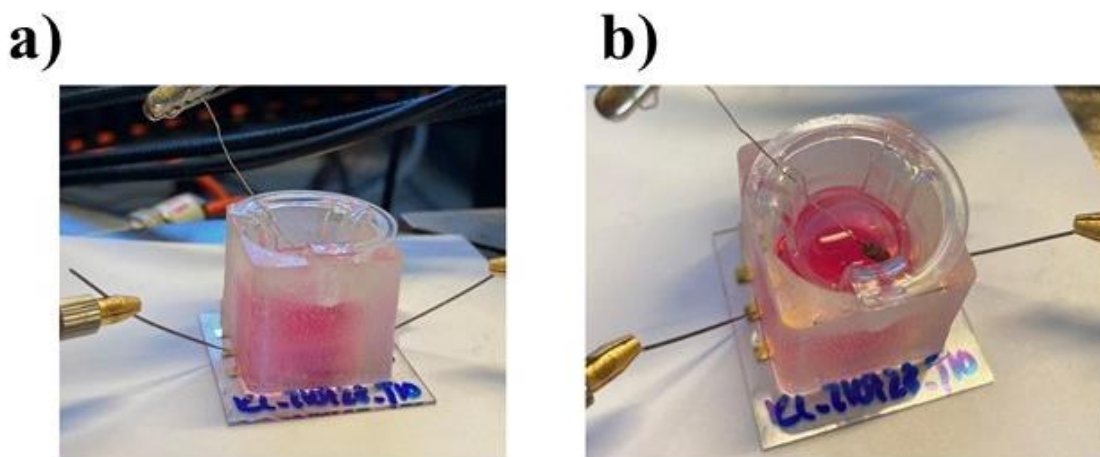


Figure 3.3: Device operation of an OECT with an integrated barrier tissue. Cells, seeded on a Transwell-filter, are placed between the gate and the channel. Cell medium is used as electrolyte. a) Upside view. b) Front view.

In order to monitor barrier tissue with high sensitivity, the OECT was operated in various configurations. The measurement settings are revealed in the following sections. To

comparing dynamic current-driven, current-driven, and transient response measurements, all three methods were performed in parallel on the same biological sample. In order to avoid cell stress, a waiting time of 3 *min* was imposed between sequences.^[7]

Standard Transient Response Measurements

For transient response measurements, we measured the drain current, while biasing the channel with a constant drain voltage $V_D = -0.4$ V and pulsing a square wave potential on the gate electrode from $V_{G_OFF} = 0$ V to $V_{G_ON} = 0.5$ V with $t_{ON} = 15$ s and $t_{OFF} = 30$ s. The transient response time was extracted by an exponential fit of $I_D(t)$.^[8]

Standard Current-Driven Configuration

In standard current-driven configuration, the OECT was measured with a supply voltage V_{DD} varying from 0.2 to 0.4 V. The input voltage V_{IN} applied at the gate was swept in a range of [-0.2; 0.8] V, while not exceeding 0.8 V voltage difference. The current bias I_B was chosen individually and is specifically mentioned for each measurement. For the standard current-driven measurement the input voltage was swept forward (from negative to positive V_{IN} voltages) only with a scan speed = 0.125 V s⁻¹.^[9]

Dynamic Current-Driven Configuration

For the dynamic current-driven configuration a dual sweep of the input voltage $V_{IN} = [0; 0.8$ and $0.8; 0]$ V was performed at the gate. To achieve the highest ion sensitivity a scan speed of 0.002 Vs⁻¹ was chosen. To perform scan speed dependent measurements, the scan speed was varied between 0.002 Vs⁻¹ and 0.5 Vs⁻¹. The supply voltage was kept same for both techniques at $V_{DD} = 0.2$ V. The current bias I_B was chosen individually.^[10]

Electrochemical impedance spectroscopy

Electrochemical impedance spectroscopy (EIS) was realized in a three-electrode configuration with a potentiostat (PalmSens4) and analysed with the software PalmSens5. OECT's source and drain, connected over the PEDOT:PSS channel, were shorted serving as the working electrode, while Pt and Ag/AgCl electrodes were used as the counter and the reference electrode, respectively. To investigate the frequency depended impedance properties of barrier tissue integrated in an OECT, counter and reference electrodes were placed apical in the Transwell filter, whereas the working electrode was basal. At the working electrode a small voltage signal was applied, and the impedance was recorded as a function of frequency with $f = [0.1; 10^6]$ Hz. The data were fitted with an equivalent (RC)-circuit in absence of barrier tissue and an (R(RC)C)-circuit in presence of barrier tissue.^[11]

3.4.2 Transepithelial electrical resistance measurement as an alternative electrical characterisation method

To determine the resistance of barrier tissues a TER measurement were performed with a handheld epithelial volt-ohm meter EVOM2™ (World Precision Instruments), as presented in **Fig. 3.4**. Two concentric electrodes, incorporating a voltage-sensing Ag/AgCl pellet in the centre and an annular current electrode on the outer, create an electric field within the electrolyte in between. The current electrode is made of Ag and coated with AgCl. The distance between both electrodes can be tuned at the cap, so that the top electrode is 1-2 mm on top of the measured barrier tissue. The complete setup is schematically depicted in **Fig. 3.4 c**. The voltage is measured, while a small alternating current signal is applied between the electrodes, so that the electrical resistance is calculated for the given electrode area as a TER-value. In this thesis the TER-value is given in $\Omega \text{ cm}^2$, normalized to the active area of the Transwell insert.^[12]

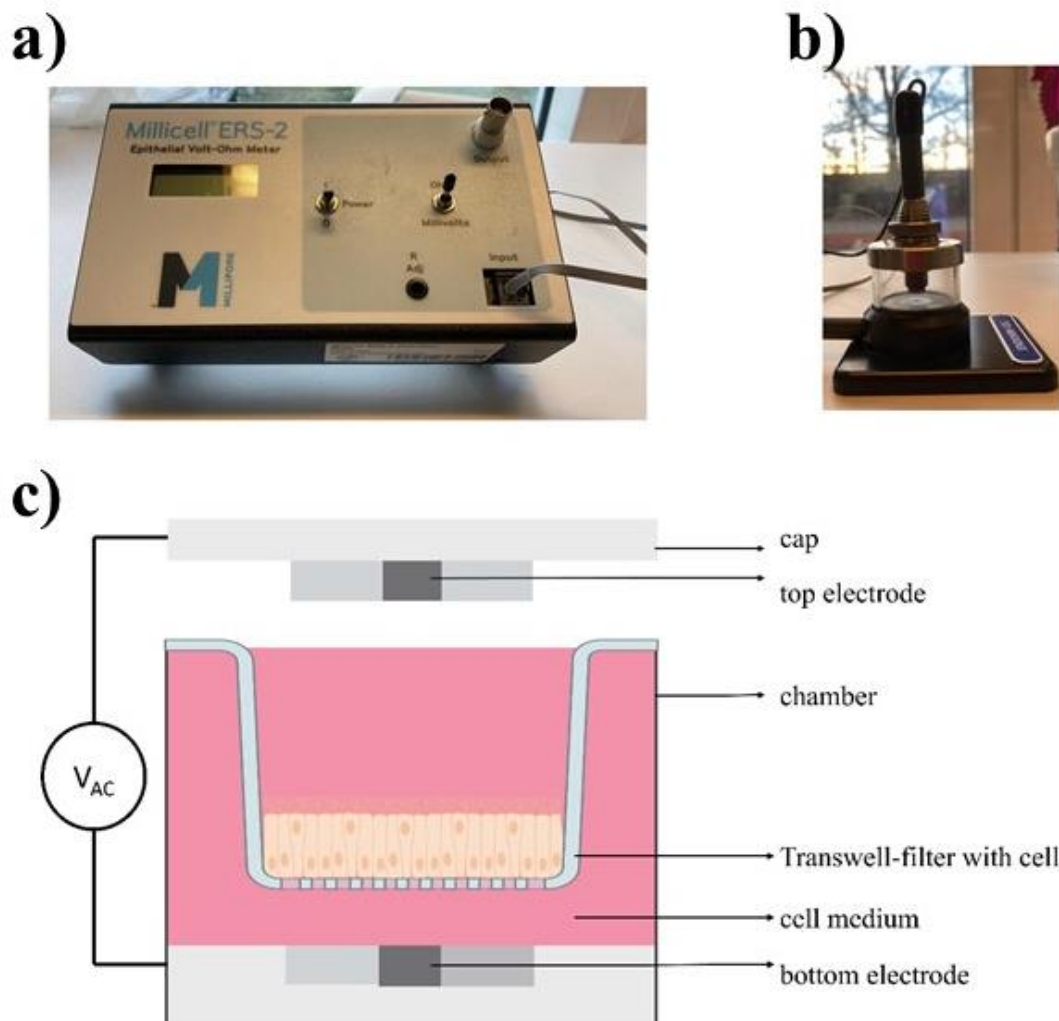


Figure 3.4: Device setup of a TER VOLT-OHM METER. a) Image of the epithelial volt-ohm meter Millicell ERS-2 comprising of the measuring device EVOM. b) The EndOhm chamber. c) Schematic diagram of the EndOhm chamber in the open state with an integrated Transwell filter.

3.4.3 Optical Characterisation

Cell Viability Assay

Caco-2 cells were seeded in a 96-well plate (Greiner Bio-One, Austria), instead of Transwell filters, with a cell number of 5×10^3 cells per well in $100 \mu\text{l}$.^[13] After four days of cultivation at 37°C and 5% CO_2 , the medium was removed. PLL (81.4, 162.86, 325.7, and $570 \mu\text{mol L}^{-1}$) were prepared in 10% FBS supplemented EMEM (except for $570 \mu\text{mol L}^{-1}$, which was used directly) and added in a volume of $100 \mu\text{L}$ to the cells. Samples were handled in biological triplicates. Caco-2 cells were incubated at 37°C and 5% CO_2 for 1, 2, and 4 h before conducting the viability assay. In case of the cell recovery, Caco-2 cells were incubated for 90 min with PLL followed by a recovery of 20 h in fresh EMEM medium (10% FBS) before conducting the viability assay. Milli-Q water and 20% DMSO in medium were used as positive controls. CellTiter-Glo[®] Luminescent Cell Viability Assay (Promega, Germany) was performed according to the manufacturer's instructions. The luminescence signal was measured with an Infinite M1000 plate reader (Tecan, Switzerland).^[7]

Immunofluorescence Staining

Confocal laser scanning microscopic images (cLSM) of immunofluorescently stained Caco-2 cells against the TJ protein occludin was performed to investigate the presence of TJs and TJ opening after 90 min of PLL exposure followed by 20 h of recovery in EMEM.

Immunofluorescence staining was conducted on the cytoskeleton and the nucleus of cells to visualize cell layer coverage. In this procedure, the cells were washed once with PBS and then fixed with 4% paraformaldehyde in PBS for 10 min at room temperature, followed by permeabilization with 0.2% Triton-X 100 and 1% BSA in PBS for 2 h. Milli-Q water (Merck) and 20% DMSO in cell culture medium were used as controls.

Staining was performed with an occludin monoclonal antibody (AF488, Thermo 33-1511) with a concentration of $5 \mu\text{g mL}^{-1}$ in 0.15 mL PBS for each μ -Slide 8 well and in 0.25 mL PBS for each Corning[®] FluoroBlok[™] Transwell filter for 24 h at 4°C in the fridge. After antibody incubation, the occludin dilution in PBS was removed and the cells were washed with PBS.

For the Transwell filters, the cell-containing membranes were excised carefully with a scalpel and placed with the cells facing upwards on a glass slide. Fluoromount-G[™] mounting medium was added to the top of the cells and a cover slip was used to seal the construct and examined under a confocal laser scanning microscope (cLSM). Z-stack images were taken on the LSM SP5 STED Leica Laser Scanning Confocal Microscope (Leica, Germany), composed

of an inverse fluorescence microscope DMI 6000CS equipped with a multilaser combination using a HCX IRAPO L 25.0 × 0.95 water objective. The specimen's FITC dye was excited with the excitation laser at 488 nm and detected with an emission filter at 510–550 nm. Editing of images was conducted by using the Fiji software and Microsoft Power Point. In Fiji, the z-stacks were converted to 2D by using the maximum intensity projection. The occludin channel was pseudo-coloured in green. In addition, the Fiji adjust function was used to automatically correct brightness and contrast. Finally, Fiji selected images were processed by Microsoft Power Point adjusting the brightness (+20 %) and contrast (+40 %).^[7]

3.5 References

- [1] L. V. Lingstedt, M. Ghittorelli, H. Lu, D. Koutsouras, T. Marszalek, F. Torricelli, N. I. Crăciun, P. Gkoupidenis, P. W. M. Blom, *Adv. Electron. Mater.* **2019**, 26, 1800804.
- [2] P. Gkoupidenis, D. A. Koutsouras, G. G. Malliaras, *Nature Comm.*, **2017**, 8, 15448.
- [3] L. V. Lingstedt, M. Ghittorelli, M. Brückner, J. Reinholz, N. I. Crăciun, F. Torricelli, V. Mailänder, P. Gkoupidenis, P. W. M. Blom, *Adv. Healthcare Mater.* **2019**, 8, e1900128.
- [4] G. Sitterley, *BioFiles* **2008**.
- [5] a) D. A. Volpe, *J. Pharm. Sci.* **2008**, 97, 712; b) J. Reinholz, C. Diesler, S. Schöttler, M. Kokkinopoulou, S. Ritz, K. Landfester, V. Mailänder, *Acta biomaterialia* **2018**, 71, 432; c) K. Sonaje, E. Y. Chuang, K. J. Lin, T. C. Yen, F. Y. Su, M. T. Tseng, H. W. Sung, *Molecular Pharm.*, **2012**, 9, 1271.
- [6] J. A. DeFranco, B. S. Schmidt, M. Lipson, G. G. Malliaras, *Org. Electron.*, **2006**, 7, 22.
- [7] K. Lieberth, M. Brückner, F. Torricelli, V. Mailänder, P. Gkoupidenis, P. W. M. Blom, *Adv. Mater. Technol.*, **2021**, 6, 2000940.
- [8] K. Lieberth, A. Pavlou, D. Harig, P. Gkoupidenis, P.W.M. Blom, F. Torricelli, **2022**, (under preparation)
- [9] L. H. Jimison, S. A. Tria, D. Khodagholy, M. Gurfinkel, E. Lanzarini, A. Hama, G. G. Malliaras, R. M. Owens, *Adv. Mater.* **2012**, 24, 5919.
- [10] M. Ghittorelli, L. Lingstedt, P. Romele, N. I. Crăciun, Z.M. Kovács-Vajna, P.W.M. Blom, F. Torricelli, *Nature Commun.* **2018**, 1441.
- [11] a) D. A. Koutsouras, P. Gkoupidenis, C. Stolz, V. Subramanian, G. G. Malliaras, D. C. Martin, *Chem. Electro. Chem.*, 4, 9, 2321-2327. b) D. A. Koutsouras, L. V. Lingstedt, K. Lieberth, J. Reinholz, V. Mailänder, P. W. M. Blom, P. Gkoupidenis, *Adv. Healthcare Mater.* 8, 23, 1901215.
- [12] B. Srinivasan, A. R. Kolli, M. B. Esch, H. E. Abaci, M. L. Shuler, J. J. Hickman, *J. of Lab. Autom.*, **2015**, 20, 107.
- [13] a) B. Christ, C. Fey, A. Cubukova, H. Walles, S. Dembski, M. Metzger, **2017**, 1601, 111; b) M. Fisichella, F. Berenguer, G. Steinmetz, M. Auffan, J. Rose, O. Prat, *BMC Genomics* **2014**, 700.

4 Monitoring reversible Tight Junction Modulation with the OECT

4.1 Summary

The barrier functionality of a cell layer regulates the passage of nutrients into the blood. Modulating the barrier functionality by external chemical agents like poly-L-lysine (PLL) is crucial for drug delivery. The ability of a cell layer to impede the passage of ions through it and therefore to act as a barrier, can be assessed electrically by measuring the resistance across the cell layer. In this chapter, we investigate the OECT in a current-driven configuration for *in-situ* monitoring of reversible tight junction modulation under the effect of drug additives, like poly-L-lysine. Exposure to low and medium concentrations of PLL initiates reversible modulation, whereas a high concentration reaches toxicity levels and induces an irreversible barrier disruption due to non-functional tight junction proteins. The results demonstrate the suitability of OECTs to *in-situ* monitor temporal barrier modulation and recovery. This shows its potential for *in vitro* and even *in vivo* toxicological and drug delivery studies.

4.2 Introduction

Since the early 90s, polycations such as chitosan or poly-L-lysine (PLL) are known to be potential promoters of drug delivery across intestinal barrier tissues.^[15,16] Polycations represent the most convenient manner to affect oral bioavailability having attributes such as enhancing drug solubility, protecting sensitive drugs from rapid degradation due to positive charges at a broad pH range, and serving as a permeability enhancer.^[17] PLL modulates the barrier functionality of epithelial cell layers by enhancing paracellular permeability as a TJ modulator.^[15,18,19] Monitoring the effect of PLL on the paracellular permeability through cell layers with barrier function has been first studied by McEwans *et al.* (1993), investigating the potential difference of physical barriers, such as MDCK canine kidney cells, with the Ussing-chamber. The work of Roblendo *et al.* (1999) investigated the effect of PLL on BEAS-2B human bronchial cells by measuring the radioactivity [¹⁴C] mannitol flux. As the most related work, Ranadi *et al.* (2002) investigated the increase of paracellular permeability of Caco-2 cells during a 2 h exposure to PLL concentration-dependent using TER measurements. However, there is no study to our knowledge on *in-situ* monitoring reversible TJ modulation with PLL as modulator. An opening of TJs causes a temporary loss of barrier functionality and allows the passage of ions or drugs across the barrier, respectively.^[4,8] Furthermore, it has been demonstrated that PLL induces reversible TJ modulation through morphological modifications of the F-actin cytoskeleton as well as a redistribution of zonulin and occludin.^[19] Therefore, recording temporal TJ modulation under the influence of a polycationic modulator is of great importance to assess the transient state of barrier functionality with potential applications in drug delivery.

More recently, the sensitivity of OECTs to ions has been strongly enhanced at low voltages using the OECT in a current-driven, inverter-like configuration.^[39] Because of this enhanced sensitivity, minute changes of ionic concentrations can be detected and therefore also small changes of a biological barrier can be detected. Furthermore, the enhanced sensitivity allows the acquisition of only one output characteristic at an effective frequency (determined by the voltage sweep rate) as compared to more traditional methods, where e.g. the transconductance is measured across a frequency range, which is more time-consuming. An investigation on irreversible barrier tissue disruption with hydrogen peroxide using a current-driven OECT confirmed the improved ion sensitivity compared to transient response measurements.^[40]

In this chapter, we demonstrate for the first time *in-situ* monitoring of barrier tissue modulation using the current-driven OECT by studying the epithelial barrier tissue integrity under the influence of PLL as TJ modulator with a current-driven OECT. The electrical response of the barrier tissue is measured as a function of TJ modulator concentration. The results demonstrate a reversible modulation of barrier functionality for low and medium concentration, whereas an irreversible effect is observed for high concentration. This study will pave the way to electrically monitor in real-time the reversible opening and closing of TJs, which is of great importance for drug delivery.

4.3 Results and discussion

4.3.1 Current-driven OECT with cell barrier integrity.

Measuring with the OECT in current-driven configuration, the voltage at the gate (input voltage, V_{IN}) was altered, whereas the output voltage, V_{OUT} was detected at the drain. As the current-driven OECT is highly ion sensitive, the measurements were performed at a specific frequency. In order to create an inverter-like circuit topology with the OECT, a direct current was applied at the drain, labelled as current bias I_B , controlling the threshold voltage. The supply voltage $\pm V_{DD}$ defines the saturation level of the ($V_{OUT} - V_{IN}$)-transfer characteristics, and was set by means of voltage compliance at the current-generator.^[41] The electronic circuit of a current-driven OECT is schematically portrayed in **Fig. 4.1 a**.^[39] A detailed description of the fabrication process is presented in the experimental section. The current-driven OECT functions as an ionic sensor, investigating the alteration of TJ properties of the Caco-2 cell layer under the influence of PLL. An effective barrier tissue with pristine TJs has a low paracellular ion permeability. Because PLL induces TJ-opening, the ion permeability increases temporarily. Due to the gate potential, ions then pass the barrier tissue, and permeate into the PEDOT:PSS channel. The OECT transduces the presence of ions into an electronic signal. All ($V_{OUT} - V_{IN}$)-measurements were performed at $I_B = [0.2; 0.5]$ mA and $V_{DD} = |0.4|$ V with 15 min delay time under physiological conditions. The ($V_{OUT} - V_{IN}$)-transfer characteristics of the current-driven OECT with an integrated cell layer monitoring ion permeability across a cell layer is displayed in **Fig. 4.1 b**. To analyse barrier tissue modulation, the shifting of ($V_{OUT} - V_{IN}$)-transfer characteristics were quantified by the switching voltage V_{SW} , indicated in **Fig. 4.1 b**. V_{SW} is the minimum V_{IN} required to operate the OECT in saturation. Effectively, this circuit topology represents an inverter circuit. For example, when V_{IN} is scanned from negative to positive voltages, there is a transition in V_{OUT} between $+V_{DD}$ and $-V_{DD}$. In this transition V_{SW} expresses the gate voltage at which there is the onset of the saturation regime of the transistor. V_{SW} is defined to be at $V_{OUT} = \frac{1}{2} (-V_{DD})$.^[39] Hence, the ($V_{OUT} - V_{IN}$)-transfer characteristic in presence of the integrated cell layer (black) results in a higher V_{SW} compared to a device in absence of barrier tissue (grey, dashed), as seen in **Fig. 4.1 b**. Being able to monitor minute changes in ionic concentration makes the current-driven OECT a beneficial and competing method to evaluate cell barrier integrity and its TJ modulation.

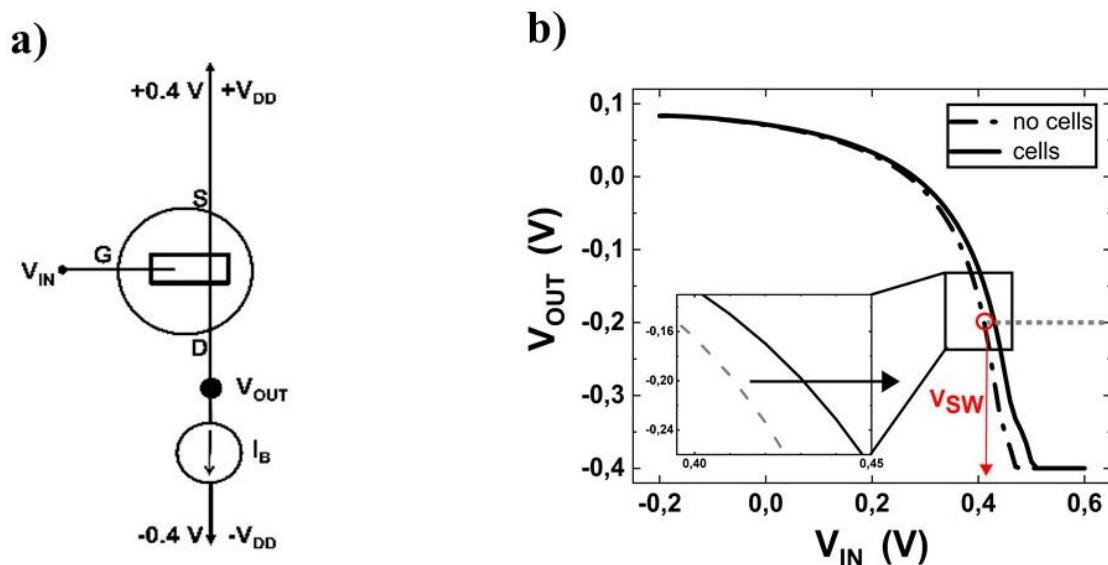


Figure 4.1: Current-driven OEET with cell barrier integrity. **a)** Schematic electronic circuit of a current-driven OEET.[39] **b)** Measured ($V_{OUT} - V_{IN}$)-transfer characteristics of a current-driven OEET in absence (dashed line) and presence (solid line) of barrier tissue. V_{SW} (red circle) is defined as a specific V_{IN} (red arrow) at which V_{OUT} is equal to half $|V_{DD}|$, marked as a horizontal grey dashed line to guide the eye.

4.3.2 Sensing reversible tight junction modulation over time with a current-driven OEET

Schematically, the four experimental steps to sense reversible TJ modulation with a current-driven OEET are represented in **Fig. 4.2 (a)**. Once V_{IN} was applied to the device with an integrated plain Transwell filter, cations from the apical and basal side were injected into the channel without facing any cell barrier at the Transwell filter, presented in sketch (1). Since, at a given V_{IN} many ions can penetrate the PEDOT:PSS channel, rapid dedoping leads to a decrease of V_{OUT} until saturation was reached (**Fig. 4.1 b** dashed line). When an intact cell layer is introduced, the transport of ions into the channel is impeded by the TJs, shown in sketch (2). Therefore, a higher value of V_{IN} is needed to dedope the PEDOT:PSS channel, such that the ($V_{OUT} - V_{IN}$) -transfer characteristics shift to the right. Upon opening of the TJs during PLL exposure (sketch (3)), the ion flow to the channel is restored, and the ($V_{OUT} - V_{IN}$) -transfer characteristics shift back to the left (lower V_{IN}). Finally, after exchanging the electrolyte and the time of recovery of TJs (sketch (4)) the ($V_{OUT} - V_{IN}$) -transfer characteristics shift back towards the situation of the closed membrane. **Fig. 4.2 b** represents the ($V_{OUT} - V_{IN}$) -transfer characteristics of all four experimental steps. The left shift caused by the opening of TJs during PLL exposure gives rise to a decay of V_{SW} , whereas a right shift of the ($V_{OUT} - V_{IN}$) -transfer characteristics due to recovery of the TJs leads to a resumption of V_{SW} . In **Fig. 4.2 c**, V_{SW} is monitored over the time of the experiment. To assure device stability, ($V_{OUT} - V_{IN}$)-transfer characteristics were measured over 1 h prior to cell layer integrity. Then a Transwell filter with

an integrated cell layer replaced the plain Transwell filter, shown in sketch (2). V_{SW} increased of ~ 45 mV, as the Caco-2 cell layer acted as a barrier for ions, shown in **Fig. 4.2 c**. For each sample the $(V_{OUT} - V_{IN})$ -transfer characteristics of the integrated cell layer with intact barriers were measured over 3 h to assure stable barrier functionality. When PLL was added in a medium concentration of $162 \mu\text{M}$ apical to the electrolyte, the volume was kept constant. We observe that 90 minutes after PLL exposure V_{SW} decayed to the level of the Transwell filter without cells. This demonstrates that the cell layer lost its barrier functionality indicating TJ opening. As a result of a subsequent exchange of the electrolyte apical and basal, V_{SW} resumed over 6 h almost to the level of the intact barrier with an increase of ~ 41 mV. The comeback of more than 90 % of its initial barrier functionality indicates a recovery of TJs. To sum up, reversible barrier modulation and more specifically TJ modulation was monitored with the OEECT in current-driven mode. We observe that the TJ opening occurs fast, whereas the recovery of the TJs is rather slow.

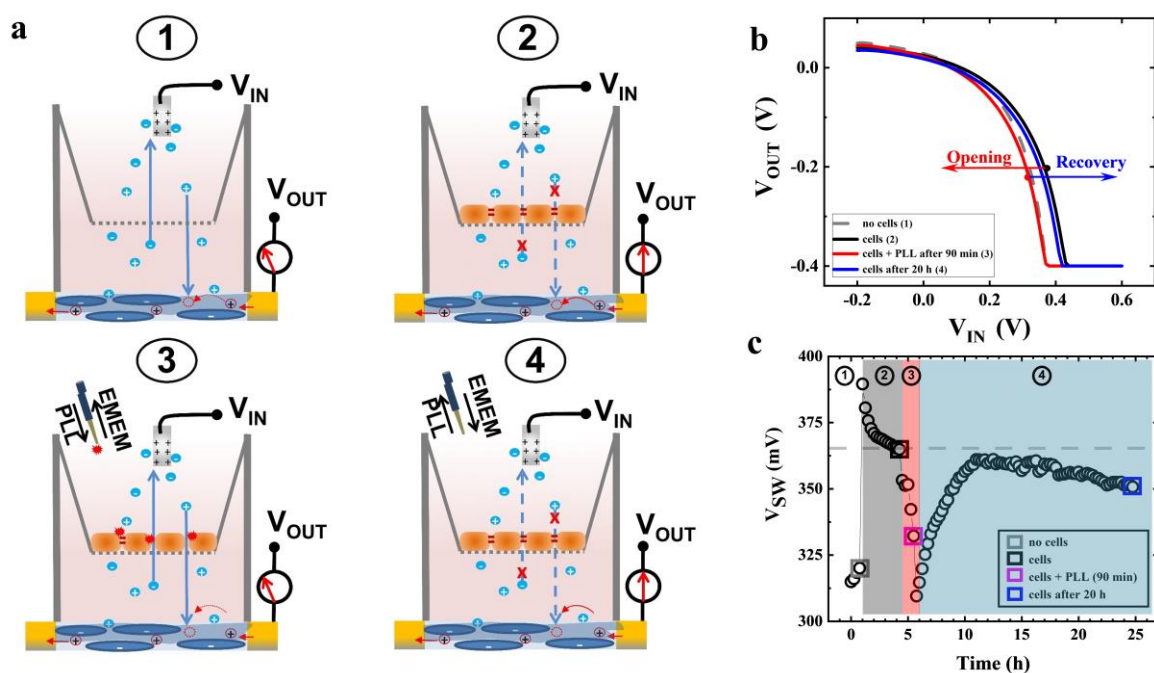


Figure 4.2: Sensing reversible tight junction modulation over time with a current-driven OEECT: **a)** Schematic of the four experimental steps performed under physiological conditions: The device with an integrated Transwell filter in absence (1) and in presence (2) of a Caco-2 cell layer; The barrier functionality of the integrated cell layer is symbolized by TJs (red). Addition of PLL, while keeping the electrolyte volume constant (3); Incubation after exchanging electrolyte apical and basal (4); The barrier functionality of the integrated cell layer is symbolized by TJs (yellow). **b)** $(V_{OUT} - V_{IN})$ -Transfer characteristics of a current-driven OEECT at $I_B = 0.5$ mA and $V_{DD} = -0.4$ V. Selected $(V_{OUT} - V_{IN})$ -transfer characteristics of the OEECT in absence (grey dashed, 1) and presence (black, 2) of the barrier tissue, 90 min after adding PLL (red, 3) and 20 h after exchanging the electrolyte (blue, 4). **c)** Monitoring the extracted V_{SW} of all measured $(V_{OUT} - V_{IN})$ -transfer characteristics over time of the experiment. Vertical grey lines help to distinguish experimental steps. Horizontal grey dashed lines indicate V_{SW} of an intact barrier tissue.

4.3.3 The concentration effect of TJ modulator PLL measured by current-driven OECT as a dynamic sensor for reversible tight junction modulation

Fig. 4.3 represents V_{SW} of ($V_{OUT} - V_{IN}$)-transfer characteristics measured with a current-driven OECT over time for various PLL concentrations. To investigate the concentration effect of PLL as TJ modulator on the cell barrier integrity, three concentrations have been tested: 81 μM (small), 162 μM (medium), and 324 μM (high). In the example for low PLL concentration, V_{SW} increased by ~ 55 mV when inserting a cell layer into the device set-up. The effect of a low PLL-concentration resulted in only a few mV changes in V_{SW} , as the barrier function is lost only slightly. Hence, the addition of a low PLL concentration had practically no effect on TJ modulation. After the exchange of electrolyte, a steady increase in V_{SW} overcoming the level of the intact cell barrier is observed. By adding a medium PLL concentration (162 μM), the effect was far more pronounced, as already presented in **Fig. 4.2**. Therefore, PLL in medium concentration served as a reversible TJ modulator. In contrast, upon adding a high PLL concentration (324 μM), V_{SW} decreased directly by ~ 40 mV to the reference response in absence of the cell layer and remained constant during and after the exposure. Hence, the effect of high PLL concentration had an irreversible effect on the cell barrier.

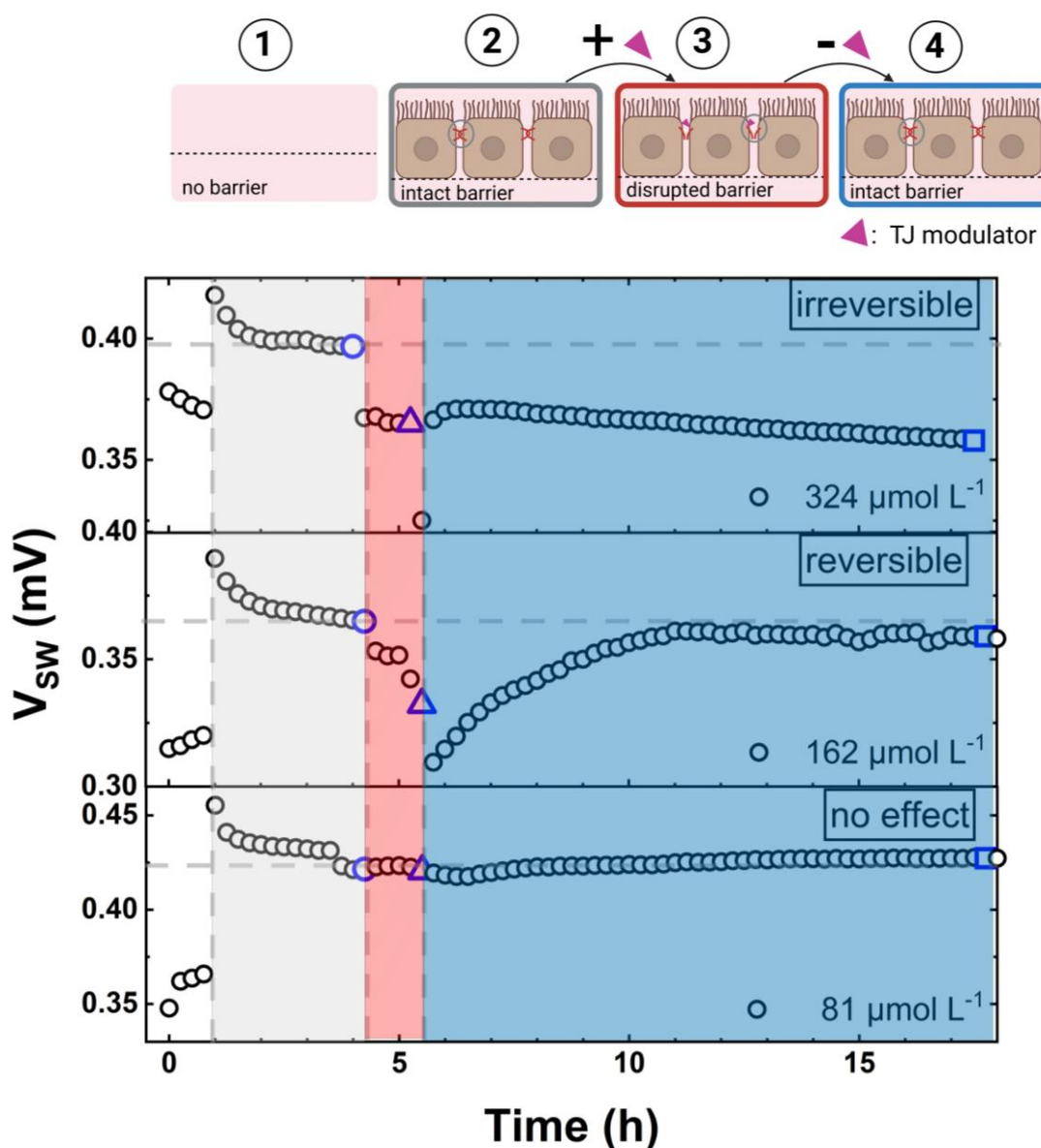


Figure 4.3 The concentration effect of TJ modulator PLL measured by current-driven OECT as an *in-situ* sensor for reversible tight junction modulation. V_{sw} over time of the experiment for three different concentrations of PLL (81 μM , 162 μM , 324 μM). Horizontal grey dashed lines indicate V_{sw} of an intact barrier tissue. Vertical grey dashed lines help to distinguish experimental steps.

A stable barrier functionality was provided over 24 h, implicating device stability, as demonstrated in **Fig. 4.4**. In this sample a V_{sw} alternation of ~ 2 mV was observed. The observed effective change of V_{sw} due to PLL treatment in medium and high concentration was of ~ 40 mV. Therefore, the latter is one order of magnitude higher than the standard derivation of tissue stability.

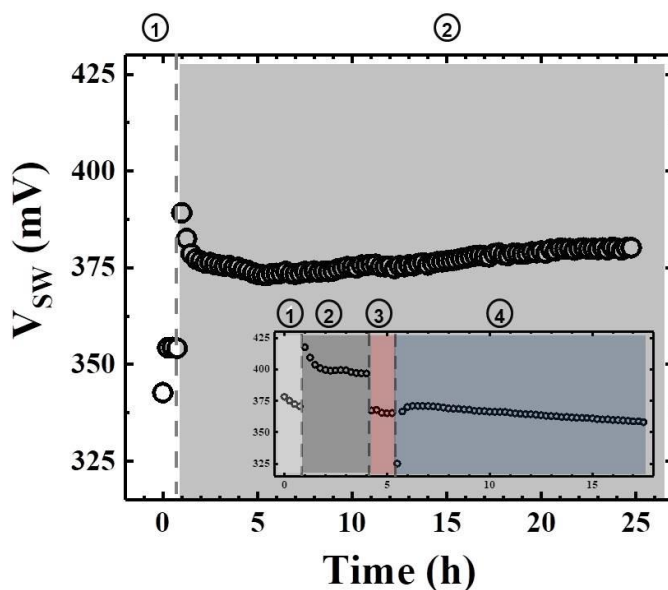


Figure 4.4: Stability measurement of a current-driven OECT with an integrated barrier tissue. Monitoring the extracted V_{SW} of all measured ($V_{OUT}-V_{IN}$)-transfer characteristics at $I_B = 0.3$ mA and $V_{DD} = -0.4$ V of an integrated cell layer compared to the effect of a high PLL concentration on a barrier tissue (small inset, see **Fig. 4.3**). Vertical grey dashed lines help to distinguish experimental steps (1), (2), (3) and (4).

The relatively fast opening of the TJs observed with the OECT is attributed to a displacement of proteins like occludin and zonulin.^[19] The recovery of the TJs is rather slow, as it requires the transport of occludin and zonulin to the cell membrane. Already Yu *et al.* and McEwan *et al.* have shown reversible permeability enhancement of PLL in a concentration from 5-100 $\mu\text{g mL}^{-1}$ exposed to kidney epithelium (MDCK I).^[15,42] For the bronchial epithelium (BEAS-2B), it was found that after 1 h exposure to 0.2-10 $\mu\text{g mL}^{-1}$ PLL, a full recovery of barrier function is maintained after 12 h. Barrier modulation is assumed to be caused by spontaneous transformations in intercellular junctions and cell proliferation.^[18] Recently, the effect of PLL in the concentrations 0.01 % and 0.001 % to urothelium was investigated exhibiting reversible TJ modulation. For Caco-2 cells, it is assumed that a recovery after PLL treatment is much faster as compared to Chitosan.^[19] The application of PLL in drug delivery as a permeability enhancer is reported to be successful.^[43]

Deionized water as solvent of PLL is affecting the osmotic pressure of the cell layer, but the effect of pure solvent was minor to the one seen upon the exposure to PLL, portrayed in **Fig. 4.5**.

The effect of deionized water as solvent of the PLL on barrier tissue was examined under the same conditions than PLL as TJ modulator and resulted in a relative decay of $\Delta V_{SW} = 3$ mV. This indicates that the observed decrease of V_{SW} seen after addition of PLL is not caused by its solvent. After exchanging the electrolyte, V_{SW} decreases by 13 mV relative to the

cell layer before the addition of water, caused by the loss of optimal physiological conditions. A full retrieval of equilibrium in osmotic pressure is observed 10 h after the exposure to water.

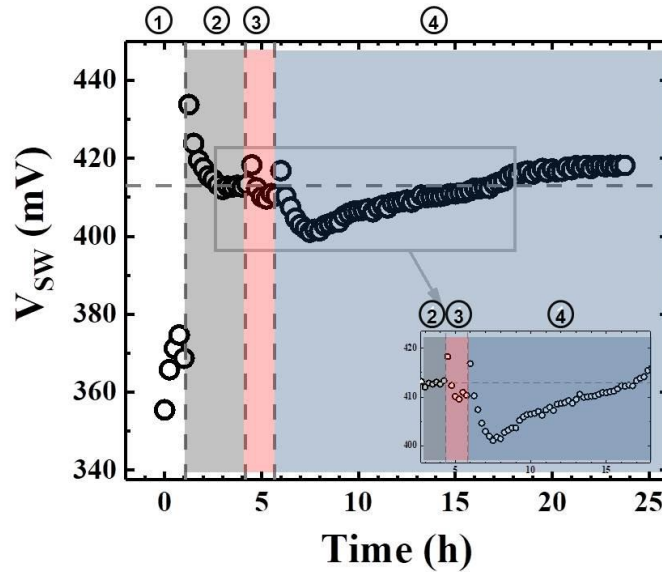


Figure 4.5: Sensing the effect of deionized water on Caco-2 barrier tissue over time with a current-driven OECT: Monitoring the extracted V_{SW} of all measured ($V_{OUT} - V_{IN}$)-transfer characteristics at $I_B = 0.2$ mA and $V_{DD} = -0.4$ V of an integrated cell layer under exposure of $162 \mu\text{M}$ H_2O . Vertical grey dashed lines help to distinguish experimental steps (1), (2), (3) and (4). Horizontal grey dashed lines indicate V_{SW} of an intact barrier tissue.

Also, an investigation of the cytotoxicity on Caco-2 cells exposed to PLL in four different concentrations over three different time durations is displayed in **Fig. 4.6**. Therefore, a luminescence-based cell viability assay was performed to measure the number of viable cells calculated from the quantitation of the ATP present, which indicates the existence of metabolically active cells. As a result, the PLL exposure has a time and concentration-dependent cytotoxic effect on Caco-2 cells. This effect is relatively weak at lower concentrations (81 and $162 \mu\text{M}$ PLL) with more than 70 % viable cells present even after 4 h of treatment. At a high concentration of PLL ($325 \mu\text{M}$) only half of the cells are viable after 1 h of treatment followed by a decrease in viability up to 18 % after 4 h. In accordance to the OECT's measurements, a recovery in cell viability is only observed at low and medium PLL concentrations, whereas at a high concentration, only 6 % Caco-2 cells are viable.

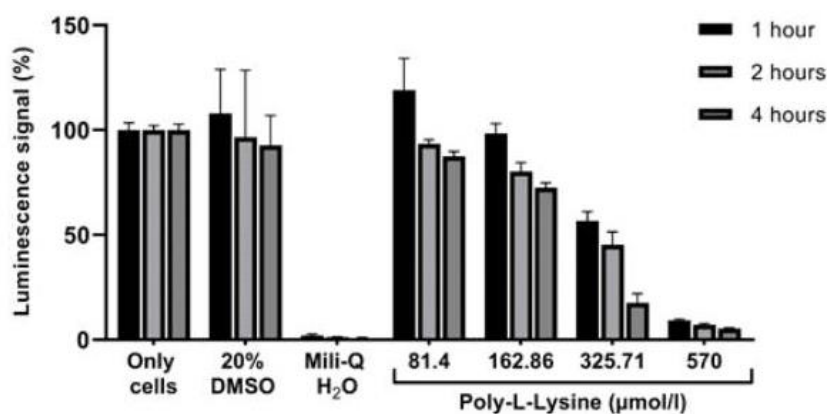


Figure 4.6: PLL toxicity on Caco2 cells is time and concentration dependent. Caco-2 cell viability, at day four of cultivation, were incubated with four different PLL concentrations at three different time points at 37 °C and 5 % CO₂. 20 % DMSO and Milli-Q water are used as positive control (n = 3).

In order to visualize the effect of PLL on Caco-2 cell barriers as measured with the current-driven OECT, additional immunofluorescent antibody labelling was performed to visualize TJ modulation by confocal laser scanning microscopy (cLSM). For this reason, the Caco-2 cells were exposed to PLL under similar conditions compared to the current-driven OECT (see Material and Methods for a detailed experimental description). The transmembrane protein occludin was immunocytochemically stained to highlight the effect on the TJ barrier integrity directly after PLL exposure, compared to staining after an incubation time of 20 h subsequent PLL exposure (**Fig. 4.7**). Regarding imaging directly after PLL exposure, samples under exposure of small and medium PLL concentrations (81 and 162 μmol L⁻¹) show almost no difference in the staining pattern of occludin compared to the untreated Caco-2 cells. However, the drop in resistance for a medium PLL concentration effect, monitored by a large alteration in V_{SW} with the current-driven OECT (**Fig. 4.2c**), is not visible in the occludin staining. It should be noted that conformational changes in the TJs occur on the nm scale, which are hard to resolve with a microscope. This shows that electrophysiological investigations of TJ modulation can have an advantage over microscopy. Regarding images 20 h after exchanging the electrolyte, occludin staining is fully visible, which is in agreement with the reversible effect measured with the current-driven OECT. However, occludin staining directly after a high PLL treatment (326 μmol L⁻¹) is clearly impaired. Here, the characteristic junctional organization of occludin is completely disrupted and reorganized into the intracellular compartments. Interestingly, subsequent to an incubation over 20 h after electrolyte exchange, the occludin staining is almost completely visible again.

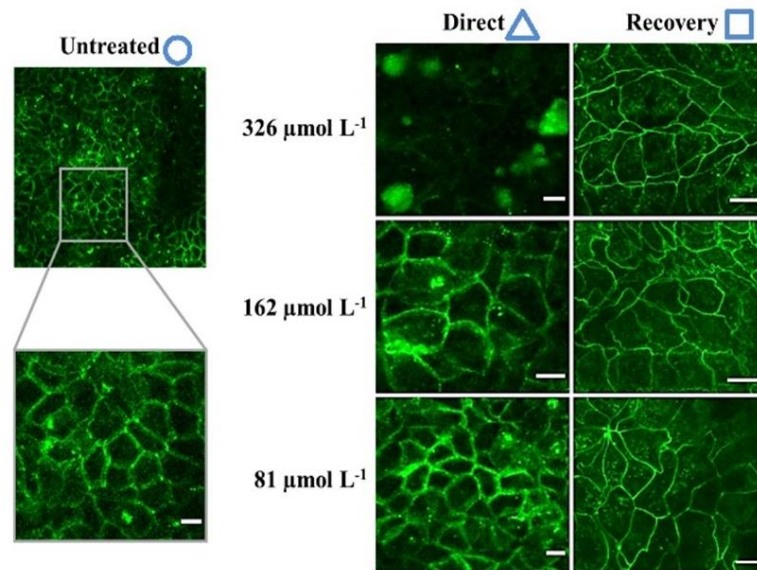


Figure 4.7: The concentration effect of TJ modulator PLL measured by immunofluorescence staining of occludin (green) in human CaCo-2 cells cultivated on day 14 on coverslips (1.12 cm^2) and treated with different concentration of PLL (detailed description in **Chapter 3.2.3**). All scale bars represent $10 \mu\text{m}$.

Therefore, when we combine the electrophysiological investigations with the visualization of TJ modulation, we conclude that the occludin proteins steadily reassemble during the 20 h recovery at the outer cell membranes. However, they either lose their functional properties of firmly sealing the adjacent cells or are not able to fully close all junctional cell connections, resulting in the inability of not being able to restore the initially measured barrier function. This effect can be seen both on Caco-2 cells grown on coverslips as well as on cells grown on Transwell filters (**Fig. 4.8**).

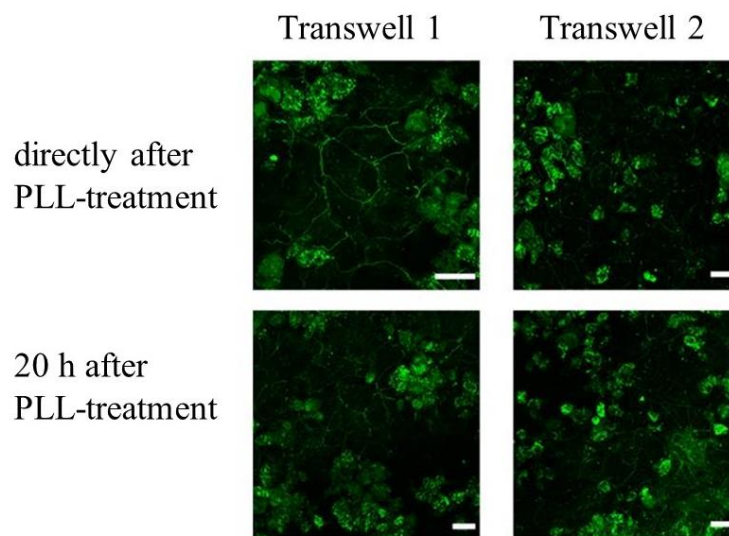


Figure 4.8: Redistribution of occludin staining after high PLL treatment and 20 h recovery under Transwell culture conditions. At day 14 of cultivation on two FluoroBlok™ Transwell filters (0.3 cm^2 ; pore size: $0.4 \mu\text{m}$), Caco-2 cells were treated with PLL ($326 \mu\text{mol L}^{-1}$) for 90 min followed by a recovery in fresh medium for 20 h at $37 \text{ }^\circ\text{C}$ and 5 % CO_2 . For the image acquisition, the cells were directly fixed, permeabilized, and occludin-stained. Exemplary pictures from two different Transwells are shown ($n=2$). All scale bars represent $25 \mu\text{m}$.

In addition, investigating the recovery behaviour of Caco-2 cells after PLL exposure in more detail, cell viability studies show that after an exposure to high PLL concentration, the cells are no longer metabolically active, leading to an increase in cytotoxicity (**Fig. 4.9**). As a result, tight junction proteins like occludin might still be present at their physiological site, however, they are not functional anymore because also the cells are not viable.

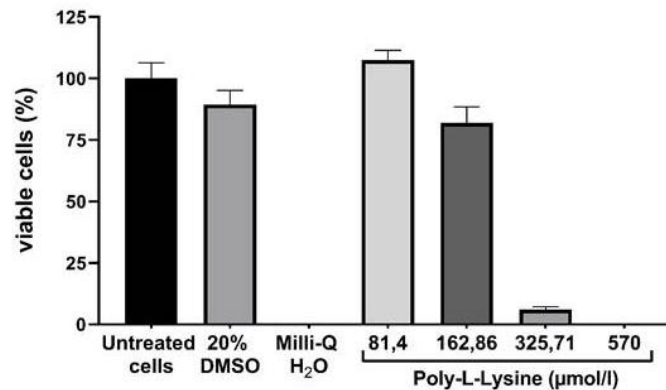


Figure 4.9: Caco2 cells show a cell recovery only after low PLL exposure. Caco-2 cell viability, at day four of cultivation, were incubated with four different PLL concentrations for 90 min followed by a recovery in fresh medium for 20 h at 37 °C and 5 % CO₂. 20 % DMSO and Milli-Q water are used as a positive control. The values for Milli-Q water and 570 µmol/L PLL are below 1 % (n = 3).

4.4 Conclusion

In conclusion, reversible TJ modulation has been detected with an OECT in current-driven configuration by investigating paracellular permeability across an epithelial cell barrier. It was demonstrated that a small PLL concentration is hardly affecting TJ properties, whereas a medium PLL concentration induces reversible TJ modulation. In contrast, a high PLL concentration causes irreversible alteration of TJ properties. With the OECT in current-driven configuration not only the process of TJ opening, but also of TJ closing can be precisely monitored as a variation of the output voltage. The work shows the progress of OECT technology towards *in vitro* testing of TJs for clinical applications and clinically-relevant timescales as drug targeting and screening.

4.5 References

- [1] M.S. Balda, L. Gonzfilez-Mariscal, R.G. Contreras, M. Macias-Silva, M.E. Torres-Marquez, J.A. Garcia-Sainz, and M. Cereijido, *J. Membrane Biol.* **1991**, *122*, 193-202.
- [2] M. A. Deli, *Biochemica et Biophysica Acta* **2009**, *1788*, 892.
- [3] J. Pionte, L. Winkler, H. Wolburg, S. L. Müller, N. Zuleger, C. Piehl, B. Wiesner, G. Krause, I. E. Blasig, *FaseB J.* **2008**, *22*, 146.
- [4] J. M. Anderson, C. M. van Itallie **1999**, R922-R924.
- [5] F. Ingels, S. Deferme, N. Delbar, M. Oth, P. Augustijns, *J. Pharm. Belg.* **2002**, 153.
- [6] A. S. Fanning, Mitic L., J. M. Anderson, *J. Am Soc. Nephrol.* **1999**, *10*, 1337.
- [7] J. M. Anderson, M. S. Balda, Fanning A. S., *Current Opinion in Cell Biology* **1993**, 772.
- [8] J. M. Anderson, *News Physiol. Sci.* **2001**, *16*.
- [9] K. Matter, M. S. Balda, *Int. Rev. Cytol.* **1999**, *1861*, 117.
- [10] J. M. Anderson, B. R. Stevenson, D. A. Goodenough, M. S. Mooseker, *J. Cell Biol.* **1986**, *103*, A71.
- [11] A. S. Fanning, van Itallie C.M., J. M. Anderson, *Molecular Biology of the Cell* **2012**, *23*, 577.
- [12] K. Sonaje, E.-Y. Chuang, K.-J. Lin, T.-C. Yen, F.-Y. Su, M. T. Tseng, H.-W. Sung, *Molecular pharmaceutics* **2012**, *9*, 1271.
- [13] Chelakkot, C., Ghim, J., Ryu, S.H., *Exp Mol Med* **2018**, *50*.
- [14] M. S. Balda, K. Matter, *Seminars in cell & developmental biology* **2000**, *11*, 281.
- [15] G.T.A. McEwan, M. A. Jepson, B. H. Hirst, N. L. Simmons, *Biochemica et Biophysica Acta* **1993**, *1148*, 51.
- [16] a) I. Westergren, B. B. Johansson, *Acta Physiol Scand.* **1993**, *149*, 99–104.; b) A. F. Kotzé, H. L. Luessen, B. J. de Leeuw, deBoer A.G., J. C. Verhoef, H. E. Junginger, *J Control Release.* **1998**, *51*, 35; c) G. Sandri, P. Poggi, M. C. Bonferoni, S. Rossi, F. Ferrari, C. Caramella, *J Pharm Pharmacol* **2006**, *58*, 1327.
- [17] a) C.-M. Lehr, J. A. Bouwstra, E. H. Schacht, H. E. Junginger, *Intern. J. of Pharm.* **1992**, *78*, 43; b) M. P. Deacon, S. MCGurk, C. J. Roberts, P. M. Williams, S.J.B. Tendler, M. C. Davies, S. S. Davis, S. E. Harding, *Biochem. J.* **2000**, *348*, 557.
- [18] R. F. Roblendo, M. W. D.S. Barber, *Toxicological Sci.* **1999**, *51*, 119.
- [19] G. Ranaldi, I. Marigliano, I. Vespignani, G. Perozzi, Y. Sambuy, *J. of Nutritional Biochemistry* **2002**, *13*, 157.
- [20] a) M. Ramuz, A. Hama, M. Huerta, J. Rivnay, P. Leleux, R. M. Owens, *Adv. Mater.* **2014**, 7083; b) S. Tria, L. H. Jimison, A. Hama, M. Bongo, R. M. Owens, *Biosensors* **2013**, 44.
- [21] L. H. Jimison, S. A. Tria, D. Khodagholy, Gurfinkel M., E. Lanzarini, A. Hama, G. G. Malliaras, R. M. Owens, *Adv. Mater.* **2012**, 5919.
- [22] B. Srinivasan, A. R. Kolli, M. B. Esch, H. E. Abaci, M. L. Shuler, J. J. Hickman, *J. of Lab. Autom.* **2015**, *20*, 107.
- [23] F. Decataldo, M. Barbalinardo, M. Tessarolo, V. Vurro, M. Calienni, D. Gentili, F. Valle, M. Cavallini, B. Fraboni, *Adv. Mater. Technol.* **2019**, 1.
- [24] a) J. Wegener, C. R. Keese, I. Giaever, *Experimental cell research* **2000**, *259*, 158; b) D. A. Koutsouras, L. V. Lingstedt, K. Lieberth, J. Reinholz, V. Mailänder, P. W. M. Blom, P. Gkoupidenis, *Adv. healthcare mater.* **2019**, *8*, e1901215.
- [25] Joachim Wegener, Dimitri Abrams, Wolfgang Willenbrink, Hans-Joachim Galla, and Andreas Janshoff, *BioTechniques* **2004**, *37*, 590.
- [26] S. A. Tria, M. Ramuz, M. Huerta, P. Leleux, J. Rivnay, L. H. Jimison, A. Hama, G. G. Malliaras, R. M. Owens, *Adv. Healthcare Mater.* **2014**, 1053.

- [27] S. T. Tria, L. H. Jimison, A. Hama, M. Bongo, R. M. Owens, *Biochemica et Biophysica Acta* **2013**, 1830, 4381.
- [28] D. A. Bernards, G. G. Malliaras, *Adv. Funct. Mater.* **2007**, 3538.
- [29] J. Rivnay, P. Leleux, M. Sessolo, D. Khodagholy, T. Hervé, M. Flocchi, G. G. Malliaras, *Adv. Mater. (Deerfield Beach, Fla.)* **2013**, 25, 7010.
- [30] J. Rivnay, P. Leleux, M. F. Ferro, M. Sessolo, A. Williamson, D. Koutsouras, D. Khodagholy, M. Ramuz, X. Stakos, R. M. Owens et al., *Sci. Adv.* **2015**, e1400251.
- [31] J. Rivnay, S. Inal, A. Salleo, R. M. Owens, M. Berggren, G. G. Malliaras, *Nat Rev Mater* **2018**, 3, 99.
- [32] a) D. Koutsouras, A. Hama, J. Pas, P. Gkoupidenis, B. Hivert, C. Faivre-Sarrailh, Pasquale E., R. M. Owens, G. G. Malliaras, *MRS Commun.* **2017**, 7, 259; b) J. Pas, C. Pitsalidis, D. A. Koutsouras, P. P. Quilichini, F. Santoro, B. Cui, L. Gallais, R. P. O'Connor, G. G. Malliaras, R. M. Owens, *Adv. Biosystems* **2018**, 2, 170014.
- [33] a) P. Gkoupidenis, N. Schaefer, B. Garlan, G. G. Malliaras, *Adv. Mater.* **2015**, 27, 7176; b) P. Gkoupidenis, D. A. Koutsouras, G. G. Malliaras, *Nature Commun.* **2017**, 8, 15448.
- [34] E. Stavrinidou, R. Gabrielsson, E. Gomez, X. Crispin, O. Nilsson, D. T. Simon, M. Berggren, *Sci. Adv.* **2015**, 1.
- [35] a) N. Y. Shim, D. A. Bernards, D. J. Macaya, J. A. DeFranco, M. Nikolou, R. M. Owens, G. G. Malliaras, *Sensors* **2009**, 9896; b) Yeung, S. Y., Gu, X., Tsang, C. M., Tsao, S. W. G., & Hsing, I. M., *Sensors and Actuators B: Chemical* **2019**, 297.
- [36] M. Ramuz, A. Hama, J. Rivnay, P. Leleux, R. M. Owens, *J. Mater. Chem. B* **2015**, 5971.
- [37] a) S. A. Tria, M. Ramuz, L. H. Jimison, A. Hama, R. M. Owens, *J. Visualized Exp.* **2014**, 84, 2; b) Yao, C., Xie, C., Lin, P., Yan, F., Huang, P., & Hsing, I. M., *Adv. Mater.* **2013**, 25, 6575.
- [38] J. Rivnay, M. Ramuz, P. Leleux, A. Hama, M. Huerta, R. M. Owens, *Appl. Phys. Lett.* **2015**, 43301.
- [39] M. Ghittorelli, L. Lingstedt, P. Romele, N. I. Crăciun, Z.M. Kovács-Vajna, P.W.M. Blom, F. Torricelli, *Nature Commun.* **2018**, 1441.
- [40] L. V. Lingstedt, M. Ghittorelli, M. Brückner, J. Reinholz, N. I. Crăciun, F. Torricelli, V. Mailänder, P. Gkoupidenis, P. W. M. Blom, *Adv. healthcare mater.* **2019**, 8, e1900128.
- [41] E. Cantatore, T. C. T. Geuns, G. H. Gelinck, E. van Veenendaal, A. F. A. Gruijthuijsen, L. Schrijnemakers, S. Drews, D. M. de Leeuw, *IEEE J. Solid-State Circuits* **2007**, 42, 84.
- [42] a) X. Y. Yu, B. H. Schofield, T. Croxton, N. Takahashi, E. W. Gabrielson, E. W. Spannhake, *Am. J. respiratory cell and molecular biology* **1994**, 11, 188; b) X. Y. Yu, N. Takahashi, T. L. Croxton, E. W. Spannhake, *Environmental health perspectives* **1994**, 102, 1068.
- [43] a) M. González Ferreiro, L.G.Tillman, G. Hardee, R. Bodmeier, *Pharm. research* **2002**, 19, 755; b) Y. Fang, J. Xue, L. Ke, Y. Liu, K. Shi, *Drug delivery* **2016**, 23, 3582.

5 High-sensitivity real-time monitoring of cellular barrier functionality with dynamic-mode current-driven organic electrochemical transistor

5.1 Summary

Cellular barriers regulate the fundamental physiological functions of animals and plants. Early detection and accurate quantification of barrier dysfunction require high-sensitivity real-time monitoring techniques operating in wide range of cellular barrier status. Current approaches target these ideal conditions only at the design stage assuming specific biological conditions, and a general approach enabling a dynamic configuration of the bioelectronic system considering the actual biological conditions is still an open challenge. Here we show real-time and high-sensitivity monitoring of cellular barrier functionality with dynamic-mode current-driven organic electrochemical transistors. Sensitivity can be enhanced in real-time during the experiments, ensuring the maximum performance in a very wide-range of biological conditions and avoiding multi-cycle design-experiment optimizations. We demonstrate a sensitivity equal to 203 mV dec^{-1} with an operating range of $13\text{-}640 \text{ } \Omega \text{ cm}^2$. The high-sensitivity and wide-range operation allow real-time monitoring of reversible barrier functionality using a tight-junctions modulator concentration as-low-as $122 \text{ } \mu\text{M}$. The ultra-low detection-limit combined with high-sensitivity and wide-range makes this approach a suitable technology for accurate monitoring subtle variations of barrier functionality offering opportunities for precision in-vitro medical diagnostic and next-generation in-vivo organic bioelectronics.

5.2 Introduction

Cellular barriers are essential biological interfaces for the physiological functions of animals, humans, and plants, being able to control the transport of ions, small molecules and nutrients through the separated compartments of a tissue. For instance, cellular barriers in plants contributes to the controlled uptake of water and mineral nutrients,^[1] while in human body are the major building blocks of various organs, including for example skin, lungs, liver, kidney, and digestive track. The physiological function of the biological barriers is diverse among tissues and responds to the specific needs of each organ, including ion absorption, nutrients uptake, protection against toxins, and secretion of waste.^[2] Under normal physiological conditions the transcellular and paracellular fluxes are finely regulated by the cellular barriers. Tight-junction (TJ) proteins – being responsible of the intercellular sealing – control the paracellular fluxes, providing either fully impermeable barriers or permeable-selective functions.^[3] The permeability of TJs in a cell barrier can be regulated by physiological cues, can be modulated by drugs, and can be altered by various biological events such as inflammation, gastrointestinal tract diseases, cancer metastases, leukocyte migration, and viral infections. For instance, disruption of epithelial and endothelial barriers is a key clinical data differentiating patients with high probability to develop severe COVID-19 symptoms including the escalation in respiratory deficiency, loss of viral containment and a progression toward multi-organ dysfunction.^[4] Analogously, blood-brain barrier disruption contributes to the severity of diverse neurological diseases, including stroke, epilepsy, Alzheimer's disease, and multiple sclerosis, among others.^[5] Therefore, monitoring the permeability of cellular barriers is essential to assess their functionality, to identify dysfunctions, to study a disease progression and to develop and test new drugs.^[6]

So far, the integrity of cellular barriers has been addressed with TER measurements. TER is an in-vitro measurement technique obtained by placing two chopstick-style electrodes on each side of a cell layer. Upon the application of a direct or alternate current, the ionic impedance of the barrier layer is measured. TER method is easy to perform but it suffers from low sensitivity, modest reproducibility, and limited temporal resolution.^[2a,7] By recording the ionic impedance at various frequencies, electrochemical impedance spectroscopies (EIS) provide a more optimized approach.^[8] EIS is a well-established method for cell-layer status detection but unfortunately it requires time-consuming measurements and modelling which limit the time resolution and increase the complexity. In addition, EIS measurements are based on small-amplitude signals, typically in the range of few milli-volts, and a suitable signal-to-noise ratio demands additional filtering and amplification operations, thus further increasing

the complexity of the experimental set-up and the cost of the equipment.^[9] In recent years, organic electrochemical transistors (OECTs) have been emerged as an effective alternative approach to electrically assess cellular barrier properties.^[10] OECTs are three-terminal iontronic devices where the electronic conductivity of an ionic-electronic conducting polymer channel connected by two electrodes, named source and drain, is modulated by a third electrode, named gate. The gate and the channel are in direct contact with an electrolyte and the polarity and magnitude of the applied gate voltage (V_G) result in a drift of anions or cations from the electrolyte to the channel and vice-versa.^[11] When an OECT is used for measuring a barrier tissue, the biological barrier can be placed in-between the gate and the channel. In this configuration, the ion transport depends on the barrier status that, in turn, is mirrored by the electrical characteristics of the OECT. The pioneering work of Owens and co-workers,^[9] demonstrated the application of an OECT as a sensor for barrier tissue by applying a pulsed V_G and measuring the drain-source current I_D . This approach enabled low-noise long-term measurements although high sensitivity operation required both model-based analysis of the recorded characteristics and barrier-dependent OECT design and set-up optimization.^[12] To avoid the need of post-processing, Hsing and co-workers proposed the direct coupling of cells' physiological ionic current that, in turn, was reflected in a change of the OECT threshold voltage.^[13] This approach was further optimized by Iannotta and co-workers that, focusing on the detection of irreversible barrier disruption, proposed the use of water as low ion concentration basal electrolyte but unfortunately a model-based analysis was re-introduced.^[14] To monitor the reversible barrier functionality with enhanced sensitivity and without the requirement of measurements modeling and post-processing analysis, we recently proposed the current-driven OECT configuration.^[15] Upon optimization of the OECT geometries, this method enabled the assessment of cellular barrier integrity when toxic compounds (H_2O_2) as low as 10^{-3} M were added to the cell media. Very recently, using the same approach, we demonstrated the monitoring of reversible TJs modulations over time.^[15,16] Therefore, while OECTs are a promising bioelectronic technology for the in-vitro investigation of the cellular barrier functionalities, current approaches require ad-hoc optimizations of the OECT design as well as of the cellular barrier geometries (e.g. the area) considering the expected specific range of the membrane resistance.^[12b,17] Under practical conditions, the inherent barrier-to-barrier biological variability typically results in a reduced sensitivity with respect to the design assuming nominal conditions. To overcome these fundamental limitations dynamically reconfigurable approaches enabling on-line real-time optimization of the bioelectronic system would be ideal. Even more importantly, the possibility of direct monitoring in real-time and

with high sensitivity a wide range of cellular barrier status, viz. barrier resistance, is still an open challenge.

Here we show real-time and high-sensitivity monitoring of cellular barrier functionality with dynamic-mode current-driven OECTs. In this approach the input voltage is dynamically swept forward and backward in a low-voltage range and the corresponding output voltage is measured. The output voltage provides a direct real-time quantification of the cellular barrier tissue status and functionality and no model-based data analysis is required. The output sensitivity can be enhanced on-line and in real-time, viz. directly during the experiments, by selecting the scan rate of the input signal during the real-time measurements. This ensures the maximum performance in a wide range of biological conditions also avoiding time-consuming multi-cycle design-experiments optimizations. The proposed approach demonstrates a sensitivity equal to 203 mV dec^{-1} with an operating range of $13 - 640 \Omega \text{ cm}^2$. The high-sensitivity and wide-range operation allow the real-time monitoring of reversible TJs modulation using a modulator concentration $c = 122 \mu\text{M}$. This ultra-low detection limit makes the dynamic-mode current-driven OECT a suitable technology for monitoring subtle variations of the barrier functionality offering opportunities for precision in-vitro medical diagnostic. Importantly, by using numerical circuit simulations we provide a clear rationale of the proposed approach, highlighting the key design parameters.

5.3 Results

5.3.1 Dynamic mode current-driven OECT

The current-driven OECT configuration integrating a barrier tissue is displayed in **Figure 5.1 a**. In this configuration the OECT is connected in series with a current generator setting a bias current I_B . The output voltage V_O is measured at the drain and the input voltage V_I is applied to a Ag/AgCl quasi-reference electrode. A Transwell filter with a barrier tissue is placed in-between the quasi-reference electrode gating the OECT and the polymeric channel and separates the electrolyte into two compartments. The prototypical ionic-electronic conductive polymer, the poly (3,4-ethylenedioxy-thiophene) doped with poly(styrene sulfonate) (PEDOT:PSS) is used for the OECT channel. PEDOT:PSS has been proven to be very stable in liquid environment even when in direct contact with the cell culture medium, thus enabling the operation under ideal biological conditions.^[18] The equivalent electronic circuit of the current-driven OECT embedding the Transwell filter with a biological membrane is displayed in **Fig. 5.1 b**. Specifically, R_G and R_A describes the non-polarizable gate electrode and the ion resistance due to the ion transport through the apical electrolyte, respectively, the barrier tissue membrane is modeled by a resistor R_M in parallel to a capacitor C_M , and R_F and R_B describes the ionic resistance of the Transwell filter and of the basal electrolyte, respectively. We note that R_M accounts for the ion transport through the cellular membrane while C_M models the ion accumulation at the apical and basal membrane interfaces.^[10b]

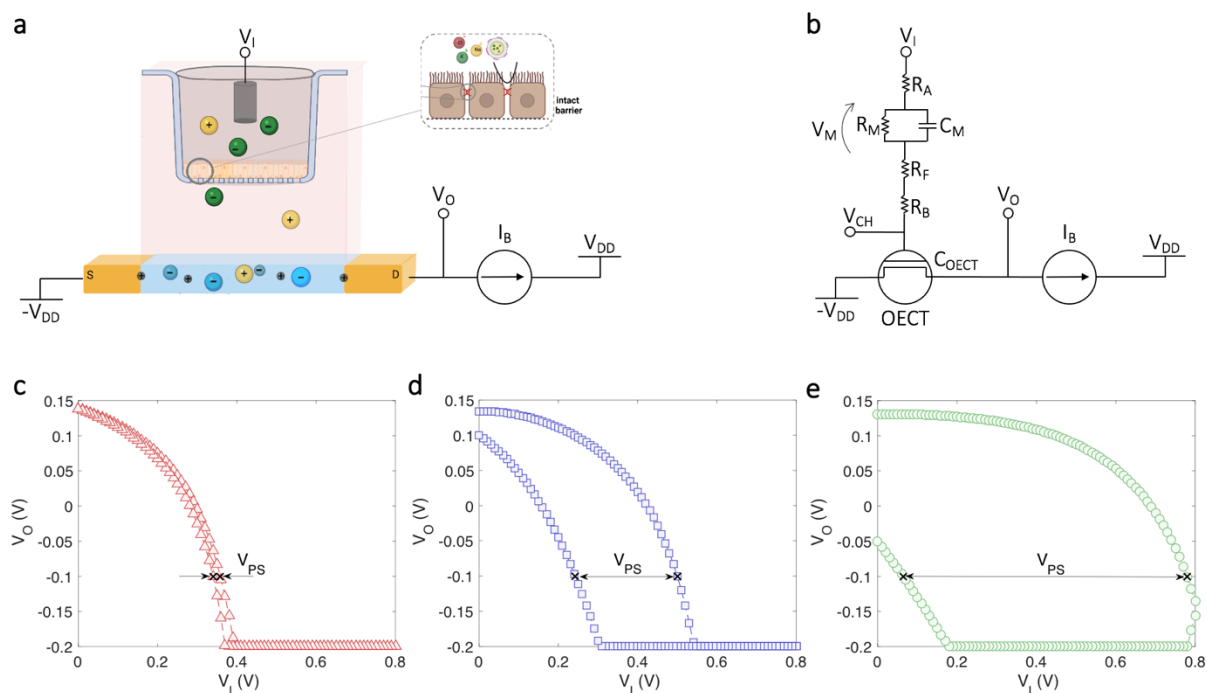


Figure 5.1: Dynamic-mode current-driven organic electrochemical transistor (OEET). **a)** Current-driven OEET configuration coupled with a biological barrier. The cellular barrier tissue is seeded in a Transwell-filter and cell medium is used as electrolyte. The gate electrode is immersed in the apical compartment and the OEET channel is in contact with the basal compartment. The ion transport between the two compartments depends on the status of the barrier tissue. Created with BioRender.com. **b)** Equivalent circuit model of a dynamic-mode current-driven OEET coupled with a biological barrier tissue. The barrier tissue is modeled as a resistor R_M in parallel to a capacitor C_M . R_M accounts for the ion transport across the barrier and C_M models the ion accumulation at the apical and basal barrier interfaces. R_A and R_B are the ionic resistance of the apical and basal electrolyte, respectively. R_F is the ionic resistance of the Transwell filter and C_{OEET} is the overall capacitance of the OEET polymeric channel. V_I is the input voltage, V_{CH} is the voltage actually gating the OEET, V_{DD} is the supply voltage, I_B is the bias current and V_O is the output voltage. **c)** Typical phase transfer characteristic V_O - V_I of a dynamic current-driven OEET operated at a scan rate $SR = 0.002 \text{ V s}^{-1}$. The phase-shift voltage V_{PS} is displayed. **d)** Measured V_O - V_I at $SR = 0.15 \text{ V s}^{-1}$. **e)** Measured V_O - V_I at $SR = 0.5 \text{ V s}^{-1}$. The gate is a Ag/AgCl pellet, the OEET geometries are: $W = 2 \text{ mm}$, $L = 1 \text{ mm}$, thickness $t = 300 \text{ nm}$. $I_B = 5 \cdot 10^{-3} \text{ A}$ and $V_{DD} = 0.2 \text{ V}$.

The aforementioned parameters are experimentally obtained by means of EIS measurements, as detailed in **Figure 5.2**.

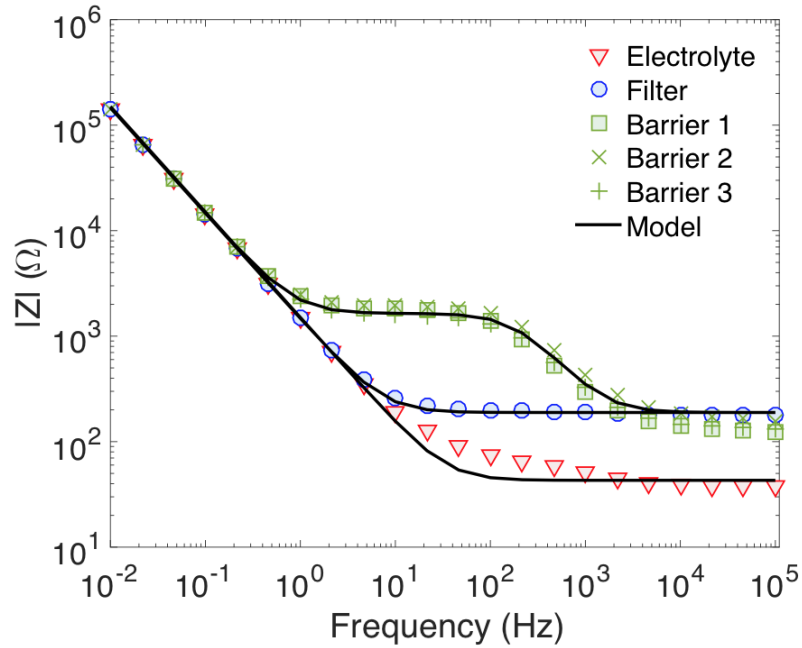


Figure 5.2: Electrochemical impedance spectroscopies. **a)** Typical electrochemical impedance spectroscopies (EIS) of OECTs with cell medium only used as electrolyte (triangles), OECT with Transwell filter (circles), OECT with Transwell filter and various nominally identical barrier tissue tissues (square, cross, plus). The full line is calculated with the lumped circuit model, which accurately reproduces the measurements. **b)** Lumped circuit model where R_A is the apical electrolyte resistance, R_M and C_M is the cellular barrier resistance and capacitance, respectively, R_F is the ionic resistance of the Transwell filter, R_B is the basal electrolyte resistance, and C_{OECT} is the overall capacitance of the OECT channel. The various EIS enabled us to disentangle the various parameters. More in detail, the EIS of the bare OECT with the cell culture medium used as electrolyte provided R_A , R_B and C_{OECT} , the EIS of the OECT with the Transwell filter provided R_F and the EIS of the OECT with the various cell barrier tissues yields R_M and C_M .

The OECT channel is described considering the ionic-electronic volumetric capacitance and the transport in the electronic channel. The OECT parameters are extracted by modeling the transfer and output characteristics, as displayed in **Figure 5.3**.

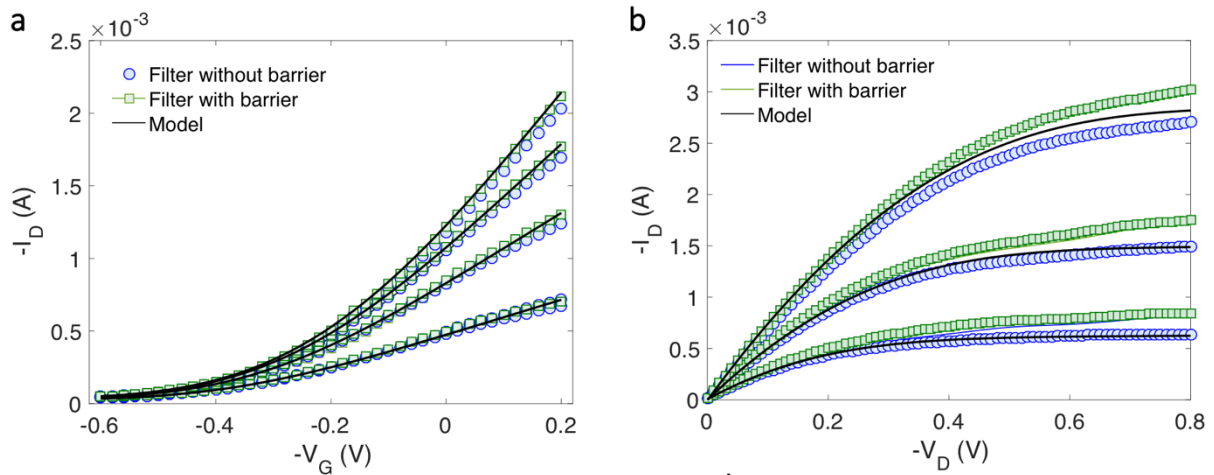


Figure 5.3: Electrical characteristics of OECTs without and with cellular barrier tissue. **a)** Typical transfer characteristics and **b)** typical output characteristics OECTs without (triangles, $\text{TER} = 13 \Omega\text{cm}^2$) and with cellular barrier tissue (squares, $\text{TER} = 640 \Omega\text{cm}^2$). Symbols are the measurements and lines are calculated with the OECT model showed in Ref. [19] including the channel length modulation.^[11a] In all cases the cell media is used as electrolyte. The characteristics of the OECTs without and with the cellular barrier tissue are almost perfectly overlapped showing that the barrier tissue has a minor impact on the steady-state electrical characteristics. The measurements are accurately described by the OECT model and the channel parameters Γ , V_T and λ are obtained.

The idea is to monitor the status of the cellular barrier taking advantage of the transient response of the ionic-electronic biological system. A typical transfer characteristic (V_O - V_I) of the dynamic-mode current-driven OECT integrating a cellular barrier is displayed in **Fig. 5.1 c**. The input voltage V_I is swept forward and backward, from 0 V to 0.8 V and back to 0.8 V, and the corresponding output voltage V_O is measured. When V_I is swept with a slow scan rate, e.g. $SR = 0.002 \text{ V s}^{-1}$ in **Fig. 5.1 c**, the forward and backward characteristics are almost perfectly overlapped. More in detail, when $V_I = 0 \text{ V}$ the p-type OECT is highly conductive and pulls-up the output voltage, resulting in $V_O = +V_{DD}$. By increasing the input voltage V_I , the OECT channel resistance (R_{OECT}) increases, I_B is set by the current generator, the voltage drop on the OECT channel ($V_{SD} = R_{OECT} I_B$) increases and, as a consequence, $V_O = V_{DD} - R_{OECT} I_B$ reduces. Further increasing V_I , the switching voltage V_{SW} is achieved ($V_{SW} = 0.39 \text{ V}$ in **Fig. 5.1 c**), the OECT operates in saturation and V_O is pulled-down to the minimum supply voltage, viz. $V_O = -V_{DD}$. By increasing the scan rate of the input voltage, the forward and backward characteristics do not overlap anymore, and the V_O - V_I characteristic shows a hysteretic loop, as displayed in **Fig. 5.1 d and 5.1 e**. The switching voltage of the forward characteristic (V_{SWf}) is larger than the switching voltage of the backward characteristic (V_{SWb}) and the voltage difference $V_{PS} = V_{SWf} - V_{SWb}$ increases by increasing SR . For instance, when $SR = 0.15 \text{ V s}^{-1}$ (**Fig. 5.1 d**) $V_{SWf} = 0.50 \text{ V}$, $V_{SWb} = 0.24 \text{ V}$ and $V_{PS} = 0.26 \text{ V}$, that increases to $V_{PS} = 0.72 \text{ V}$ when $SR = 0.5 \text{ V s}^{-1}$ (**Fig. 5.1 e**).

This can be explained as follows. In the dynamic-mode current-driven OECT configuration, a triangular waveform with amplitude V_I and frequency f_I is applied as input. The frequency f_I is modulated by SR and reads: $f_I = SR (V_{max} - V_{min})$, where V_{max} and V_{min} are the maximum and minimum amplitude of V_I , respectively. In our case $V_{min} = 0$ V and $V_{max} = 0.8$ V (**Figs. 5.1c-e**). Considering the lumped circuit model in **Fig. 5.1b**, the amplitude and phase of the voltage actually gating the OECT channel, named V_{CH} , depends on the input frequency f_I and on the time-response of the R-C circuit accounting for the impedance of the cellular barrier (R_M , C_M), electrolyte resistance (R_A and R_B), Transwell filter resistance (R_F) and OECT capacitance (C_{OECT}). A detailed calculation regarding the applied model of the dynamic-mode current driven OECT used for the numerical circuit simulations is provided below.

According to the circuit model displayed in **Fig. 5.1 b**, the channel voltage V_{CH} can be related to the input voltage V_I and output voltage V_O as follows:

$$V_{CH} = H_1(s)V_I + H_2(s)V_O \quad (1)$$

where

$$H_1(s) = \frac{1}{1+s Z_I C_{OECT}} \quad (2)$$

$$H_2(s) = \frac{s Z_I C_{OECT}}{2} H_1(s) \quad (3)$$

$$Z_I(s) = R_A + \frac{R_M}{1+s R_M C_M} + R_F + R_B \quad (4)$$

$s = j 2 \pi f$, $j = \sqrt{-1}$ and f is the frequency. Then, the electronic current flowing through the polymeric channel (I_D) is calculated using the Bernards-Malliaras model ^[19] including the channel length modulation,^[11a] and considering the current-driven circuit topology ($I_D = I_B$) it reads:

$$I_B = \Gamma \left(V_{DD} - V_{CH} + V_T - \frac{V_{DD}-V_O}{2} \right) (V_{DD} - V_O) \quad \text{if} \quad V_{CH} - V_T < V_O \quad (5)$$

$$I_B = \Gamma (V_{DD} - V_{CH} + V_T)^2 [1 + \lambda (V_{DD} - V_O)] \quad \text{if} \quad V_{CH} - V_T \geq V_O \quad (6)$$

where $\Gamma = \left(\frac{W}{L}\right) t_p \mu C_V$, W and L is the channel width and length, respectively, t_p is the thickness of the polymeric channel, μ is the electronic mobility and C_V the volumetric capacitance. I_B is the bias current set by the current generator, V_{DD} is the supply voltage, V_T is the OECT threshold voltage and λ accounts for the channel length modulation.

By means of the circuit simulator, the set of non-linear equations (1), (5) and (6) are coupled and solved together as a function of time. The transient simulations eventually provides the V_O - V_I transfer characteristics of the dynamic-mode current-driven OECT. In our simulation we applied as input voltage V_I a triangular waveform with frequency $f_I = SR (V_{max} - V_{min})$, where SR is the scan rate, V_{max} and V_{min} are the maximum and minimum amplitude of V_I , respectively.

5.3.2 Operation Mechanism

Since V_I is a large-signal triangular wave and the current-driven OECT gives rise to a non-linear input-output characteristic (I_D - V_{CH}), a linear analysis cannot be applied and numerical non-linear simulations are required. To this aim, we implemented the equivalent circuit displayed in **Fig. 5.1 b** in a numerical simulator accounting for the physical parameters obtained from the EIS, I_D - V_G , and I_D - V_D measurements (**Fig. 5.2** and **Fig. 5.3**). As displayed in **Fig. 5.4 a**, the simulations accurately predict the measurements in the whole range of V_I and SR .

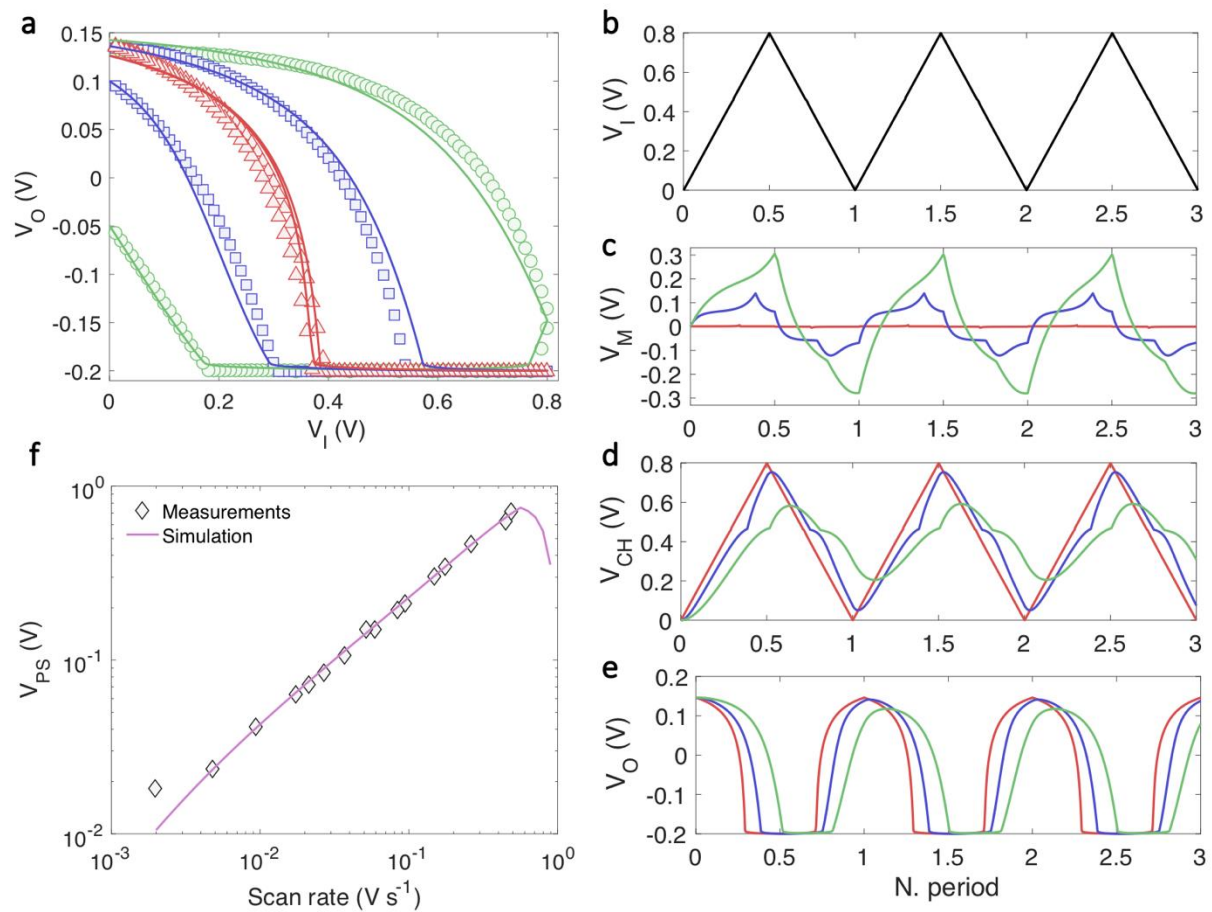


Figure 5.4: Operation mechanism. **a)** Measured (symbols) and model (lines) transfer characteristics (V_O - V_I) as a function of the scan rate $SR = 0.002 \text{ V s}^{-1}$ (triangles), $SR = 0.15 \text{ V s}^{-1}$ (squares), and $SR = 0.5 \text{ V s}^{-1}$ (circles). **b)-e)** Simulations of dynamic-mode current-driven OECT with a cellular barrier. Applied input voltage V_I , calculated voltage across the cellular barrier V_M , channel voltage V_{CH} and output voltage V_O as a function of time normalized to the input frequency $N_P = \text{time} (V_{max} - V_{min}) SR^{-1}$, where V_{max} and V_{min} are the maximum and minimum applied input voltage. Scan rate: $SR = 0.002 \text{ V s}^{-1}$ (red line), $SR = 0.15 \text{ V s}^{-1}$ (blue line), and $SR = 0.5 \text{ V s}^{-1}$ (green line). **f)** Phase-shift voltage V_{PS} as a function of the scan rate SR . Symbols are the measurements and line is calculated with the numerical simulations. Applied bias conditions: $I_B = 5 \cdot 10^{-3} \text{ A}$ and $V_{DD} = 0.2 \text{ V}$.

To gain more insight on the operation of the dynamic-mode current-driven OECT embedding a cellular barrier, we calculated the transient responses as a function of SR . For the sake of clarity, the various time responses are normalized to the corresponding SR . **Fig. 5.4 b - e** show the input voltage (V_I), the potential drop across barrier tissue (V_M), the actual potential

gating the OEET (V_{CH}), and the output voltage (V_O) as a function of the number of periods $N_P = \text{time} (V_{max} - V_{min}) SR^{-1}$. When $SR = 0.002 \text{ V s}^{-1}$, V_M is negligible, V_{CH} shows the same amplitude and phase of V_I (**Fig. 5.7 d**, red line), and the forward and backward V_O - V_I characteristics are almost overlapped (**Fig. 5.4 a**, red line). By increasing the scan rate at $SR = 0.15 \text{ V s}^{-1}$, the impedance of the OEET decreases, the voltage drop on the cellular membrane increases at about $V_M \approx 0.2 \text{ V}$ and the V_M oscillation is in phase with the input signal V_I (**Fig. 5.4 c**, blue line). Conversely, V_{CH} is attenuated and shifted with respect to V_I (**Fig. 5.4 d**, blue line) and, as displayed in **Fig. 5.4 e** (green line), this is mirrored in a phase-shift of V_O . This behavior is confirmed by further increasing the scan rate at $SR = 0.5 \text{ V s}^{-1}$. In this condition, $V_M \approx 0.6 \text{ V}$ (**Fig. 5.4 c**, green line), V_{CH} is significantly attenuated and shifted with respect to V_I , and the corresponding V_O shows an increased phase-shift (**Fig. 5.7 e**, green line). Focusing on the amplitude of V_O , the maximum output voltage slightly decreases at the maximum SR while the minimum output voltage is not altered ($V_{Omin} = -V_{DD}$, $V_{DD} = 0.2 \text{ V}$). This behavior is inherently due to the OEET current-driven configuration: the pull-up towards V_{DD} depends on the overdrive voltage $V_{DD} - V_{CH}$ applied to the OEET, while the output pull-down towards $-V_{DD}$ is achieved by means of the current generator I_B . As a result, in a dynamic-mode current-driven OEET the voltage $V_{PS} = V_{SWf} - V_{SWb}$ is related to the input-output phase shift, providing a direct measurement of the resistance of the cellular barrier. Indeed, this hysteretic behavior disappears when the V_O - V_{CH} characteristics are plotted (**Fig. 5.5**), confirming that V_{PS} provides information on the status of the barrier tissue. Interestingly, the provided analysis indicates that the sensitivity can be enhanced by means of SR.

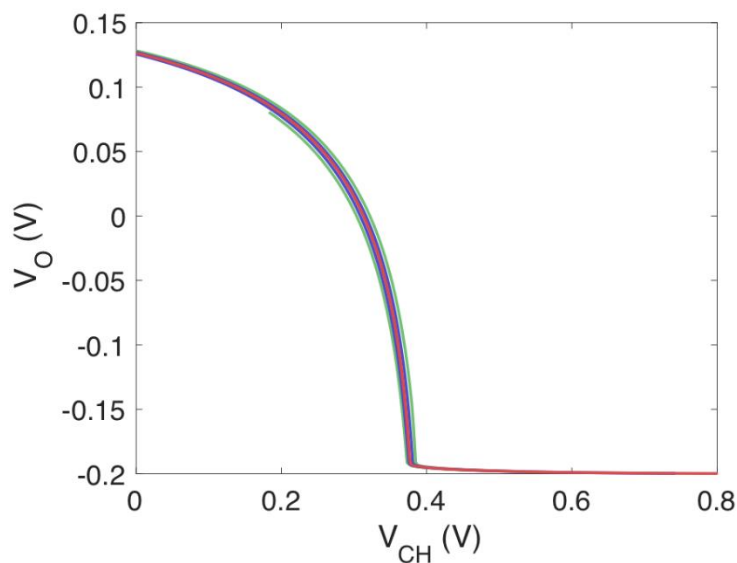


Figure 5.5: Impact of the scan rate on the OEET characteristics. Output voltage V_O as a function of the channel voltage V_{CH} at various scan rate SR . $SR = 0.002 \text{ V s}^{-1}$ (red line), $SR = 0.15 \text{ V s}^{-1}$ (blue line), and $SR = 0.5 \text{ V s}^{-1}$ (green line). The various characteristics are almost perfectly overlapped showing that the OEET response is independent of SR and the phase-shift is inherently due to the cellular barrier tissue.

Fig. 5.4 f shows the measured V_{PS} (symbols) as a function of SR . V_{PS} systematically increases by increasing SR in the range $2 \cdot 10^{-3} - 5 \cdot 10^{-1} \text{ V s}^{-1}$. At $SR = 0.5 \text{ V s}^{-1}$ we obtained $V_{PS} = 0.72 \text{ V}$, which is 90 % of the maximum input voltage. Overall, the dynamic-mode current-driven OECT shows a scan-rate sensitivity equal to $1391 \text{ mV V}^{-1} \text{ s}$. The simulations (**Fig. 5.4 f** full line) accurately predict the measurements showing that the maximum performance is achieved. Indeed, further increasing SR the voltage drop on the cellular barrier increases as well, resulting in a decreasing of V_{CH} . As a consequence, although the phase-shift increases, the OECT current reduces eventually resulting in a smaller V_{PS} . (**Fig. 5.6**).

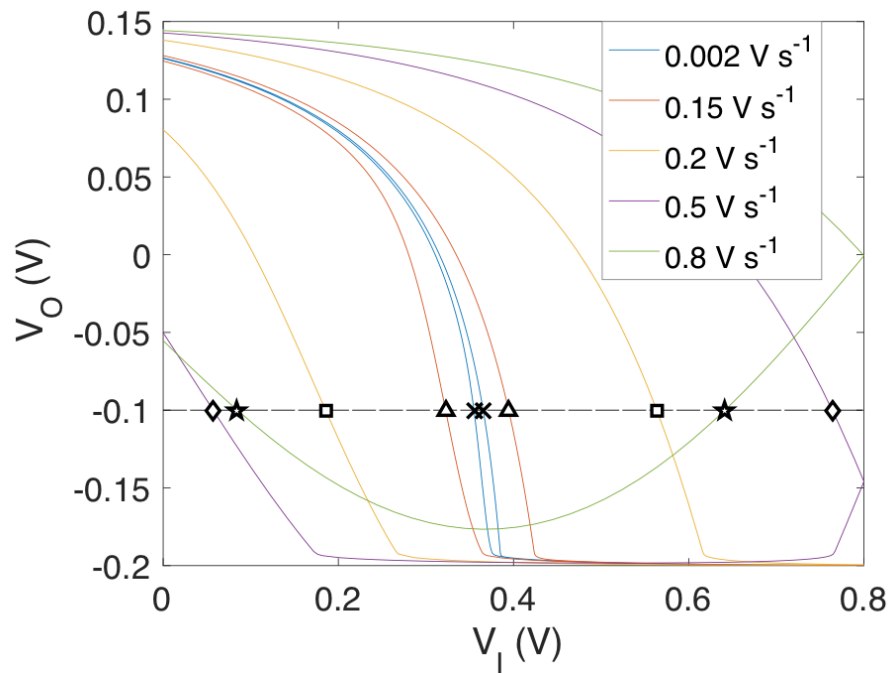


Figure 5.6: Impact of the scan rate on the V_O - V_I characteristics. Calculated V_O - V_I transfer characteristics as a function of the scan rate SR . The parameters of the dynamic-mode current-driven OECT are the same of **Fig. 5.4**. The symbols highlight V_{PS} for each curve obtained with a different SR . By increasing SR from 0.002 V s^{-1} to 0.5 V s^{-1} , V_{PS} consistently increases (crosses, triangles, squares, diamonds) while at larger SR , e.g. $SR = 0.8 \text{ V s}^{-1}$ V_{PS} decreases (stars).

To investigate the range of operation of the dynamic-mode current driven OECT, the ionic resistance between the gate and the channel is systematically varied considering four relevant cases: (I) cell medium electrolyte only ($R = 13 \Omega \text{ cm}^2$), (II) cell medium with Transwell filter ($R = 20 \Omega \text{ cm}^2$), (III) low-resistance barrier ($R = 320 \Omega \text{ cm}^2$), and (IV) high-resistance barrier ($R = 640 \Omega \text{ cm}^2$). We note that this range of resistances covers the relevant biological conditions, including intact and fully disrupted barrier tissues as well as the bare experimental set-up. **Fig. 5.7 a** shows the corresponding V_O - V_I measurements when $SR = 0.5 \text{ V s}^{-1}$. V_{PS}

consistently increases by increasing the ionic resistance R . To quantitatively evaluate the effect of the ionic resistance on V_{PS} , we calculated $\Delta V_{PS} = V_{PS} - V_{PS}(I)$ where $V_{PS}(I)$ is the value of V_{PS} obtained in the reference case (I) where only the electrolyte is used. **Fig. 5.7 b** shows ΔV_{PS} as a function of ionic resistance R : V_{PS} increases by a factor of two. More in detail, by inserting the Transwell filter into the electrolyte R increases from $13 \Omega \text{ cm}^2$ to $20 \Omega \text{ cm}^2$ resulting in a $\Delta V_{PS} = 226.2 \text{ mV}$. ΔV_{PS} increases to 327.8 mV when $R = 320 \Omega \text{ cm}^2$ (Transwell filter with a confluent barrier tissue of “low-resistance” Caco-2 cell line) and $\Delta V_{PS} = 445.3 \text{ mV}$ when $R = 640 \Omega \text{ cm}^2$ (Transwell filter with “high-resistance” Caco-2 cells). The least-square linear approximation of the measured ΔV_{PS} (circles in **Fig. 5.7 b**) as a function of R yields an average sensitivity $AR = dV_{PS}/dR = 353.4 \cdot 10^{-6} \text{ V } (\Omega \text{ cm}^2)^{-1}$ that corresponds to 203 mV dec^{-1} . We note that case (I) is very relevant for evaluating the experimental set-up but it is of limited practical interest when monitoring the barrier tissues and therefore it was not considered in the calculation of sensitivity. Therefore, the sensitivity is provided in the most challenging conditions. To further assess the effectiveness of the proposed approach, we measured the V_O - V_I input-output characteristics as a function of ionic resistance at various SR . **Fig. 5.7 c** shows that V_{PS} monotonically increases with R and the sensitivity AR systematically increases by increasing SR . More in detail, by increasing SR the phase-shift between the input signal V_I and the voltage V_{CH} modulating the OECT channel increases resulting in a larger magnitude of V_{PS} and in an enhanced sensitivity to the ionic resistance R . This is confirmed in **Fig. 5.7 d** where AR as a function of the SR is displayed. When the scan rate is very slow, $V_{CH} = V_I$, viz. same amplitude and phase, making impossible detecting variations of the barrier tissue. By contrast, at large SR , e.g. $SR = 0.5 \text{ V s}^{-1}$, a large phase shift between V_I and V_{CH} is obtained because of the voltage partition between the ionic impedance of the barrier tissue and the ionic-electronic

volumetric capacitance of the OEET and this, in turn, is converted in a large variation of V_{PS} by the dynamic-mode current-driven OEET.

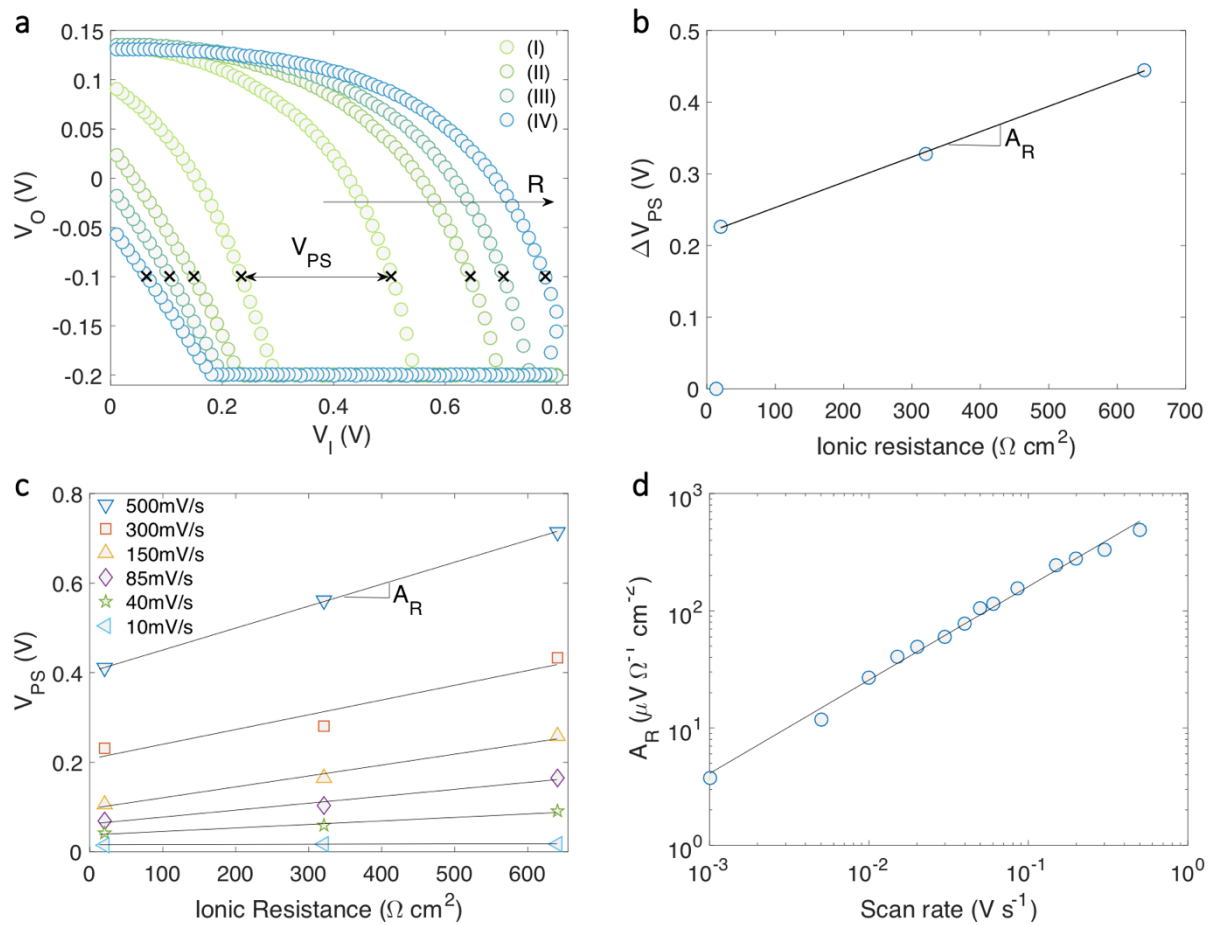


Figure 5.7: Wide range high sensitivity operation. **a)** Measured transfer characteristics (V_O - V_I) as a function of ionic resistance R . Four relevant cases are considered: (I) cell medium $R = 13 \Omega \text{ cm}^2$, (II) cell medium with Transwell filter $R = 20 \Omega \text{ cm}^2$, (III) low-resistance barrier $R = 320 \Omega \text{ cm}^2$, and (IV) high-resistance barrier $R = 640 \Omega \text{ cm}^2$. Considering the model displayed in **Fig. 5.1 b**, $R = R_A + R_M + R_F + R_B$. In all cases $SR = 0.5 \text{ V s}^{-1}$. The cross symbols indicate the forward and backward switching voltage for the various cases and, as an example, the phase-shift voltage V_{PS} is explicitly shown in the case (I). **b)** Variation of the phase-shift voltage $\Delta V_{PS} = V_{PS} - V_{PS(I)}$ as a function of the ionic resistance R . $V_{PS(I)}$ is V_{PS} obtained in the reference case (I). $SR = 0.5 \text{ V s}^{-1}$. Full line is the linear least square fit to the measurements and yields a sensitivity to the ionic resistance $A_R = 353.4 \cdot 10^{-6} \text{ V } (\Omega \text{ cm}^2)^{-1}$ that corresponds to 203 mV dec^{-1} . **c)** Measured V_{PS} as a function of the ionic resistance R by varying SR showing that A_R consistently increases by increasing SR . **d)** Calculated average A_R as a function of SR . Applied bias conditions: $I_B = 5 \cdot 10^{-3} \text{ A}$ and $V_{DD} = 0.2 \text{ V}$.

The analysis is corroborated in **Fig. 5.8** showing that V_{PS} depends on R and the sensitivity can be significantly enhanced by means of SR .

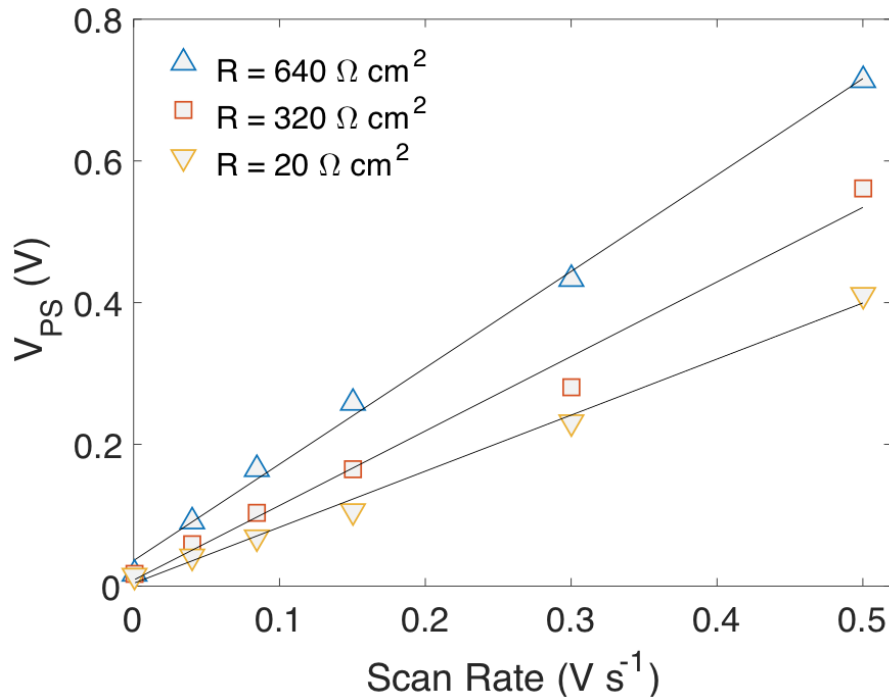


Figure 5.8: Impact of the scan rate and ionic resistance. Phase-shift voltage V_{PS} as a function of the scan rate SR by varying the ionic resistance R . V_{PS} consistently increases by increasing SR and R .

As a relevant application, high-sensitivity real-time monitoring of cellular barrier functionality is demonstrated. As a model system, we used confluent barrier tissue of the Caco-2 cell line. Caco-2 cells are widely used as a model of intestinal barrier permeability, which is the major barrier separating our body from the external environment and it is essential to avoid any imbalance in homeostasis.^[20] For instance, an imbalance in the intestinal barrier can give rise to an uncontrollable immune reaction or various diseases including inflammatory disorders, rheumatoid arthritis and metabolic disorders, e.g. obesity and diabetes.

5.3.3 High-sensitivity real-time monitoring of cellular barrier functionality

As a first step, the dynamic-mode current-driven OECT approach is benchmarked with the state-of-art OECT approaches including transient response OECT measurements and conventional current-driven OECT.^[21] As displayed in **Fig. 5.9 a**, the cell media is used as electrolyte and the electronic response is measured when a bare Transwell filter and a Transwell filter with intact Caco-2 cell barrier are embedded in the OECT. The OECT transient response and current-driven architectures are measured in the very same conditions, viz. same barrier and consequently. To directly compare the various architectures, we calculated the normalized output response $NR = 100 \times (R - R_0) / R_0$, where in the case of transient response R and R_0 is the transient time without and with cells, respectively, in the case of conventional current-driven R and R_0 is the switching voltage V_{SW} measured without and with cells, respectively, and in the

case of dynamic-mode current-driven OECT R and R_0 is the phase-shift voltage V_{PS} measured without and with cells, respectively. **Fig. 5.9 b** shows NR as a function of time for the various methods. The insertion of the cell barrier results in a $NR > 120\%$ in the case of dynamic-mode current-driven (DCD) OECT operated at $SR = 0.5 \text{ V s}^{-1}$. NR reduces to 40% when the conventional current-driven (CD) is used and lowers to $NR = 25\%$ in the case of the transient response (TR) method. This comparison shows that the DCD provides an enhanced sensitivity with respect to the state-of-art OECT methods and, according to previous studies,^[21] confirms that the CD is more sensitive than TR.

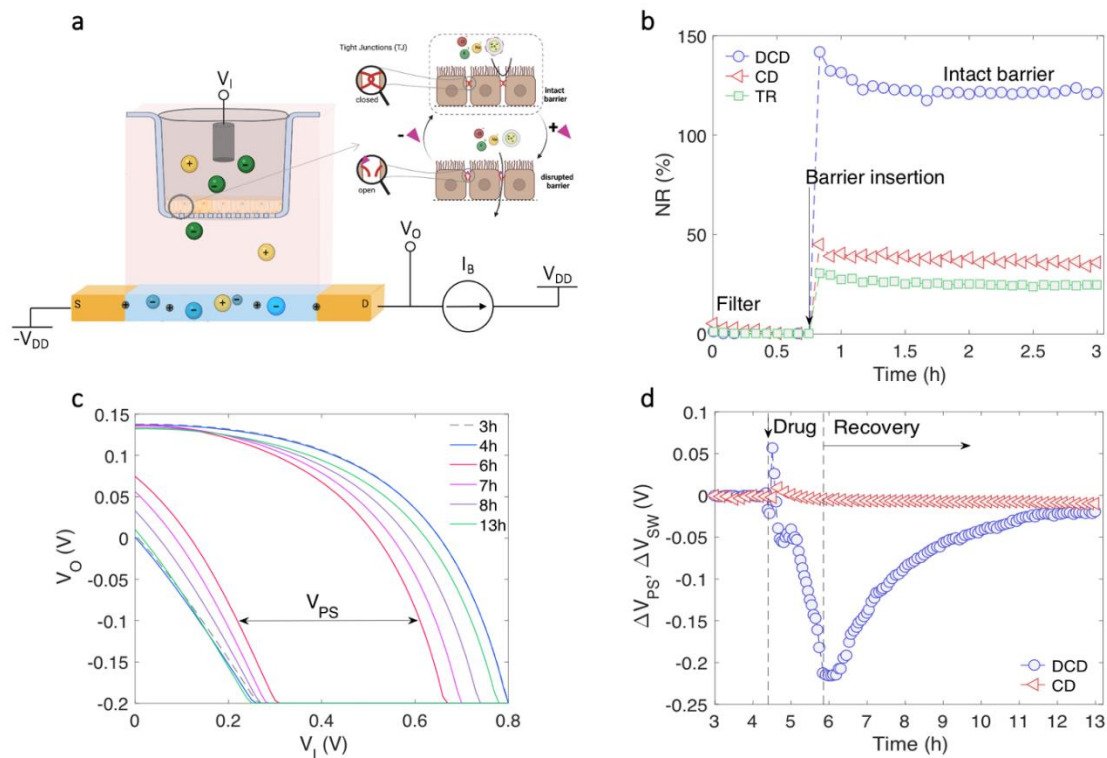


Figure 5.9: High-sensitivity real-time monitoring of cellular barrier functionality. **a)** Schematic representation of a current-driven OECT coupled with a biological barrier tissue, e.g. human Caco-2 cells. Ion transport through the barrier depends on the status of the tight junctions (TJs) proteins. TJs Upon to the addition of a TJ modulator, inserted on a drug carrier, TJs open, the tissue becomes permeable to ions and drug carriers. By removing the TJ modulator in the electrolyte, the TJs are closed and the barrier functionality is restored limiting the ions and drug passage. Created with BioRender.com. **b)** Normalized response $NR = 100 \times (R - R_0) / R_0$ as a function of time. In the case of transient response R and R_0 is the transient time without and with cells, respectively, in the case of conventional current-driven (CD) R and R_0 is the switching voltage V_{SW} measured without and with cells, respectively, and the case of dynamic-mode current-driven (DCD) OECT R and R_0 is the phase-shift voltage V_{PS} measured without and with cells, respectively. The cell barrier is inserted into the electrolyte at time = 50 min and then the intact barrier is monitored for more than 2 hours. **c)** Measured (transfer characteristics ($V_O - V_I$)) as a function of time. The intact barrier is measured two times at time $t = 3$ h and $t = 4$ h. Then the TJ modulator PLL, $C_{PLL} = 122 \mu\text{M}$, is added to the cell medium. The measured barrier status is displayed at $t = 6$ h where a large amount of TJs are open. Then the electrolyte cell media with PLL is exchanged, and the $V_O - V_I$ characteristics at $t = 7, 8, 13$ h show the recovery of the cellular barrier. **d)** Output signal measured with a DCD, $\Delta V_{PS} = V_{PS}(t) - V_{PS}(t_0)$, and CD, $\Delta V_{SW} = V_{SW}(t) - V_{SW}(t_0)$, as a function of time. The initial time is $t_0 = 3$ h. The CD shows a limited response because of the very small concentration of PLL. By contrast, the dynamic current-driven OECT provides a response ΔV_{PS} of up to 216.2 mV and both the disruption and recovery temporal dynamics are recorded in real-time and high sensitivity. The DCD provides valuable information about the final status of the cellular barrier exposed to the TJ modulator, showing that the full recovery is not achieved after 10 h.

As a next step, cellular barrier functionality is monitored in real-time and in the very same biological conditions with the DCD and CD approaches. The relevant transfer characteristics V_O-V_I measured with a DCD OECT as a function of time are displayed in **Fig. 5.9 c**. The DCD OECT with the intact barrier shows perfectly overlapped characteristics after 3 and 4 hours of continuous measurements, proving the excellent stability of the bioelectronic system. Then, the barrier tissue is exposed to a low concentration of poly-L-lysine (PLL) TJ modulator, $c_{PLL} = 122 \mu\text{M}$, and after 6 hours the TJs are opened (barrier disrupted). Ions can transport from the apical to the basal electrolyte compartment and vice-versa passing through the open channels of the cell barrier. The forward and backward characteristic shifts to smaller and larger V_I , respectively, and as a consequence the phase-shift voltage V_{PS} reduces. Then, the electrolyte cell media with PLL is exchanged, the cellular barrier recovers, the V_O-V_I characteristics shift back, and the corresponding V_{PS} increases. After 13 hours the recovery is completed (green line **Fig. 5.9 c**). The comparison with the initial characteristic of the intact barrier (blue line) shows that a small amount of TJs are still opened, viz. full recovery after PLL is not achieved.

As a comparison, real-time monitoring of the barrier functionality with DCD and CD are displayed in **Fig. 5.9 d**. The output voltage V_{PS} and V_{SW} are normalized with respect to their value obtained when the barrier is intact ($t=t_0$), viz. before exposure to PLL, and hence $\Delta V_{PS} = V_{PS}(t) - V_{PS}(t_0)$ and $\Delta V_{SW} = V_{SW}(t) - V_{SW}(t_0)$. The comparison of ΔV_{PS} and ΔV_{SW} as a function of barrier status demonstrate the real-time high sensitivity of the DCD. Indeed, CD shows a very limited response because of the very small concentration of PLL. By contrast, in the very same biochemical conditions the DCD architecture provides a response ΔV_{PS} of up to 216.2 mV and both the disruption and recovery temporal dynamics can be recorded. Moreover, the high-sensitivity of the DCD provides valuable information about the final status of the cellular layer exposed to the drug, showing that the full recovery is not achieved and few, but measurable, TJs result irreversibly open.

5.4 Conclusion

Seeking for bioelectronic alternatives replacing the animal model on the in-vitro platform, we proposed the dynamic-mode current-driven OECT configuration for high-sensitivity real-time monitoring of the cellular barrier functionality. This approach provides a direct measurement of the cellular barrier status without the need of model-based post-processing and the sensitivity can be enhanced by simply selecting the scan rate of the input signal. This enabled the monitoring in real-time and with high sensitivity cellular barrier in a

wide range of barrier status, viz. resistance, providing on-line reconfiguration and optimization of the bioelectronic system parameters.

The rational and operating principle of the proposed approach are investigated by means of numerical simulations, highlighting the key design parameters. No hardware post-processing optimization is required and a maximum scan-rate sensitivity equal to $1391 \text{ mV V}^{-1} \text{ s}$ is demonstrated. The sensitivity can be dynamically reconfigured achieving the optimal conditions in the whole range of relevant biological conditions. We systematically varied the ionic resistance between the gate and the OECT channel assessing a very large experimental range, from $R = 13 \text{ } \Omega \text{ cm}^2$ to $R = 640 \text{ } \Omega \text{ cm}^2$. The DCD OECT efficiently converted the ionic resistance into a phase-shift of the output voltage V_{PS} . The experimental analysis of the DCD OECT provided an average ionic resistance sensitivity equal to 203 mV dec^{-1} with an operating range of $13\text{-}640 \text{ } \Omega \text{ cm}^2$.

The high sensitivity combined with the direct output response and easy of configuration even during the real-time operation, allowed us to monitor the human Caco-2 cells functionality with enhanced performance with respect to current state-of-art approaches. Barrier disruption and recovery are accurately recorded when PLL at a concentration down to $122 \text{ } \mu\text{M}$ is used as TJ modulator, also showing that the full recovery of the TJs is not achieved. The DCD approach is benchmarked under the very same biochemical conditions with the CD, highlighting the superior performance of the proposed method.

Prospectively, the proposed approach is general, and it could be used as-it-is for real-time multiparametric in-vitro cell monitoring including cell layer coverage, cellular vitality, differentiation, ionic channel molecular transport, and cell toxicity experiments, finding also relevant application in detecting virus-host entry fusion and toxin biomembrane bioelectronic sensors.^[6,22] In addition, the technological implementation can be extended to other electrochemical material technologies including for example n-type and ambipolar organic mixed ionic electronic conductors, as well as accumulation and depletion mode OECTs.^[23] Overall, the high sensitivity combined with the reconfigurable operation and simple fabrication on flexible or even conformable substrates can open opportunities for a next-generation in-vivo organic bioelectronics.

5.5 References

- [1] a) W. Underwood, *Frontiers in plant science* **2012**, *3*, 85.; b) P. Wang, M. Calvo-Polanco, G. Reyt, M. Barberon, C. Champeyroux, V. Santoni, C. Maurel, R. B. Franke, K. Ljung, O. Novak, N. Geldner, Y. Boursiac, D. E. Salt, *Scientific reports*, **2019**, *9*, 1, 1-11.
- [2] a) J. Yeste, X. Illa, M. Alvarez, R. Villa, *J. of Biological Engin.*, **2018**, *12*, 1, 1-19.; b) C. Chelakkot, J. Ghim, S. H. Ryu, *Exp. & molec. medicine* **2018**, *50*, 8, 1-9.
- [3] C. Zihni, C. Mills, K. Matter, M. S. Balda, *Nature rev. Molec. cell biology*, 2016, *17*, 9, 564-580.
- [4] S. L. Barron, J. Saez, R. M. Owens, *Adv. Biology*, **2021**, *5*, 6, 2000624.
- [5] M. Blanchette, R. Daneman, *Mechanisms of development*, **2015**, *138*, 8-16.
- [6] S. F. Bint E. Naser, H. Su, H. Y. Liu, Z. A. Manzer, Z. Chao, A. Roy, A.-M. Pappa, A. Salleo, R. M. Owens, S. Daniel, *ACS Applied Bio Materials*, 2021, *4*, 11, 7942-7950.
- [7] L. Yuan, H. C. van der Mei, H. J. Busscher, B. W. Peterson, *Frontiers in microbiology*, **2020**, 2891.
- [8] a) G. Linz, S. Djeljadini, L. Steinbeck, G. Köse, F. Kiessling, M. Wessling, *Biosensors and Bioelectronics*, **2020**, *165*, 112345.; b) D. A. Koutsouras, L. V. Lingstedt, K. Lieberth, J. Reinholz, V. Mailänder, P. W. M. Blom, P. Gkoupidenis, *Adv. Healthcare Mater.*, 2019, *8*, 23, 1901215.
- [9] L. H. Jimison, S. A. Tria, D. Khodagholy, M. Gurfinkel, E. Lanzarini, A. Hama, G. G. Malliaras, R. M. Owens, *Adv. Mater.* **2012**, *24*, 5919.
- [10] a) C. Lubrano, G. M. Matrone, G. Iaconis, F. Santoro, *ACS nano*, **2020**, *14*, 10, 12271-12280.; b) C. Pitsalidis, A. M. Pappa, A. J. Boys, Y. Fu, C. M. Moysidou, D. van Niekerk, R. J. Saez, A. Savva, D. Iandolo, M. Owens, *Chemical Rev.*, 2022, *122*, 4, 4700–4790.
- [11] a) P. Romele, M. Ghittorelli, Z. M. Kovács-Vajna, F. Torricelli, *Nature commun.*, **2019**, *10*, 1, 1-11.; b) F. Torricelli, D. Z. Adrahtas, Z. Bao, M. Berggren, F. Biscarini, A. Bonfiglio, C. A. Bortolotti, D. D. Frisbie, E. Macchia, G. G. Malliaras, I. McCulloch, M. Moser, T-O Nguyen, R. M. Owens, A. Salleo, A. Spanu, L. Torsi, *Nature Rev. Methods Primers*, **2021**, *1*, 1, 1-24.
- [12] a) M. Ramuz, K. Margita, A. Hama, P. Leleux, J. Rivnay, I. Bazin, R. M. Owens, *ChemPhysChem*, **2015**, *16*, 6, 1210-1216.; b) F. Decataldo, M. Barbalinardo, M. Tessarolo, V. Vurro, M. Calienni, D. Gentili, B. Fraboni, *Adv. Materials Techn.* 2019, *4*, 9, 1900207.
- [13] C. Yao, C. Xie, P. Lin, F. Yan, P. Huang, I. M. Hsing, *Adv. Mater.*, 2013, *25*, 45, 6575-6580.
- [14] A. Romeo, G. Tarabella, P. D'Angelo, C. Caffarra, D. Cretella, R. Alfieri, P. G. Petronini, S. Iannotta, *Biosensors and Bioelectronics*, 2015, *68*, 791-797.
- [15] a) L. V. Lingstedt, M. Ghittorelli, M. Brückner, J. Reinholz, N. I. Crăciun, F. Torricelli, V. Mailänder, P. Gkoupidenis, P. W. M. Blom, *Adv. Healthcare Mater.* **2019**, *8*, e1900128.; b) K. Lieberth, M. Brückner, F. Torricelli, V. Mailänder, P. Gkoupidenis, P. W. M. Blom, *Adv. Mater. Technol.*, **2021**, *6*, 2000940.
- [16] K. Lieberth, P. Romele, F. Torricelli, D.A. Koutsouras, M. Brückner, V. Mailänder, P. Gkoupidenis, P.W.M. Blom, *Adv. Healthcare Mater.*, **2021**, *10*, 19, 2100845.
- [17] a) S. Y. Yeung, X. Gu, C. M. Tsang, S. W. Tsao, I. M. Hsing, *Sensors and Actuators A: Physical*, 2019, *287*, 185-193.; b) S. Y. Yeung, X. Gu, C. M. Tsang, S. W. G. Tsao, I. M. Hsing, *Sensors and Actuators B: Chemical*, **2019**, *297*, 126761.
- [18] a) A. Giovannitti, R. B. Rashid, Q. Thiburce, B. D. Paulsen, C. Cendra, K. Thorley, D. Moia, J. T. Mefford, D. Hanifi, D. Weiyuan, M. Moser, A. Salleo, J. Nelson, I. McCulloch, J. Rivnay, *Adv. Mater.*, **2020**, *32*, 16, 1908047. b) M. P. Ferro, L. Leclerc, M. Sleiman, B. Marchiori, J. Pourchez, R. M. Owens, M. Ramuz, *Adv. Biosystems*, **2019**,

- 3, 3, 1800249.; c) F. Decataldo, M. Barbalinardo, D. Gentili, M. Tessarolo, M. Calienni, M. Cavallini, B. Fraboni, *Adv. Biosystems*, **2020**, 4, 1, 1900204.
- [19] D. A. Bernardis, G. G. Malliaras, *Adv. Functional Materials*, **2007**, 17, 17, 3538-3544.
- [20] a) M. C. Valenzano, K. DiGuilio, J. Mercado, M. Teter, J. To, B. Ferraro, B. Mixson, I. Manley, V. Baker, V. A. Moore, J. Wertheimer, J. M. Mullin, *PloS one*, **2015**, 10, 7, e0133926.; b) C. M. Moysidou, C. Pitsalidis, M. Al-Sharabi, A. M. Withers, J. A. Zeitler, R. M. Owens, *Advanced Biology*, **2021**, 5, 2, 2000306;
- [21] a) G. C. Faria, D. T. Duong, A. Salleo, *Organic Electronics*, **2017**, 45, 215-221.; b) M. Ghittorelli, L. Lingstedt, P. Romele, N. I. Crăciun, Z.M. Kovács-Vajna, P.W.M. Blom, F. Torricelli, *Nature Commun.* **2018**, 1441.
- [22] T. Tang, A. Savva, W. C. Traberg, C. Xu, Q. Thiburce, H. Y. Liu, A. M. Pappa, E. Martinelli, A. Withers, M. Cornelius, A. Salleo, R. M. Owens, S. Daniel, *ACS nano*, **2021**, 15, 11, 18142-18152.;
- [23] a) C. Y. Yang, M. A. Stoeckel, T. P. Ruoko, H. Y. Wu, X. Liu, N. B. Kolhe, Z. Wu, Y. Puttisong, C. Musumeci, M. Massetti, H. Sun, K. Xu, D. Tu, W. M. Chen, H. Y. Woo, M. Fahlman, S. A. Jenekhe, M. Berggren, S. Fabiano, *Nature commun.*, **2021**, 12, 1, 1-8.; b) R. B. Rashid, W. Du, S. Griggs, I. P. Maria, I. McCulloch, J. Rivnay, *Sci. adv.*, **2021**, 7, 37, eabh1055.; c) A. F. Paterson, A. Savva, S. Wustoni, L. Tsetseris, B. D. Paulsen, H. Faber, A. H. Emwas, X. Chen, G. Nikiforidis, T. C. Hidalgo, M. Moser, I. P. Maria, J. Rivnay, I. McCulloch, T. D. Anthopoulos, S. Inal, *Nature commun*, **2020**, 11, 1, 1-11. d) Z. S. Parr, R. B. Rashid, B. D. Paulsen, B. Poggi, E. Tan, M. Freeley, M. Palma, I. Abrahams, J. Rivnay, C. B. Nielsen, *Adv. Electronic Mater.*, **2020**, 6, 6, 2000215.; e) S. Chen, A. Surendran, X. Wu, S. Y. Lee, M. Stephen, W. L. Leong, *Adv. Mater. Techn.*, **2020**, 5, 12, 2000523.

6 Conclusion

In short, this thesis focuses on the optimization of using the organic electrochemical transistor (OECT) as an impedance sensor for barrier tissue using the current-driven configuration.

Bioelectronic research and with it the OECT stemmed from the ground only 30 years ago, with promising results. The OECT as an impedance sensor monitoring *in vitro* cultured barrier tissue outstands commonly used biotechnologies in many aspects, as it is a non-invasive, biocompatible, easy to fabricate device architecture. However, the ability to measure only over short time scales and a low ion sensitivity hinder state-of-the-art OECT measurement configurations to *in-situ* monitor small changes in barrier modulation. To date, despite significant research progress on biosensing barrier tissue integrity with the OECT has been achieved, an *in-situ* measurement configuration with high ion-sensitivity is still missing to transform it into a commercialized biosensor. In this thesis, the current-driven OECT in sensing barrier tissue has been comprehensively studied to provide an improved understanding on sensing the resistance of integrated barrier tissue as an insightful parameter for toxicological and drug delivery research.

This thesis combines both, an experimental study on *in-situ* monitoring reversible tight junction (TJ) modulation over long time, as well as a profound investigation and optimization of the current-driven measurement configuration sensing various resistances of barrier tissue. To translate ionic into electronic current the widely used organic mixed ionic-electronic conducting (OMIEC) polymer PEDOT:PSS has been chosen as channel material. As an example for barrier tissue, we cultivated Caco-2 cells, a well-established model for the intestine having a high barrier functionality of $\sim 500 \Omega \text{ cm}^2$.

In **Chapter 1** of this thesis an introduction to organic bioelectronic devices, mixed ion-electron conductors, OECTs and their application in biology with a specification on the OECT as an impedance sensor is provided. In **Chapter 2** the current-driven configuration of the OECT and the promising results of current-driven OECTs in terms of ion sensitivity are presented. In **Chapter 3** the accomplished experimental processing steps for producing OECT devices and cell preparations are explained in detail. Further, the electrical characterisation methods in described, providing information on the transient response, current-driven, optimized dynamic current-driven configuration, cell layer integrity, Transepithelial electrical resistance measurement and electrochemical impedance spectroscopy. After a detailed portrayal on

measuring reversible TJ modulation, the used microscopical characterisation method are explained.

Operating the OECT in current-driven configuration results in a promising ion sensitivity of $1200 \text{ mV V}^{-1} \text{ dec}^{-1}$. The operating voltage can be maintained low, as a set current bias determines the sensing range of the measured output voltage. In **Chapter 4** monitoring reversible TJ modulation *in-situ* with an OECT in current-driven configuration is presented, as the paracellular permeability across an epithelial cell barrier is investigated. Measuring in current-driven configuration under humidified conditions, as it is required for cell culture, makes it possible to monitor barrier tissue with the OECT over 24 h, a timescale which is clinically relevant for drug delivery. The ion sensitivity of the current-driven configuration is high enough not only to sense the presence of barrier tissue, but also small changes in the resistance of the tissue due to opening and closing of TJs. As TJ modulator the polycationic polymer Poly-L-Lysine (PLL) was used, being a well-studied and customized additive in pharmaceuticals. We demonstrated that a small concentration ($82 \mu\text{mol L}^{-1}$) is hardly affecting TJ properties, whereas a medium concentration ($162 \mu\text{mol L}^{-1}$) induces reversible TJ modulation. In contrast, a high concentration ($326 \mu\text{mol L}^{-1}$) causes irreversible alteration of TJ properties. With the OECT in current-driven configuration not only the process of TJ opening, but also of TJ closing can be precisely monitored as a variation of the output voltage. Our work proved that the concentration of TJ modulators is essential and has to be systematically studied in order to find the optimum concentration window and at the same time to avoid toxicity phenomena leading to irreversible phenomena of the barrier integrity.

In **Chapter 5** real-time monitoring of barrier tissue in the dynamic-mode current-driven OECT configuration is shown highlighting the enhanced ion sensitivity. An increase in the selected scan rate of the input signal leads to an enhanced ion sensitivity. The operating principle of the proposed method are investigated by means of numerical simulations, highlighting the key design parameters. We demonstrated a maximum scan-rate sensitivity equal to $1391 \text{ mV V}^{-1} \text{ s}$. Assessing a very large experimental range ($\text{TER} = 13 - 640 \Omega \text{ cm}^2$) the DCD OECT efficiently converted the ionic resistance into a phase-shift of the output voltage V_{PS} . An average ionic resistance sensitivity equal to 203 mV dec^{-1} within the experimental operating range is obtained. TJ opening and recovery are accurately recorded even at the limit of detection of TJ modulator concentration using PLL at a concentration down to $122 \mu\text{M}$. The DCD approach is benchmarked under the very same biochemical conditions with the CD, highlighting the superior performance of the proposed method. Prospectively, the proposed approach is general and could find application for real-time multiparametric *in-vitro* cell

monitoring. In addition, the technological implementation can be extended to other electrochemical material technologies including for example n-type and ambipolar organic mixed ionic electronic conductors, as well as accumulation and depletion mode OECTs. Overall, the high sensitivity combined with the reconfigurable operation and simple fabrication on flexible or even conformable substrates can open opportunities for a next-generation in-vivo organic bioelectronics.

Appendix

Declaration

I hereby declare that I wrote the dissertation submitted without any unauthorized external assistance and used only sources acknowledged in this work. All textual passages which are appropriate verbatim or paraphrased from published and unpublished texts, as well as all information obtained from oral sources, are duly indicated and listed in accordance with bibliographical rules. In carrying out this research, I complied with the rules of standard scientific practice as formulated in the statutes of Johannes Gutenberg-University Mainz to insure standard scientific practice.

A handwritten signature in blue ink that reads "Katharina Lieberth". The signature is written in a cursive style and is positioned above a horizontal dotted line.

(Katharina Lieberth)

List of Publications

Journal Publications:

First-authorships:

- **K. Lieberth**, M. Brückner., F. Torricelli, V. Mailänder, P. Gkoupidenis, P.W.M. Blom, "Monitoring Reversible Tight Junction Modulation with a Current-Driven Organic Electrochemical Transistor", *Advanced Materials Technologies*, 2021, 2000940
- **K. Lieberth**, P. Romele, F. Torricelli, D.A. Koutsouras, M. Brückner, V. Mailänder, P. Gkoupidenis, P.W.M. Blom, "Current-Driven Organic Electrochemical Transistors for Monitoring Cell Layer Integrity with Enhanced Sensitivity", *Advanced Healthcare Materials*, 2021, 10 (19), 2100845
- **K. Lieberth**, A. Pavlou, D. Harig, P. Gkoupidenis, P.W.M. Blom, F. Torricelli, "Monitoring Barrier Tissue Integrity with the Dynamic-Mode Current-Driven Organic Electrochemical Transistor", 2022, (submitted)
- T. Sarkar*, **K. Lieberth***, A. Pavlou, T. Frank, V. Mailaender, I. McCulloch, P. W. M. Blom, F. Torricelli, P. Gkoupidenis, "An organic artificial spiking neuron with electrobiochemical degrees of control for in-situ neuromorphic sensing and biointerfacing", 2022, (submitted)

Co-authorships:

- Krauhausen, D. A. Koutouras, A. Melianas, S.T. Keene, **K. Lieberth**, H. Ledanseur, R. Sheelamanthula, Giovannitti, F. Torricelli, I. McCulloch, P.W.M. Blom, A. Salleo, Y. Van de Burgt, P. Gkoupidenis, "Local sensorimotor control and learning in robotics with organic neuromorphic electronics", *Science Advances*, 2021, 7 (50)
- DA Koutsouras, **K Lieberth**, F Torricelli, P Gkoupidenis, PWM Blom, "Selective Ion Detection with Integrated Organic Electrochemical Transistors", *Advanced Materials Technologies*, 2021, 2100591
- F. Torricelli, P. Romele, P. Gkoupidenis, D.A. Koutsouras, **K. Lieberth**, Z. M. Kosvács-vajna, P.W.M. Blom, "Integrated amplifier with complementary organic electrochemical transistors for high-sensitivity ion detection and real-time monitoring", *Integrated Sensors for Biological and Neural Sensing*, 11663, 1166314
- I. Krauhausen, D. A. Koutouras, A. Melianas, S.T. Keene, **K. Lieberth**, H. Ledanseur, R. Sheelamanthula, Giovannitti, F. Torricelli, I. McCulloch, P.W.M. Blom, A. Salleo, Y. Van

- de Burgt, P. Gkoupidenis, “Local sensorimotor control and learning in robotics with organic neuromorphic electronics”, *Neural Interfaces and Artificial Senses*, 2021
- P. Romele, P. Gkoupidenis, D. A. Koutsouras, **K. Lieberth**, Z. M. Kovács-Vajna, P.W.M. Blom, F. Torricelli, “Multiscale real time and high sensitivity ion detection with complementary organic electrochemical transistors amplifier”, *Nature communications*, 2020, 1(11)
 - D. A. Koutsouras, L. V. Lingstedt, **K. Lieberth**, J. Reinholz, V. Mailänder, P. W.M. Blom, P. Gkoupidenis.,,“Probing the Impedance of a Biological Tissue with PEDOT: PSS-Coated Metal Electrodes: Effect of Electrode Size on Sensing Efficiency“, *Advanced Healthcare Materials*, 2019, 8(23), 1901215
 - M Schleep, C Hettich, J Velázquez Rojas, D Kratzert, T Ludwig, **K Lieberth**, I. Krossing, “The Parent Cyclopentadienyltin Cation, Its Toluene Adduct, and the Quadruple-Decker [Sn₃Cp₄]²⁺”, *Angewandte Chemie International Edition*, 2018, 56(11), 2880

List of Conferences

International Conference Contributions:

Oral Presentations

- **K. Lieberth**, M. Brückner, F. Torricelli, V. Mailänder, P. Gkoupidenis, P.W.M. Blom, “OEETs with integrated cell membrane”, MPFL, September 2019, Lisbon, Portugal
- **K. Lieberth**, M. Brückner, F. Torricelli, V. Mailänder, P. Gkoupidenis, P.W.M. Blom, “Monitoring Reversible Tight Junction Modulation with a current-driven OEET”, MRS Spring/Fall, 2020, virtual
- **K. Lieberth**, M. Brückner, V. Mailänder, F. Torricelli, P. Gkoupidenis, P.W.M. Blom, “Organic electrochemical transistors to measure tight junction modulation”, Nanotechnology, 2021, Thessaloniki, Greece
- **K. Lieberth**, D. Harig, P. Gkoupidenis, P.W.M. Blom, F. Torricelli, “High-sensitivity and real-time monitoring of cell layers with dynamic-mode current-driven OEET”, MRS Fall, 2021, Boston, USA

Poster Presentations

- **K. Lieberth**, L. V. Lingstedt, M. Brückner, J. Reinholz, M. Ghittorelli, F. Torricelli, N.I. Craciun, V. Mailänder, P. Gkoupidenis, P.W.M. Blom, “Organic electrochemical transistors to measure tight junction modulation”, Fp14, 2019, Berlin, Germany
- **K. Lieberth**, L.V. Lingstedt, M. Brückner, M. Ghittorelli, F. Torricelli, V. Mailänder, P. Gkoupidenis, P.W.M. Blom, “The organic electrochemical transistor to measure tight junction modulation”, MPIP, 2019, Mainz, Germany
- **K. Lieberth**, M. Brückner, F. Torricelli, V. Mailänder, P. Gkoupidenis, P.W.M. Blom, “Biosensing barrier tissue with the organic electrochemical transistor”, MPIP, 2020, Mainz, Germany
- **K. Lieberth**, A. Pavlou, D. Harig, P. Gkoupidenis, F. Torricelli, P.W.M. Blom, “Sensing barrier tissue with the dynamic current-driven OEET”, MPIP-Posterday, 2021, Mainz, Germany

Curriculum Vitae

Katharina Lieberth

Date of Birth: 01/09/1993

Place of Birth: Bamberg

Nationality: German

PROFESSIONAL CAREER

- 10/2018-03/2022 Doctoral Candidate in chemistry, Max Planck Institute for Polymer Research and Johannes Gutenberg University (JGU), Mainz
 Thesis: *Cell Integrity in organic electrochemical transistors*
- 10/2015-03/2018 M.Sc. , Chemistry, Julius-Maximilian University, Würzburg, Germany
 Thesis: *Synthesis and Characterisation of an inorganic-organic Hybrid-Polymer with Positive-Resist-behaviour*
- 10/2012-07/2015 Bilingual B.Sc., Chemistry, Albert-Ludwigs University, Freiburg, Germany and Université de Haute-Alsace, Mulhouse, France
 Thesis: *Synthesis and characterisation of Sn(I)Cp⁺ - cation and weakly coordination anions*
- 09/2004-07.2012 Maria-Ward Gymnasium, Bamberg, Germany

Conference Contributions

- 05/2019 Poster Presentation at Fp14, Berlin, Germany
- 09/2019 Oral Talk at MPFL-Symposium, Lisabon, Portugal
- 10/2019 Poster Presentation at Max Planck Institute for Polymer Research
- 10/2020 Poster Presentation at Max Planck Institute for Polymer Research
- 11/2020 Oral Talk at MRS Fall, Boston, USA
- 07/2021 Oral Talk at Nanotexnology 2021, Thessaloniki, Greece
- 12/2021 Oral Talk at MRS Fall 2021, Boston, USA

Working and Practical Experiences:

- 2018-2020 Tutorial job at the Chemistry Department at the Johannes Gutenberg University, Mainz, Germany
- 2018-2019 Supervision of Girls´ Day and Family Day 2018 & 2019 at the Max Planck Institute, Mainz
- 2020-2021 Supervision of Bachelor and Master Students
- 09/2017-03/2021 Research assistant at Fraunhofer Institute for Silicate Research ISC, Würzburg, Germany
- 01/2017-05/2017 Research assistant inorganic molecular chemistry at Durham University, England
- 06/2019-03/2022 Member of the PhD Committee at Max-Planck Institute for Polymer Research, Mainz

Mainz, March 13, 2022

Acknowledgements

